Chapter 4

The MICROMEGAS detector

One of the three X-ray detectors in CAST is Micromegas. The principle of operation of this innovative detector is explained and a thorough description of the prototype used in the CAST experiment is given. Before getting into this subject, a short description of the phenomenology used in gaseous detectors introduces a brief mention of the highlights of the gaseous detectors' development through the years.

4.1 Phenomenology of particle detection in a gas

Before moving on, this could be a good point to mention, rather than discuss, the main topics one will come across when studying the interactions of radiation with matter (in a gaseous detector).

4.1.1 Photons

A beam of photons with an intensity I_0, after passing through a medium of thickness χ will have an intensity of

$$I = I_0 e^{-\mu\chi} \tag{4.1}$$

where $\mu = N\sigma$ is the total absorption coefficient, with N the density of atoms and σ the total photon cross section per atom. Figure 4.1 shows an example of σ, which consists of three main factors,

$$\sigma = \Phi_{\text{photo}} + Z\sigma_C + \tau_{\text{pair}} \tag{4.2}$$

each one corresponding to one of the main interactions of photons: the photoelectric effect, Compton scattering and pair production. In the following some more information is given on the process of the most interest, the photoelectric effect. Each of these interactions show a preference in a part of the energy spectrum of the photons: the lower part of the spectrum, up until several keV is ruled by the photoelectric effect. Next comes the Compton scattering, dominating until hundreds of keV, while the last region (above 1.22 MeV) is left for the pair production.

The photoelectric effect

A photon meets an atomic (bound) electron and is absorbed, allowing for the electron to be ejected from the atom, with an energy

$$E = h\nu - E_B \ , \tag{4.3}$$

for $h\nu$ the energy of the photon and E_B the binding energy of the electron.

In the energy region of the X-rays, the cross-section (per atom) is calculated

$$\Phi_{\text{photo}} = 4\alpha^4 \Phi_0 \left(\frac{m_e c^2}{h\nu}\right)^{\frac{7}{2}} Z^5 \tag{4.4}$$

where α=1/137 , $\Phi_0 = 8\pi r_e^2/3$=$6.651\times10^{-25}\,\text{cm}^2$ (for r_e the radius of the electron) and Z the atomic number. From equation (4.4) emerges the strong dependence on the Z, which, depending on the application, will have a significant role on the decision for materials to be used for the detection.

An interesting point arising is what follows the emission of the electron. When ejected, the electron causes a re-arrangement in the shell, which can take either of two ways:

- the Auger effect (a radiationless transition), which is the emission of an electron of energy close to the binding energy after an internal rearrangement of the electrons on the shells, or

- fluorescence, the process through which an electron from an inner shell takes the place of the ejected electron, emitting a photon carrying the energy difference between the two shells.

4.1.2 Electrons

Of all the interactions the charged particles can possibly be involved in, only the electromagnetic one (Coulomb interactions, bremsstrahlung, Čerenkov, transition radiation), whose cross section is of some orders of magnitude bigger than the rest, is practically used for their detection. In gas detectors, the 'signature' of the particles is mainly due to Coulomb interactions.

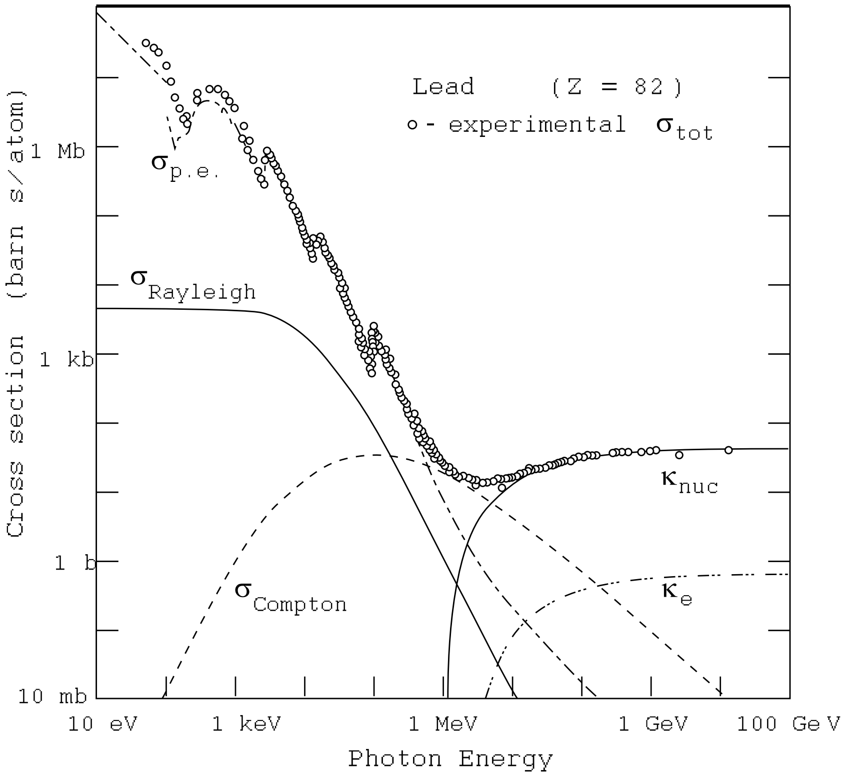

Figure 4.1: The total cross-section for photon absorption in lead. Depending on the energy of the photon, the interaction can follow different mechanisms; at low energies and up to several keV, the photoelectric conversion ($\sigma_{\text{p.e.}}$) is dominant; Compton scattering follows (σ_{Compton}), driving up to some hundreds of keV, while when the barrier of 1.22MeV is reached ($2 \times 0.511\,\text{MeV}$) the electron-positron pair production (κ_{nuc}) is the most probable process. On the figure are noted as well σ_{Rayleigh}, for Rayleigh (coherent) scattering and κ_e for the pair production in the electron field [12].

Energy loss due to Coulomb interactions

The basic calculation for the energy loss is given by the Bethe-Bloch formula

$$-\frac{dE}{dx} = K\rho\frac{Z}{A}\frac{z^2}{\beta^2}\left[\ln\left(\frac{2m_ec^2\beta^2E_{\max}}{I^2(1-\beta^2)}\right)-2\beta^2-\delta-2\frac{C}{Z}\right] \tag{4.5}$$

where:

$K = \dfrac{2\pi N_a e^4}{m_e c^2}$

$N_a =$ 6.022×10^{23} mole^{-1} (the Avogadro number)

ρ, Z, A density, atomic number and mass of the medium

$I =$ $I_0 Z$ where $I_0 \simeq 10\,\text{eV}$ (effective ionization potential of the medium)

z, β charge (in e units) and velocity of incident particle

$E_{\max} = \dfrac{2m_ec^2\beta^2}{1-\beta^2}$ (maximum energy transfer allowed)

and the two correction factors:

δ the density effect correction, important at high energies,

C the shell correction, important at low energies.

The energy loss distribution

The Bethe-Bloch formula provides the mean value of the energy loss. However, due to statistical fluctuations of the number of collisions taking place finally, and on the energy transferred to each of them, the energy lost by any particle will be, most likely, different than that. Fig (4.2) shows a typical distribution of the energy loss in thin media. This Landau distribution has a very characteristic shape, that can be expressed as

$$f(\lambda) = \frac{1}{\sqrt{2\pi}}e^{-\frac{1}{2}(\lambda+e^{-\lambda})} \quad , \tag{4.6}$$

where λ denotes the normalized deviation from the most probable energy loss $(\Delta E)_{\text{mp}}$ when ΔE is the actual loss and ξ the average energy loss:

$$\lambda = \frac{\Delta E - (\Delta E)_{\text{mp}}}{\xi}$$

$$\xi = K\rho \frac{Z}{A}\frac{z^2}{\beta^2}x \tag{4.7}$$

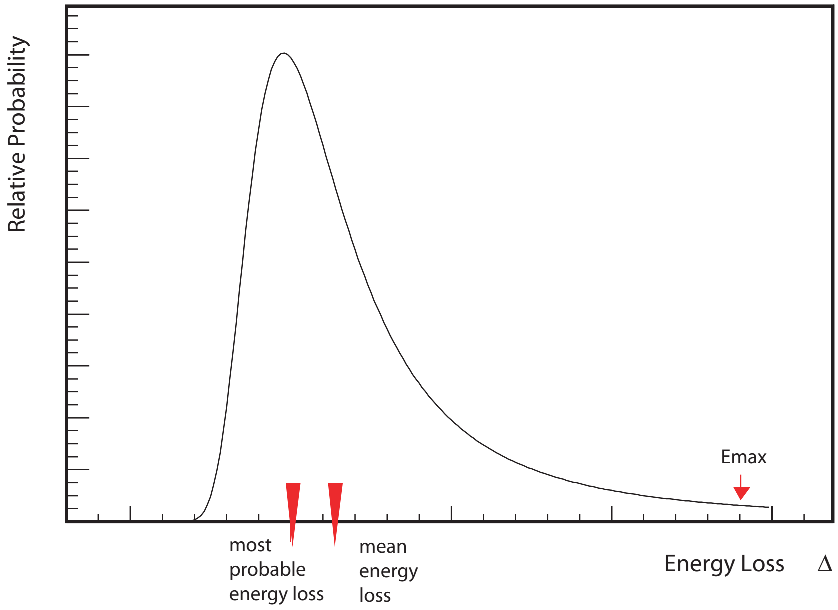

Figure 4.2: The characteristic Landau distribution. The peak indicates the most probable energy loss $(\Delta E)_{\mathrm{mp}}$. The distribution shows a tail in the high energy loss region, due to –rare– energetic δ electrons . This tail causes the mean value ξ of the energy loss to shift to the right of the peak of the distribution. The maximum allowed energy loss per collision $(E_{\max})$ is shown as well.

Range of slow electrons

The electrons ejected after ionization, can have any energy up to $E_{\max}$, the maximum allowed value. Those with an energy above few keV, are known as δ-rays. The number of δ-rays that may have an energy equal or larger than E_0 is

$$N(E \geq E_0) = \int_{E_0}^{E_{\max}} P(E)dE = W\left(\frac{1}{E_0} - \frac{1}{E_{\max}}\right) \tag{4.8}$$

where $P(E)$ represents the probability of an electron having energy E and is essentially the first term of the Bethe-Bloch formula. These electrons are emitted to an angle given by

$$\cos^2\theta = \frac{E}{E_{\max}} \ , \tag{4.9}$$

which means that for the larger energies (several keV) they are emitted perpendicularly. Nevertheless, multiple scattering in the medium causes their direction to be random, and confines their movement. An empirical formula to calculate the practical range is (E in MeV)

$$R_P = 0.71E^{1.72} \quad . \tag{4.10}$$

4.1.3 Excitation and Ionization in Gases

The energy loss discussed in the previous section, can be transferred to electrons through two mechanisms, excitation or ionization.

Excitation

In the case of excitation, an atomic electron acquires an energy which "pushes" the atom to an elevated (excited) state

$$X + p \rightarrow X^* + p$$

and is a resonant reaction, where no electron-ion pairs are produced. The atom eventually returns to its stable state, usually with the emission of a photon. A molecule may have many –characteristic– ways of excitation; for example noble gases can be excited only through photon absorption or emission, while polyatomic molecules have transitions of a rotational and vibrational nature. Excitation can result in ionization; in a gas mixture, composed by a noble gas and a quencher (a polyatomic molecules gas, usually hydrocarbons) the excited noble gas can ionize the quencher, the deexcitation taking place through collisions (Penning effect).

Ionization

Contrary to excitation, an ionization takes place, when an electron-ion pair is created. For this to happen, the energy of the passing particle should be above a threshold equal to the ionization potential of the medium. When the ionization is caused by the incident particle itself, it is called *primary* ionization. If the electron of the pair gains an energy above the threshold it ionizes further, and produces *secondary* ionization. This phenomenon may continue until the threshold for ionizing reactions is reached.

Although there is no simple way of calculating the number of primary ionization pairs produced, it is roughly linearly increasing with the average atomic number of the gas (with the exception of Xe). However, since they follow Poissonian distribution, one can calculate that the probability of having k in one event as

$$P_k^n = \frac{n^k}{k!} e^{-n} \tag{4.11}$$

where n is the average number of primary interactions. The total number of pairs produced (the sum of primary and secondary ionizations) is given by

$$n_{\mathrm{T}} = \frac{\Delta E}{W_i} \quad . \tag{4.12}$$

Table 4.1: Properties of gases at normal conditions: density ρ, minimal energy for excitation E_{ex}, minimal energy for ionization E_{ion}, mean effective ionization potential per atomic electron $I_0 = I/Z$, energy loss W_i per ion pair produced, number of primary ion n_{P} and total number of ion pairs n_{T} per centimeter of path for minimum ionizing particles.[72]

Gas	Z	A	ρ [cm^2/s]	E_{ex} [eV]	E_{ion} [eV]	I_0 [eV]	W_i [eV]	n_{T} [cm^{-1}]	n_{P} [cm^{-1}]
H_2	2	2	8.38×10^{-5}	10.8	15.9	15.4	37	5.2	9.2
He	2	4	1.66×10^{-4}	19.8	24.5	24.6	41	5.9	7.8
Ar	18	39.9	1.66×10^{-3}	11.6	15.7	15.8	26	29.4	94
Xe	54	131.3	5.49×10^{-3}	8.4	12.1	21.1	22	44	307

ΔE is the energy lost and W_i the effective energy for the creation of one electron-ion pair. Values for W_i and other gas properties are given in Table 4.1. For gas mixtures the former formula takes the form

$$n_{\mathrm{T}} = \sum_i \frac{\Delta E}{W_i} \times q \tag{4.13}$$

where i indicates each component, and q the percentage of the component in the mixture.

4.1.4 Transport of ions and electrons in gases

The number of pairs created has just been calculated, and yet that is not necessarily the number of pairs that will be detected; recombination or electron attachment might take place. In the absence of an external electric field (or when it exists but is a low one), the electron-ion pairs will be recombined, drawn to each other by their electrical attraction, and will emit a photon, a process depending on the electron and ion concentrations. In the presence of electronegative gases, the electrons might be captured by atoms of the gas before they are collected, releasing energy known as electron affinity. The probability of attachment h, is very high for oxygen and practically zero for noble gases.

Diffusion

When no electric field is present, the electrons and ions produced by passing radiation lose their energy rather soon, because of the multiple collisions with the gas molecules. They will rest when they assume the average thermal energy

$$\epsilon_{\mathcal{T}} = \frac{3}{2} kT, \tag{4.14}$$

where k is Boltzmann's constant and T the temperature, while their speed will be (if their mass is m)

$$u = \sqrt{\frac{8kT}{\pi m}} \ . \tag{4.15}$$

Naturally, the electrons will be much faster than the ions, due to their much smaller mass.

After diffusing for time t, the linear distribution of the charges is given by

$$\frac{dN}{dx} = \frac{N_0}{\sqrt{4\pi Dt}} e^{-\frac{\chi^2}{4Dt}} \tag{4.16}$$

where N_0 is the total number of charges, χ the distance from the origin and D the diffusion coefficient. The standard deviation then, is expressed using the diffusion coefficient by

$$\sigma(\chi) = \sqrt{2Dt} \tag{4.17}$$

or $\sigma(\chi) = \sqrt{6Dt}$ for three dimensions. With the help of the kinetic theory, and assuming a classical ideal gas, the expression

$$D = \frac{2}{3\sqrt{\pi}} \frac{1}{P\sigma_0} \sqrt{\frac{(kT)^3}{m}} \tag{4.18}$$

(defining σ_0 as the total cross section for a collision with a gas molecule, P and T the pressure and temperature, respectively, of the gas) gives the diffusion coefficient and shows its dependence on the various gas parameters. Typical values of the diffusion parameters for ions in their own gas under normal conditions, are given in Table 4.2.

Mobility ("drift") of ions

Proceeding with the application of an electric field across the gas volume, the movement of the ions is no longer random; they follow, on average, the direction of the field. Although the presence of the field accelerates them, the continuous collisions with the gas molecules limit their movement to an average velocity, the *drift velocity* u which depends linearly

Table 4.2: Values of the mean free path, the velocity, the diffusion coefficient and the mobility of ions in their own gas (under normal conditions)[72].

Gas	λ [cm]	u [cm/s]	D [cm$^2/s$]	μ [cm^2 s^{-1} V^{-1}]
H_2	1.8×10^{-5}	2.0×10^5	0.34	13.0
He	2.8×10^{-5}	1.4×10^5	0.26	10.2
Ar	1.0×10^{-5}	4.4×10^4	0.04	1.7
O_2	1.0×10^{-5}	5×10^4	0.06	2.2

on the ratio E/P (where P is the gas pressure). A useful parameter, the mobility μ, can be defined as

$$\mu = \frac{u}{E} \tag{4.19}$$

and is shown to be related to the diffusion coefficient by

$$\frac{D}{\mu} = \frac{kT}{e} \quad . \tag{4.20}$$

Two observations can be made:

- The mobility of the ions is practically constant, since their average energy basically remains unchanged even for high electric fields, and
- inserting equations (4.19), (4.20) to the standard deviation (equation (4.17)), it is shown that the latter is independent of the nature of the ions and the gas:

  $$\sigma(x) = \sqrt{\frac{2kTx}{eE}}$$

  for x the diffusion length.

Drift of electrons

Unlike ions, the mobility of the electrons is not constant. The electrons take advantage of their small mass and increase their velocity to high values:

$$u = \frac{e}{2m_e} E\tau \tag{4.21}$$

where τ is the mean time between two collisions of an electron (e, m_e) in an electric field E.

Complex quantum-mechanical processes occurring when the electron approaches the molecule, cause τ and essentially the collision cross-section to vary strongly with E, presenting minima and maxima (Ramsauer effect). This has a direct effect on the energy distribution of the electrons, which is now more complicated

$$F(\epsilon) = C\sqrt{\epsilon}\ \exp\left(-\int \frac{3\Lambda(\epsilon)\epsilon d\epsilon}{[eE\lambda(\epsilon)]^2 + 3\epsilon kT\Lambda(\epsilon)}\right) \tag{4.22}$$

for ϵ the electron energy, $\Lambda(\epsilon)$ the fraction of energy lost per collision, $\lambda(\epsilon)$ the mean free path between collisions. For given elastic and inelastic cross sections, the drift velocity will be

$$u(E) = -\frac{2}{3}\frac{eE}{m}\int \epsilon\lambda(\epsilon)\frac{\partial[F(\epsilon)v^{-1}]}{\partial\epsilon}d\epsilon \tag{4.23}$$

with $v = \sqrt{2\epsilon/m}$ and m , ϵ the mass and energy of the electrons respectively.

Diffusion of electrons

During the drift, electrons continue to diffuse obeying the gaussian distribution given for ions. Only the change in the energy distribution, imposed by the electric field, causes a change in the diffusion coefficient :

$$D(E) = \int \frac{1}{3} v \lambda(\epsilon) F(\epsilon) d\epsilon \tag{4.24}$$

with $v = \sqrt{2\epsilon/m}$ and ϵ the energy of the electrons, as shown before.

4.1.5 Multiplication

A single electron drifting towards an anode wire in a strong magnetic field, carries some energy ϵ given by equation (4.22). As it was discussed before, for moderate electric fields the energy carried by the electron will be rather constant on average, due to the random collisions with the gas molecules. However, for higher fields –in the time between collisions with the gas molecules– its energy may increase over the first ionization potential of the gas, and an electron-ion pair will be produced, while the first electron continues its travel possibly producing more pairs. In the same way, these secondary electrons can produce further ionization forming finally an *avalanche*. As already noted, the mobility of the electron is much greater than that of the ions, therefore the electrons are the front of this cloud of charges, while the newly produced ions are still close, parting towards the first produced ions at their pace; the result of this movement is a drop-like distribution as shown in the schematic of figure 4.3.

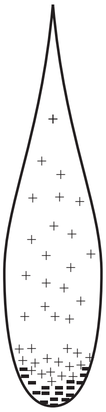

Figure 4.3: The drop-like shape of an avalanche; the more mobile electrons take the head of the drop, leaving behind the slower ions, which are drifting upwards.

The distance that this electron will travel until ionization defines the *mean free path* for ionization. Probably the most interesting quantity is the *first Townsend coefficient* α, the inverse of the mean free path of ionization. α represents the number of pairs produced per unit length of travel. If at some point there are n electrons, after they drift for a path dx

$$dn = n\alpha dx$$

new electrons will have been produced, hence the total number of electrons created in a path x is

$$n = n_0 e^{\alpha x} \quad .$$

The multiplication factor or *gas gain* M is then given by

$$M = \frac{n}{n_0} = e^{\alpha x} \tag{4.25}$$

In the general case of a non-uniform electric field, $\alpha = \alpha(x)$ and M can be expressed as

$$M = \exp(\int_{x_1}^{x_2} \alpha(x)\, dx) \quad .$$

This factor cannot be increased at will, eventually a spark breakdown will occur. The Raether limit, the limit for multiplication before breakdown is

$$\alpha x \sim 20 \;\text{ or }\; M \sim 10^8 \quad .$$

In practice the gain achieved is usually two orders of magnitude less than the Raether limit.

The basic operation of the gas detectors, is the avalanche multiplication.

4.2 Gaseous Detectors; A brief walk through history

Since the discovery of the electromagnetic radiation the question of how to detect it was risen. Because of the greater mobility of electrons and ions, a gas is the obvious medium to use. Several inventions were made, separating the history of the gaseous detectors in periods. Bypassing the very first period with the three original devices; the ionization chamber, the proportional counter and the Geiger-Müller counter, this journey through time will start from a very important moment – worthy of the Nobel Prize (1992) – the invention of the MultiWire Proportional Chamber by G. Charpak in 1968 [73].

The main characteristics of the MWPC (figure 4.4) are the good space resolution (few hundred μm), an excellent energy resolution and a modest rate capability (10^4 counts mm^{-2} s^{-1}). The chamber is widely used apart from the particle physics in other fields like X-rays for medical imaging, neutron and crystal diffraction studies, single photon detection and others.

The introduction of the MWPC triggered many ideas, like using the drift time of the electrons to acquire spatial information: the drift chamber [75]. With the help of a trigger detector, to signify the "time zero" of the event, and measuring the drift time of the electrons, the length of its path and therefore its origin is easily deduced (figure 4.5).

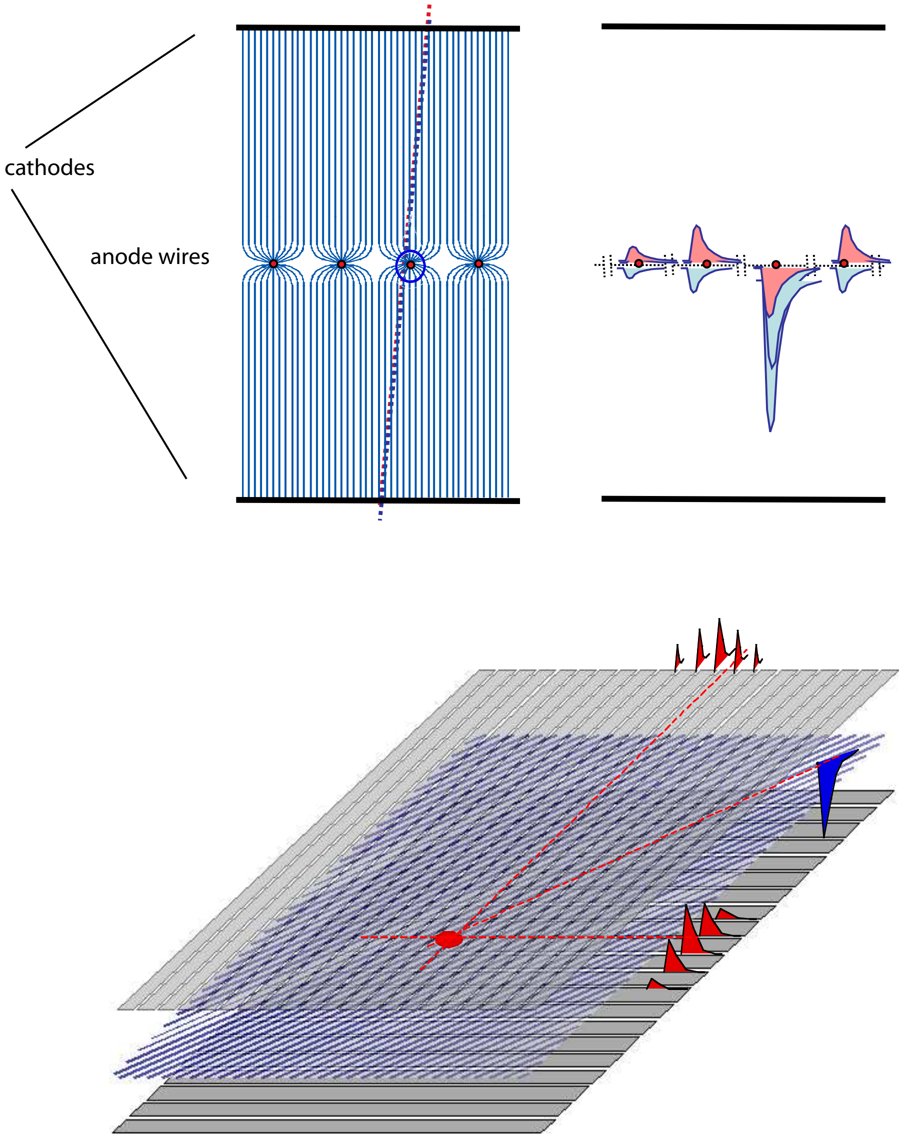

Figure 4.4: Top left: The configuration of the MWPC chamber; a plane of wires –equally spaced– placed in the middle between two cathode planes. Typical distances between the anode wires are 1 to 4 mm, while the two cathode planes are from 5 to 15 mm apart. The figure shows the electric field lines: the electrons that are produced in the constant field region will drift towards the closest anode wire, where under the force of the higher field they will be accelerated and produce an avalanche. Top right: The signal induced in the closest wire and the neighbouring ones. It will be negative in the former one, while in the neighbouring ones positive. Low: With the implementation of a second plane of wires, placed perpendicular to the first one, the spatial information is increased [74].

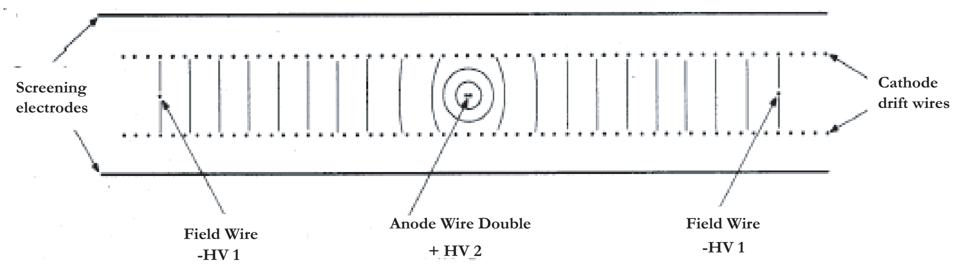

Figure 4.5: In the Drift Chamber the space-information is acquired by measuring the drift-time of the electrons towards the anode. For such a measurement the drift velocity –and therefore the electric filed– must be kept constant. In the chamber shown in the figure, that is achieved with the help of additional wires between the anodes. The cathode wires' potential varies uniformly from 0 (cathode facing the anode wire) downwards to a high negative voltage (cathodes facing the field wires), keeping the electric field very stable, as the equipotential lines demonstrate. Usually the drift regions are approximately $5 - 10\,\mathrm{cm}$, therefore for a typical drift velocity of $5\,\mathrm{cm}/\mu\,\mathrm{s}$ the measured drift time should be 1 or $2\,\mu\,\mathrm{s}$.

A three dimensional information of the particle was achieved with the construction of the Time Projection Chamber (TPC) [76]: a more sophisticated device that combines the features both of the drift chamber and the MWPC. A typical TPC is shown in figure 4.6. The information on the two dimensions is given by the anodes and cathodes of the endcaps, while the third one is deduced from the drift time.

Successful as they may have been, these chambers met with fundamental limitations when questions on better space resolution and higher rate capabilities were raised: wires cannot be placed closer without meeting functional problems, and as far as rates are concerned the positive ions were not evacuated fast enough.

To cover these limitations, Oed [77] invented the Micro-Strip Gas Chamber (MSGC), signifying a new time in the gaseous detectors' history. Taking advantage of the improvement of microelectronics and the development of the process of photolithography, very thin strips are imprinted on an isolating board (figure 4.7), in a succession of narrow anodes and wider cathodes, closer than the wires in a MWPC (typical distances around $50-100\,\mu\mathrm{m}$). Because of the form of the electric field, the ions produced by the avalanche are rapidly evacuated, increasing the counting capacity of the chamber a 100 times above that of MWPC, reaching $10^6\,\mathrm{counts\,mm^{-2}\,s^{-1}}$. Variations of this design were, for example, the Micro-Gap Chamber (MGC) [79] and the WELL detector [80].

MSGCs were welcomed and developed to be included in high-luminosity experiments. However, they were susceptible to aging and discharge damages. The MSGC era was followed by a series of other inventions, leading to the design of the "Micro-Pattern" detectors, which take advantage of new technology in micro-electronics and photolithography, and have high granularity. The "Compteur á Trous" (CAT) [81, 82](evolved later into the micro-CAT [83]) was one of the first examples in 1996; a hole (0.1 to 2 mm in diameter) in a (less than) 2 mm thick metallic plate above the anode, composes a device

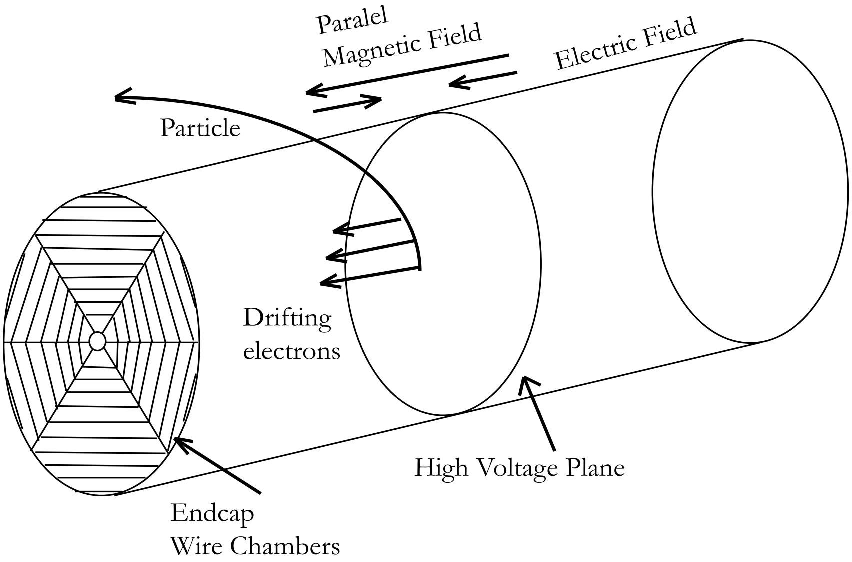

Figure 4.6: A more sophisticated detector, the Time Projection Chamber combines the detection principles of the MWPC and the drift chamber. It is a cylinder with a thin electrode in the middle, creating a uniform electric field along the axis. The cylinder is closed with 'endcaps', which are planes separated in sectors of proportional anodes in between cathode pads. The MWPC logic gives the two-dimensional information, while the third is given by measuring the drift time of the electrons. To minimize diffusion, a magnetic field parallel to the electric one forces the electrons to spiral paths about the field direction. The spatial resolution achieved goes down to 150 μm in the x-y plane and approximately 1 mm on the z axis.

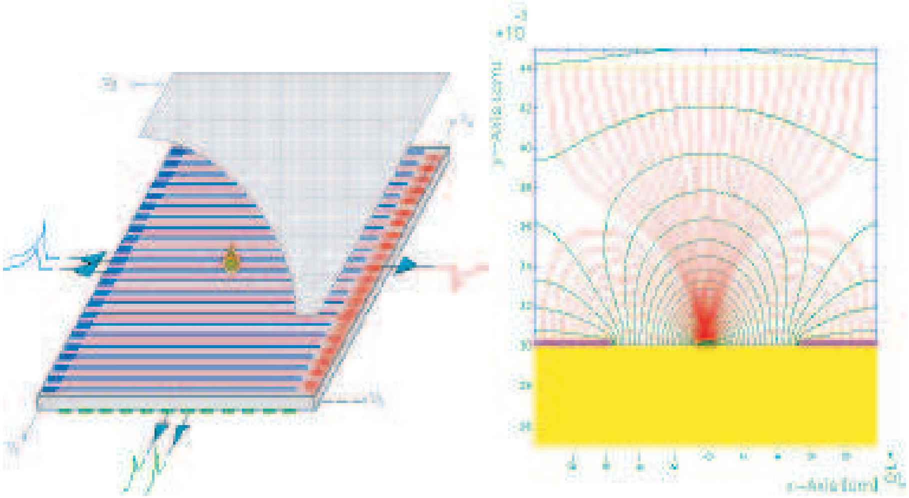

Figure 4.7: The principle of the MicroStrip Gas chamber (a two-dimensional readout on the left); thin anode strips are engraved in between wider cathode strips, all on the same plane, substituting the wires. Applying the proper voltage differences between the two types of strips, all the avalanche is created in front of the anode (right), where the electrons are gathered, while the ions are collected, rather rapidly, in the neighbouring cathodes. The chamber exhibits a good energy resolution, an unprecedented position resolution of the order of 50 μm, while typical counting capacities reach 10^6 counts mm^{-2}s^{-1} [78].

which acts as a lens, focusing the drifting electrons, and leading to the formation of the avalanche. The gain reached, is of about 10^4.

Around the same time, MICROMEGAS was introduced[84]. The principle of the detector will be explained later. To the same generation belong the microdot detector and the GEM. The microdot (μDOT) detector consists of a periodic structure of coaxial cathode and anode rings –with very small diameters, 200 and 20 μm respectively– laid on a dielectric substrate. Gains achieved with this type of detector reached gains of the order of 10^5. Variations of it are a 3d version of the detector, or the MIcro-Pin Array (MIPA)[85].

Using the kapton-etching technology, the Gas Electron Multiplier (GEM)[86, 87], (figure 4.8) introduces a new concept. A thin ($\sim 50\,\mu$m) kapton foil, metallized on both sides, carries holes of 100 μm in diameter every $\sim 150\,\mu$m. A gain of 10^4 is achieved, while using multiple layers of GEMs the counting capacity reaches 10^6).

4.3 MICROMEGAS

MICROMEGAS (for MICRO MEsh GAseous Structure) [84] is a very asymmetric double structure detector. What makes the difference of this detector with the previous is that the two well distinguished regions are no longer separated by a plane of wires, but by a micromesh. Its operation principle can easily be described through its elements; figure

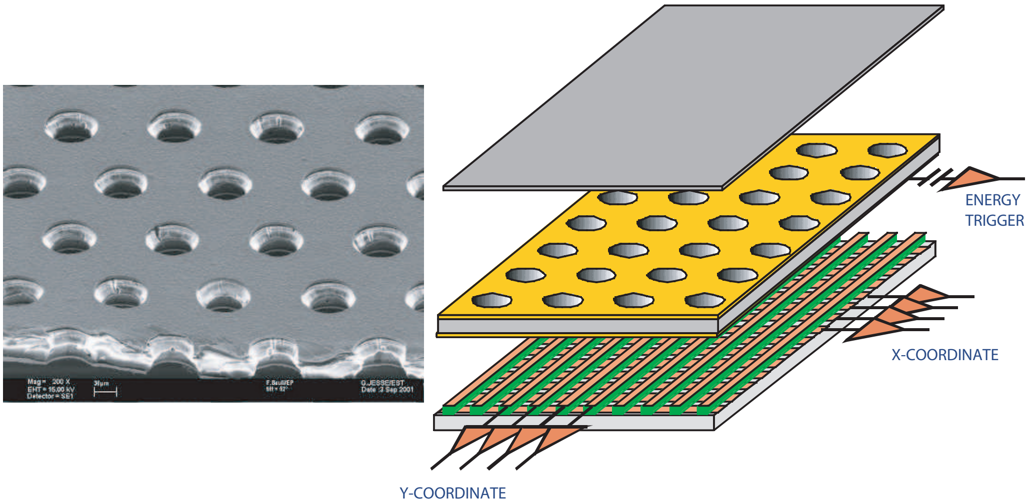

Figure 4.8: Several holes (with a diameter of the order of 50 μm) are chemically etched through a metal-insulator-metal thin-foil composite. In combination with an MSGC (in fact, similar performances can be obtained with multiple layers of GEM), the amplification takes place in two stages, and the gains obtained at discharge are increased [87].

4.9 shows a schematic view.

The very first part a particle will have to cross is the drift electrode. As soon as the drift electrode is passed, the particle is already inside the *conversion* region, which stretches up to some mm until the grid. It holds a rather weak electric field –of the order of 1 kV/cm– and is the place where the ion-electron pair production takes place.

The role of the grid (or else micromesh) is multiple, and does more than marking the end of the conversion gap and the beginning of the *amplification* one [88]. It is made out of copper (5 μm) with a process which relies on the photolithograhy technique that allows to print on it 25 μm openings and a pitch of 50 μm (see figure 4.11). The voltage applied to it (up to 500 V) is such that the ratio of the electric field in the amplification gap over the field of the conversion gap is very big. The bigger the ratio the higher the electron transmission to the amplification gap reached (in practice a ratio of 20 means full transmission). Once in the amplification gap, the process of avalanche is easily started; the gap is so small (of the order of 100 μm) that the electric field achieved is very high (up to 50 kV/cm). At the same time as providing a smooth way for the electrons into the amplification gap, the micromesh prevents the ions produced by the avalanche to enter the conversion gap.

While the ions are collected by the micromesh with a high efficiency and speed, the electrons continue in the amplification gap and end their travel on the anode electrode. The anode electrode consists of copper strips with a typical width of 150 μm and a pitch of 200 μm, grounded through low-noise charge preamplifiers of high gain to an isolating layer (usually kapton).

The advantages of the technique introduced with Micromegas are listed below:

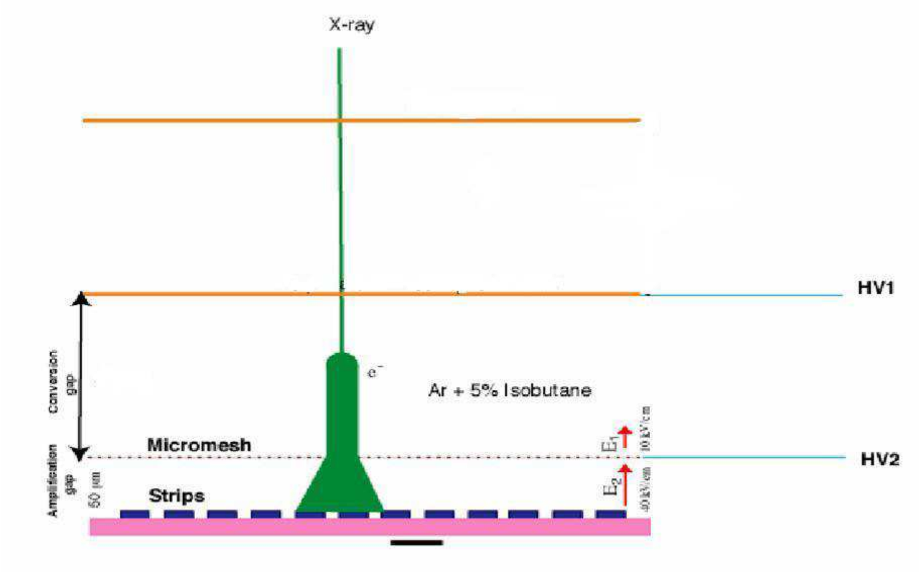

Figure 4.9: A schematic view of Micromegas: the micromesh separates the detector volume to the conversion gap (some mm) and the amplification gap (of the order of 100 μm) which ends to the strip plane.

- The fast response: because of the very small path the ions need to travel (amplification gap length $\sim 100\,\mu$m) and of the very strong field, the ions are very rapidly collected, suppressing any space-charge effects.

- Any mechanical imperfection on the stretching of the micromesh above the strips is compensated, leading to essentially steady gain; an approximation of the change in the amplification factor M with the amplification gap d is given by [91]

  $$\frac{\delta M}{M} = \alpha d \left(1 - \frac{Bd}{V}\right) \frac{\delta d}{d}$$

  for pressure P, applied voltage V and B a constant depending on the gas used. Under constant pressure, when d decreases, the multiplication factor increases up to a maximum (for $d = V/B$) and then decreases for higher values of d. The combination of the amplification gap and the applied voltage in the Micromegas detectors is such, that the multiplication factor is maximized, so fluctuations due to defects of flatness between the mesh and the anode plane are canceled.

- Because of the constant field along the amplification region, the signal detected in the anode is equally due to the ions and the electrons, contrary to the wire chambers.

- An excellent spatial resolution.

- Counting capability of the order of 10^6 counts mm^2 s^{-1} due to the fast evacuation of the ions and the high granularity of the mesh.

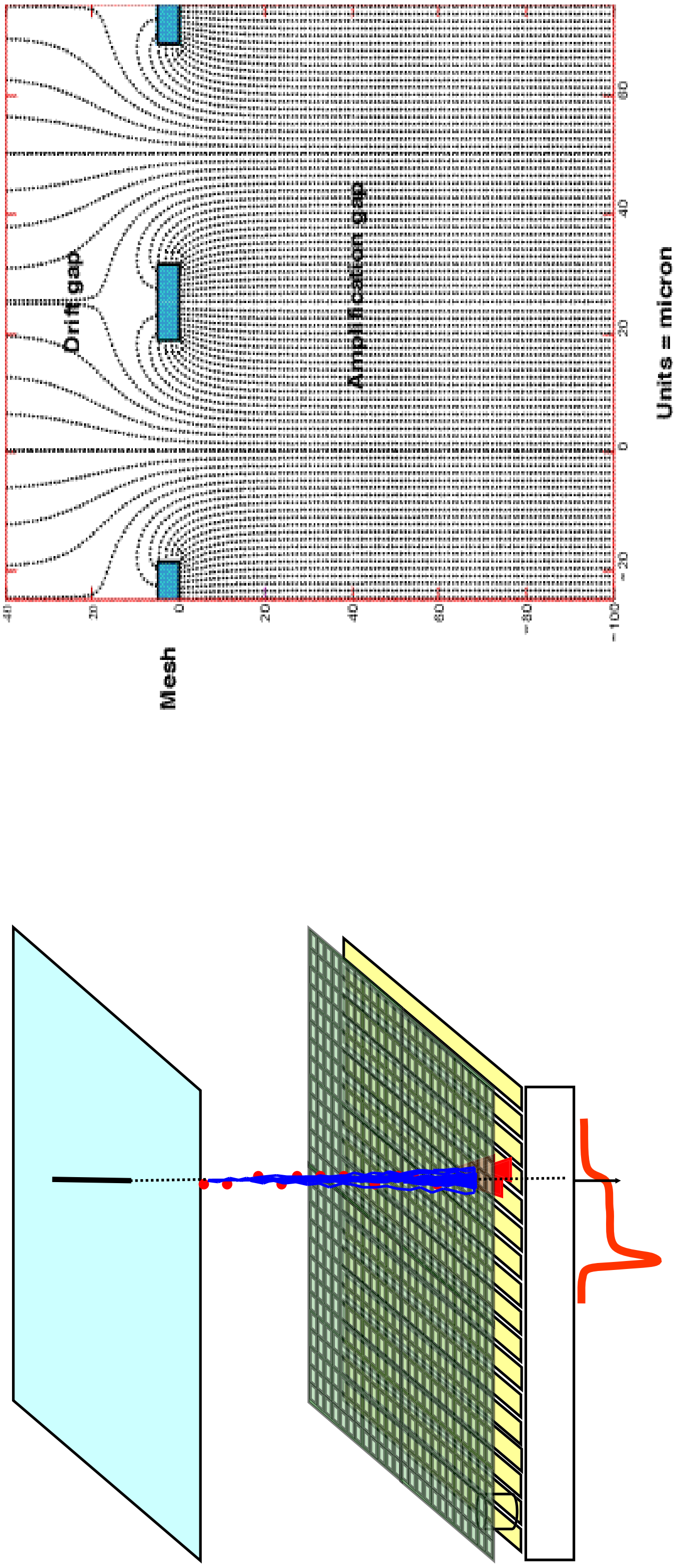

Figure 4.10: Left: A schematic representation of the passage of one particle through the detector's volume. Right: The electric field lines starting just above the mesh and resulting on the strips.

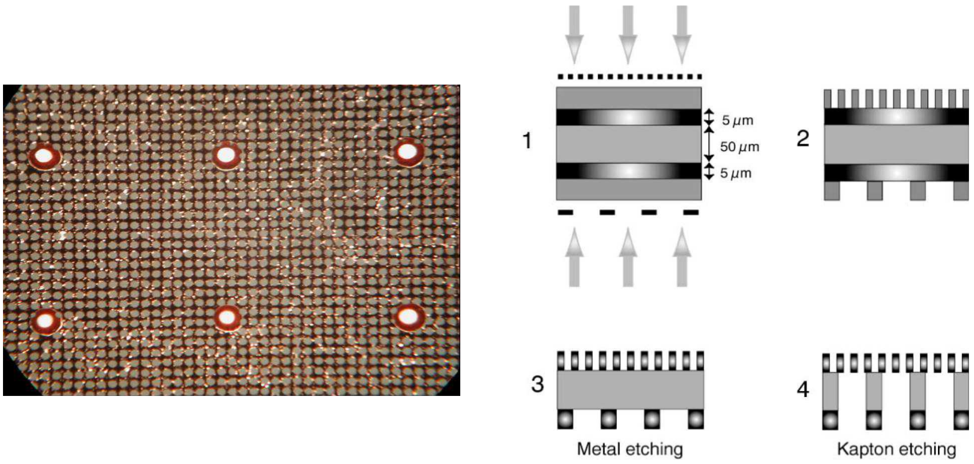

Figure 4.11: A description of the micromesh. Left:A photography taken with a microscope. Right: The new etching process of the mesh: a 50 μm double-sided kapton foil is stretched; solid 15 μm thick photoresist is applied on the two sides of the copper clad; two lithograhic masks (with the patterns of the whole and the pillars) are used for both faces of the kapton; the etching of the copper and kapton provides the final mesh and pillars.

Table 4.3: The performance of Micromegas in various applications.

Spatial resolution	12 μm (rms) [89]
Time resolution	0.2 ns (rms) [90]
Energy resolution (at 5.9 keV)	11% (FWHM) [88]
Rise time of the fast signal	< 1 ns [91]
Signal-to-noise for M.I.Ps	> 100 [92]

Micromegas has been used in a variety of domains, including high energy physics (COMPASS, n_TOF, NA48, TESLA), non accelerator physics (CAST, HELLAZ) and in medical applications (X-ray imaging), reaching performances like the ones in Table 4.3

4.3.1 Description of the CAST Prototype

The CAST experiment requires a low-threshold and low-background detector, optimized to be sensitive to low energy X-ray photons ($1-10$ keV). The main sources of background are cosmic rays and natural radioactivity, thus the choice of the materials used for the construction of this Micromegas detector was made in order to reduce this factor.

The innovation of the CAST prototype is the introduction of the x-y structure: the charge is collected on 192 X strips and 192 Y strips of $\sim 350\,\mu$m pitch, all on the same plane. The kapton substrate is doubly clad so the connections for the X strips is on one side and the connections for the Y strips are on the other side, passing through vias on

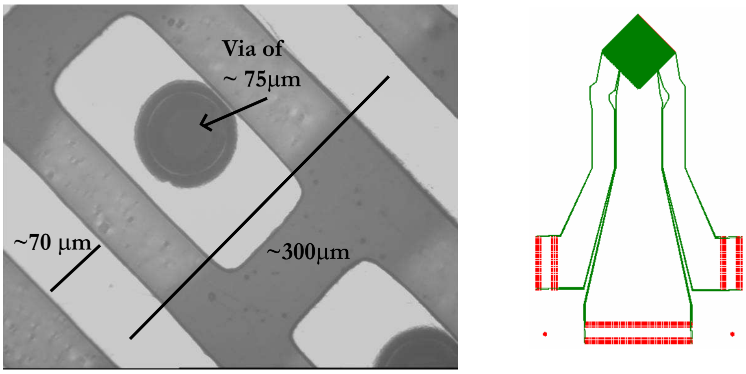

Figure 4.12: Left: The two dimensional reading of the strips, with the mention of some dimensions. Right: Scheme of the X-Y strip plane with the readout transfer lines that end to the four connector pads.

the Y pads as figure 4.12 shows. With the given number and width of the strips, the active area is $\sim 45\,\mathrm{cm}^2$. In figure 4.12 is also shown a schematic of the kapton with the X and Y strips and the readout lines.

The amplification region is only $50\,\mu$m thick reaching from the strips to the micromesh. Above the mesh, the conversion gap is $\sim 25\,$mm thick and ends with a thin ($4\,\mu$m) aluminized polypropylene window, glued on stainless steel strong-back, transparent enough to allow particles to come through and tight enough to keep the gas tightness of the detector to the desired level. This window also serves as the cathode for the drift field. Both the drift and anode electrons are attached to the Plexiglas cylinders, held together via plastic bolts, which compose the detector frame. A blown-up view of the detector in 4.13, and a picture of the detector in the laboratory is given in figure 4.14.

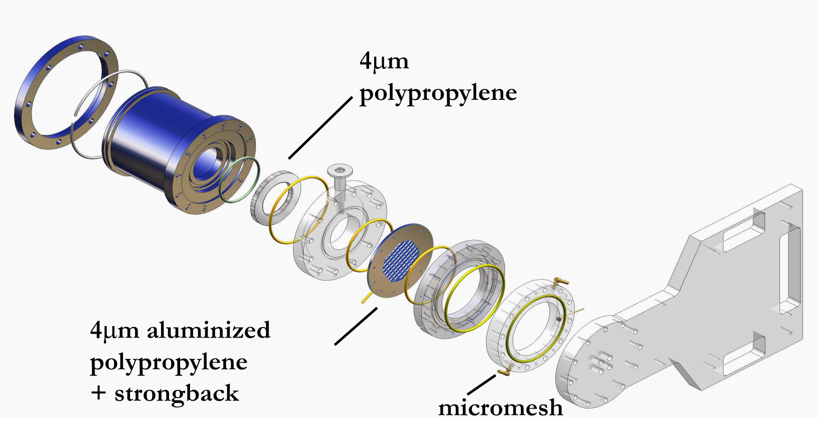

Figure 4.13: A blown-up view of the detector, where its components are clearly separated.

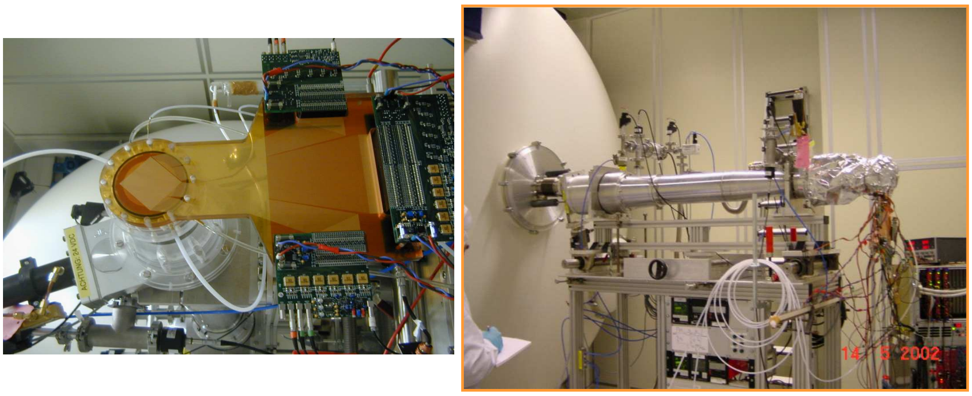

Figure 4.14: Right: The detector on the laboratory bench, equipped with the four electronic cards and the gas pipes. The strip planes and the transfer lines can be distinguished. Left: The Micromegas setup in the clean room of the PANTER X-ray facility.

4.3.2 The Set Up

As described before, the Micromegas is sitting on the west side of the magnet, looking for "sunrise" axions, holding a bore next to the X-ray focusing device. The issue of accommodating everything in a platform, forbade that the detector was directly attached to the magnet vessel. Hence the detector is fastened to the bore with the help of an aluminum tube (approximately 1 m long) and a flange. The magnet volume and the tube are separated by a gate valve (figure 4.15).

In order to couple the (gaseous) detector and the magnet vacuum environment with a maximum transparency to X-ray photons and a minimum vacuum leak the solution of two windows with a differential pumping in between was adopted and developed to fit the setting. The two windows are made of 4 μm polypropylene and their position can be seen in figure 4.16, where the concept is explained.

The two windows define 3 zones: Zone A is the gaseous detector at a pressure of 1 bar, Zone B is the vacuum gap at a pressure of 5×10^{-4} mbar obtained by the pumping group, and Zone C is the vacuum tube at a pressure of 5×10^{-7} mbar in the magnet. The leak of the first window is proportional to the differential pressure between zone A and B, i.e. 1 bar. This differential pressure imposes a strongback on the first window. The leak for this window, tested under zone A full of Helium, is 4×10^{-5} mbar ls^{-1}. As the differential pressure between zone B and C is 5×10^{-4} bar, a strongback is not needed. The net leak for this second window when zone A is full of Helium, has been measured to be 3×10^{-9} mbar ls^{-1}. The leaking gas through the first window is continuously removed by the pump. The pump used for this application is made of a small dry turbo pump

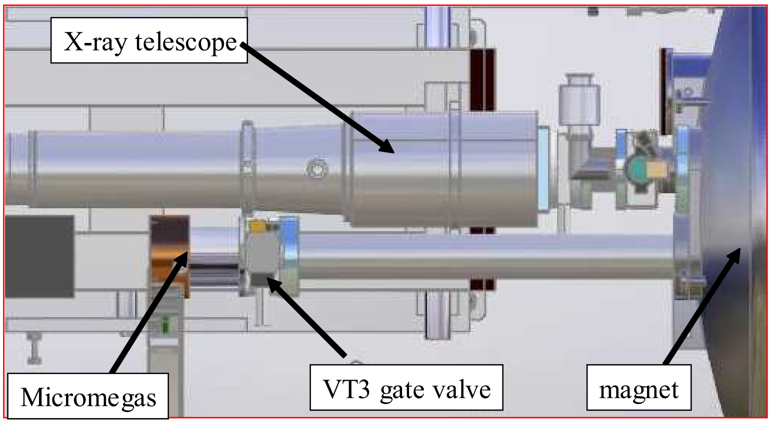

Figure 4.15: A schematic of the arrangement of the devices on the platform. The Micromegas is approximately 1 m away from the magnet volume, connected to it via a pipe.

(magnetic bearing) and of a dry primary pump.

The main detector is enclosed in a copper Faraday cage to help eliminate any induced charges into the conductive elements of the detector. The cage includes feedthrough connections for the cables connecting the high voltage, power supplies and Data Acquisition system with the detector electronic elements.

The gas mixture used in CAST is Argon-Isobutane (95%-5%). This is a flammable gas and therefore special considerations had to be made for the setup, and certain safety regulations to be met. A continuously working fan was installed on the platform, in front of the detector, not to allow concentration of any leaking gas to increase. The Micromegas Safety Box was a control box, which through the Slow Control issued another interlock, stopping the gas flow of the detector in case of a fire alarm and in case of bad vacuum in the detector.

4.3.3 Readout electronics and the Data Acquisition (DAQ)

The top part of figure 4.17 shows the general layout of the readout and data acquisition of the Micromegas. The charge on the X or Y strips is read out with the help of four Front End (FE) electronic cards based on the Gassiplex chip. Each FE card integrates 96 signals (96 strips) and operates at a maximum clock speed of 1 MHz. The cards are controlled by a CAEN sequencer with two CRAMS modules (CAEN Readout for Analog Multiplexed Signals) in a VME crate and are powered by a 6 V power supply (positive and negative). The Sequencer provides the proper timing signals (Clock, Track and Hold, Clear or Reset) to the FE cards. The CRAM modules integrate and store the total charge of each channel indicated by the signal provided by the FE cards until the software reads the data and transfers them to the PC for permanent storage and analysis.

The signal for triggering the Micromegas device is obtained through the use of a preamplifier (an ORTEC 142B), which provides the high voltage for the micromesh cathode as

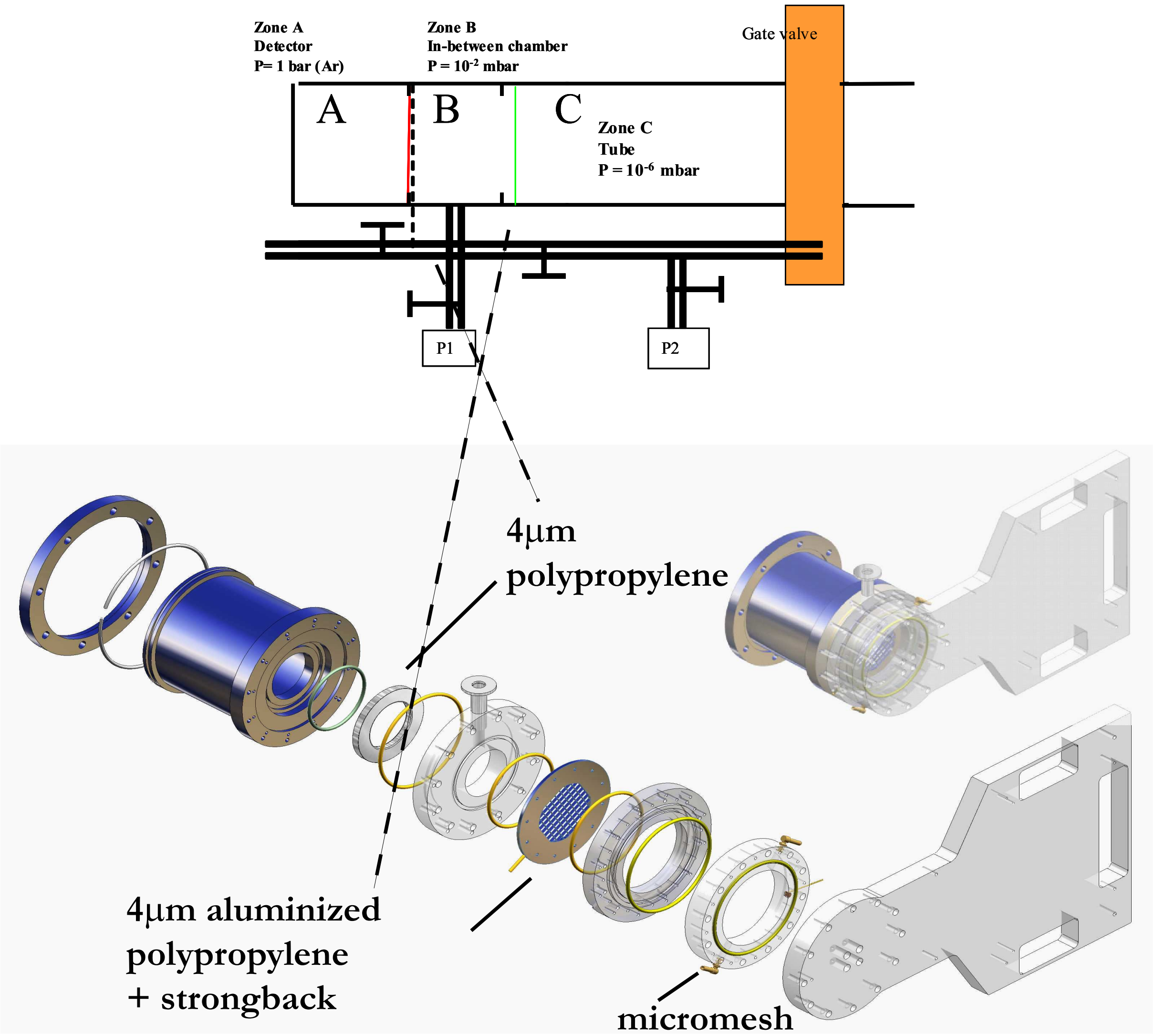

Figure 4.16: At the top, the mechanical design of the differential pumping concept. Down, the design of the several parts of the detector, blown up to the big picture in the middle. The first, aluminized window acts as the drift electrode.

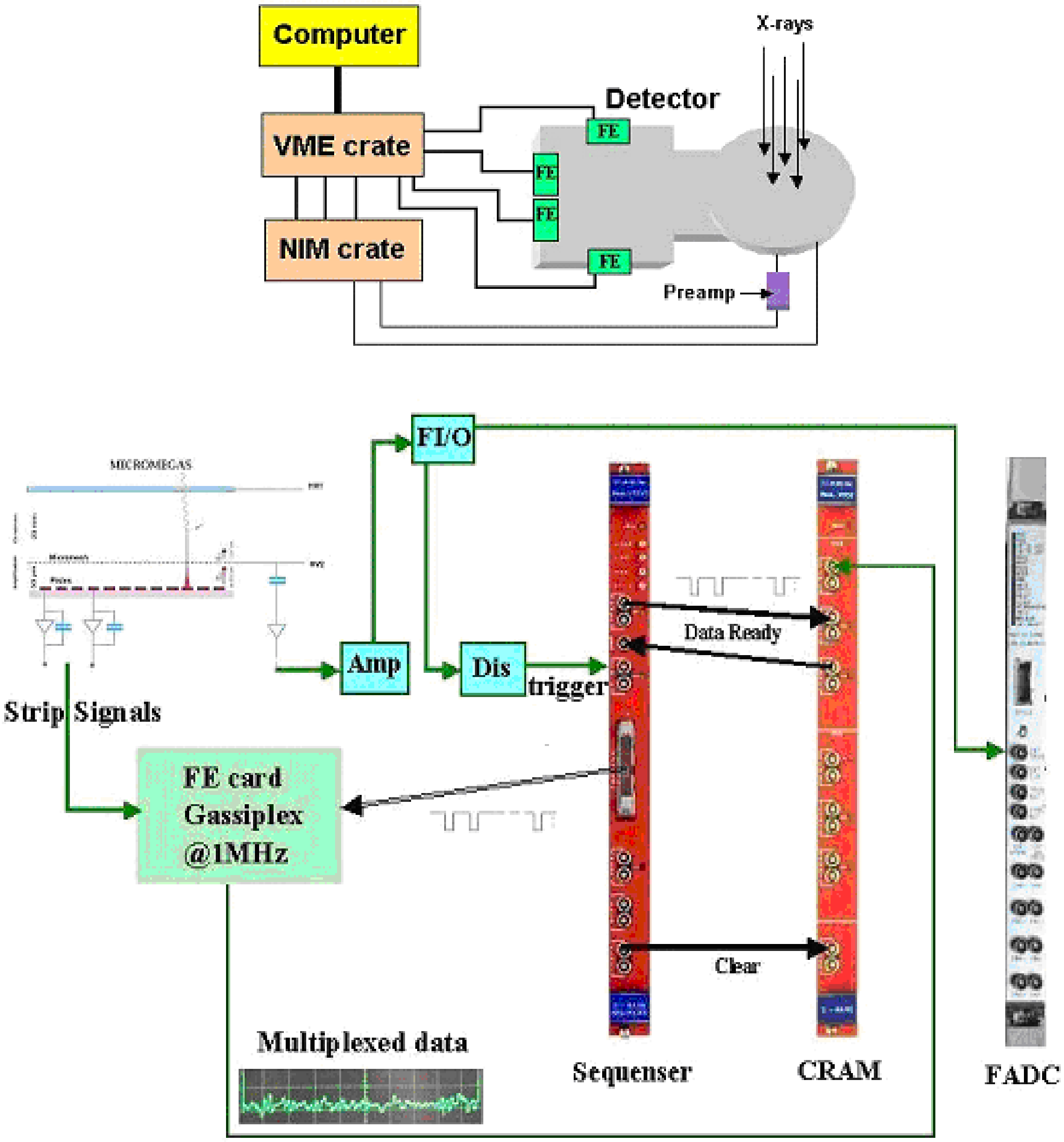

Figure 4.17: The top part displays the general layout of the Data Acquisition. At the bottom, the layout of the trigger and data readout. (The MATACQ card is noted as 'FADC')

well. The output of the preamplifier is subsequently shaped and amplified to produce the appropriate trigger signal. The trigger rate of the detector in the experiment is rather low (1 Hz), hence the zero suppression and pedestal subtraction capabilities of the CAEN modules are not utilized and all strip data are recorded.

The expected signal events (i.e. X-rays) have a characteristic mesh pulse that will be useful to the rejection of unexpected shapes for background events. In this aspect, for this Micromegas detector there is also the recording of the mesh pulse via a high sampling VME Digitizing Board, the MATACQ Board [93]. This board can code 4 analog channels of bandwidth up to 300 MHz over 12 bits dynamic range and a sampling frequency reaching up to 2 GHz and over 2520 usable points. One of these channels is used to record the time structure of the mesh pulse. The low part of figure 4.17 is a schematic of the Micromegas trigger and readout.

The data acquisition and monitoring system is based on the LabView software package, of National Instruments, and can run on a PC with either the Linux RedHat 7.3.1 (CERN release) or the Windows 2000 operating system. A dual boot PC is used to connect to the VME Controller and run the data acquisition software. The connection is performed via a PCI-MXI2 card sitting on the PCI bus of the PC, a VME-MXI2 controller card sitting on the VME and a 20 m long MXI2 cable connecting these two cards. The DAQ system was chosen to run on Linux because it provides (through CERN) the facilities of the CASTOR automatic data archiving system and the xntp software for the synchronization of the PC clock to the GPS universal time.

The online software is controlled by two LabView virtual instrument modules (VIs) (figure 4.18):

- The RunControlAll.vi, which is a state machine module controlling the initialization and start/stop of the run along with the creation of the monitoring processes.
- The RunControlAllMonitor.vi, displays the status of the run and the monitoring processes as well as the values of parameters like run number, event numbers, recording file etc.

The monitoring processes include the Event Display and the Run Monitor. The Event Display displays the X-strip, Y-strip charges and MATACQ digitizing pulse of individual events, with a frequency chosen in advance (figure 4.18). The Run Monitor performs an analysis of each event and makes one or two dimensional histograms of X strip or Y strip energies, positions and any other quantities of monitoring interest. All processes run asynchronously and communicate to each other via global variables.

The first tests

To precisely determine several parameters of the detector, the two first prototypes[1] were transported and mounted at the PANTER [94] facility of the Max Planck Institute (MPE)

---

[1] These very first modules had an additional buffer space between the vacuum window and the drift electrode, which was filled with Helium gas at atmospheric pressure. The conversion gap was 18 mm and the amplification gap 50 μm.

in Munich (figure 4.14), after the X-ray focusing optics [95]. This facility, designed for the calibration and characterization of X-ray telescopes, provides a parallel X-ray beam with a very accurately calibrated energy and intensity.

The purpose of these tests was to prove that this Micromegas design can be used in the CAST experiment with or without the focusing telescope. In addition, it was a good opportunity to test some commercial vacuum windows and various gas mixtures, of Argon or Xenon, were tested. The capability to determine the position with the X-Y readout as well as to detect low energy photons was proven for the first time (figure 4.19).

During these tests, with highly controlled X-ray beams focused by the X-ray telescope, the background rejection capability of this particular design Micromegas detector was shown. Long background data runs were taken and they were processed by the same means as the real photon beam data to determine the software efficiency. The background remaining after all cuts within $8 \times 8\,\mathrm{mm}^2$ around the focus area of the telescope was found to be: $2.5 \times 10^{-6}\,\mathrm{events\,s^{-1}keV^{-1}cm^2}$ with 47% efficiency. The excellent linearity of the Micromegas detector was also shown as well as its good energy resolution during these early tests.

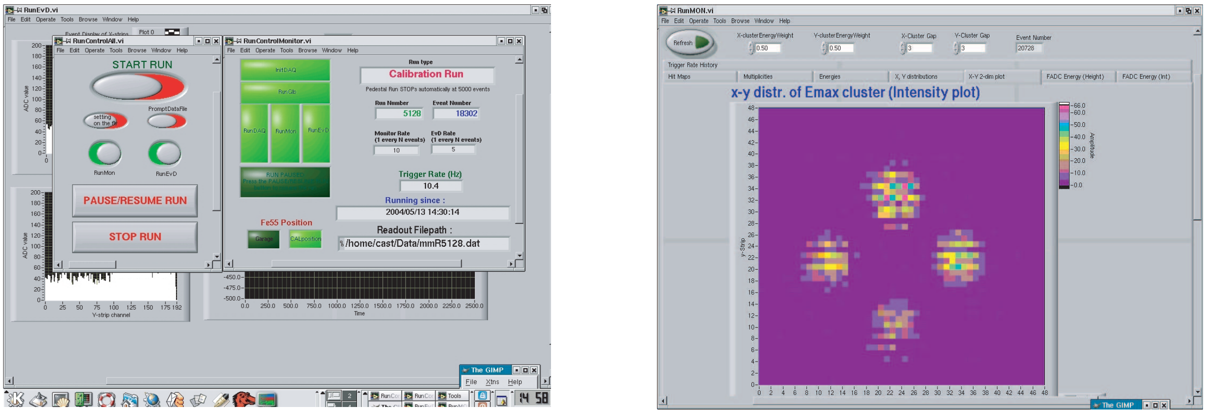

Run type: Calibration Run

Pedestal Run STOPs automatically at 5000 events

Run Number: 5128

Event Number: 18302

Monitor Rate (1 every N events): 10

EvD Rate (1 every N events): 5

Trigger Rate (Hz): 10.4

Running since : 2004/05/13 14:30:14

Readout Filepath : /home/cast/Data/mmR5128.dat

Figure 4.18: The modules of the Micromegas acquisition: the control VIs as described in the text left, and the on-line view of the data (right)

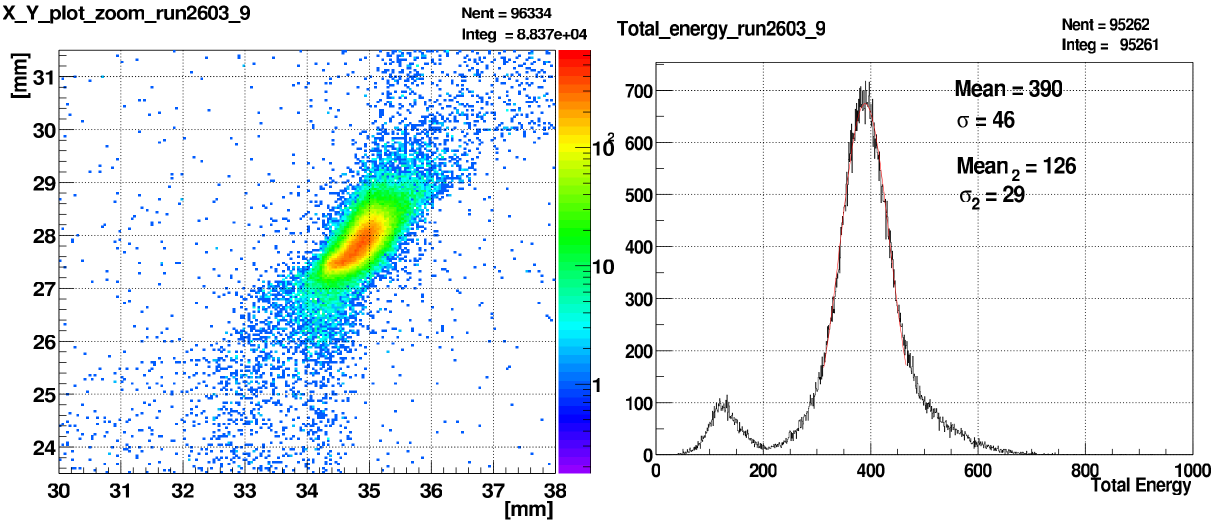

Figure 4.19: Left: The intensity plot (logarithmic) of the X-Y position of 4.5 keV photons at the focusing point, with the set up in Panter. The size of the point-like beam, some mm is distinguishable. Right: the energy spectrum of a 4.5 keV beam , showing the very good energy resolution of the detector. The peak at 1.5 keV is the escape peak of the Argon.

Chapter 5

The Search for Axions with MICROMEGAS

CAST was taking data in 2003 for six months. In spite of some interruptions, the Micromegas detector was looking at the Sun for approximately 120 h and for ten times more hours it was taking background data. A part of this was used to derive an upper limit of the coupling constant of axions to photons, as it is presented here.

5.1 The 2003 Data taking

The data taking period for the year 2003 started on the 1st of May, and ended on the 13th of November.

These six-and-a-half months were not uneventful; the problems that came up were successfully faced most of the times, at the cost of data-taking time, though. The most serious event was a mechanical problem that appeared on the 1st of June: a problem of gripping in the magnet lifting mechanism appeared and magnet movement was stopped on the 31st of May. Apparently the moving system was too constrained, and in order for data taking to restart in a short time, some more play was added to the lifting system and at the same time the lubrication system was improved. Six weeks later, data taking was resumed.

Several quench signals (most of which due to loss of utilities, water, electricity and a configuration error) resulted in the loss of many trackings, both in the morning and

Table 5.1: The hours of data taken by the Micromegas detector in 2003, separated in Sets.

	Dates	Background [h]	tracking [h]	Set Characteristic
Commissioning data	01.05 - 07.08			
Set A	08.08 - 16.09	374.8	42.2	Implementation of MATACQ Board
Set B	17.09 - 06.10	121	11.5	Change in the shaping time
Set C	08.10 - 13.11	251	21.8	Implementation of attenuator

in the afternoon. And last, in early November, an accident caused another break in the data-taking: a cable support attached to a moving arm 1.5 m above the platform where Micromegas and the X-ray telescope system are sitting got unhinged and fell on these detectors. Data-taking was resumed after insuring there was no damaged caused on the telescope or the detectors, and after the cable-tray was put in place.

Throughout this time, there were changes on the part of Micromegas as well, some forced and others introduced in order to improve the performance of the detector:

After 3 weeks of full operation, at the end of May, the detector showed a problem on the strips' readout, more than ten strips appeared not to be working. The problem was traced back to be bad connectors on the detector of the electronic cards reading the strips. As a consequence the detector was replaced by a new one, V3. While taking background data in late June, a window was broken and the loss of pressure lead to a contamination of the gas pipes system (oil from the output bubbler was taken in), which was consequently changed. At that time, a pick up noise was noticed on the data while the motors were on. The threshold of the trigger was raised from approximately 0.6 keV to close to 1, keV, which was enough to overcome the noise.

V3 was practically in its commissioning phase when data taking was resumed and several changes were made from then on, constantly improving its characteristics. In August, the MATACQ board was already installed with the intention that the data acquired would include more information. In the middle of September, the shaping time of the shaper unit of the preamplifier's signal was changed in a try to include the 8 keV peak clearly in the energy range of the detector. In October, an attenuator was added, with the aim to increase the energy range of the pulse taken from the mesh. As a result of these improvements 3 data sets emerged, denoted as SetA, SetB and SetC from now on.

The quality of the data taken after the implementation of the MATACQ board reading the mesh signal was clearly better in comparison to the 3 weeks of data taken in May (different detector). Hence, for the analysis those three weeks of data were not considered. In the period between August and November, the Micromegas detector had gathered

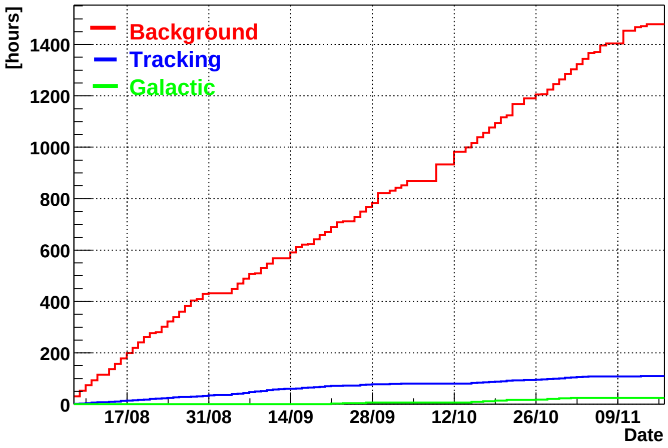

Figure 5.1: The accumulated hours of background and tracking for the Micromegas detector in 2003. In green (right low part), called “Galactic” are shown the hours that CAST was pointing to other X-ray sources than the Sun (see section Collateral). The numbers shown are the total number of hours of data taken, out of which only 810 h of background and 77 h of tracking data was used.

approximately 120 h of tracking and 1500 h of background data out of which 77 h of tracking and 810 h of background data were used (figures 5.1, 5.2).

Data-Taking Protocol

The data taken by Micromegas belong to four different types: *pedestals*, *tracking*, *calibration* and *background*. For the best handling of the data, it was decided that a separate file will be taken every day for each type. The pedestal run consisted of 5000 events taken when there was only internal triggers. While the magnet was aligned with the Sun during sunrise, the tracking data were gathered. To calibrate the detector, a file of approximately 25000 events was taken every day with a ^{55}Fe X-ray source. The data outside these times, were considered the background events.

5.2 The Analysis of the 2003 data

As it has already been mentioned, Micromegas uses two different readouts: the strips, and the signal of the mesh (through the preamplifier). The analysis follows both sources and uses combined information for the identification of the events. The detector resolution

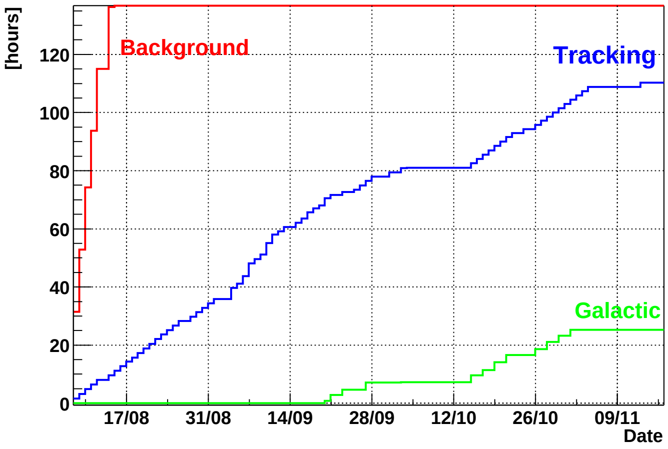

Figure 5.2: A zoom of figure 5.1 on the lower part of the plot.

will allow to distinguish events issued from X-rays from background events taken into account their energy, topology and time structure. In order to set the sequential criteria to reject background events, the calibration spectra obtained from a ^{55}Fe source will be used. In these spectra, two peaks are present, the main peak at 5.9 keV and the Argon escape peak at 3 keV. The axion expected spectrum has a mean value of 4 keV, therefore this source is quite suitable to deduce efficiencies in the range of interest.

At this point, the "event" should be defined:

Event: the readout of the integrated number for every strip (384) and 2500 samples from the mesh signal after a trigger.

The standard procedure followed from the raw data to the results passes through the following steps:

- Low Level part I
    - For the strips :
        - Reading raw data
        - Pedestal subtraction - strip trigger
        - Clustering
    - For the mesh Pulse:
        - Reading pulse data
        - Pulse Shape Analysis - Identifying peaks
- Low Level part II: The information characterizing the pulse stored in the previous step is later archived and stored in a ROOT Tree (an advanced ntuple) [96].
- High level: This is the level where the information, rapidly fetched by the access to the tree files, is subject to several conditions that the formed "X-ray" profile suggests. After this step, any events surviving are considered X-rays.

5.2.1 Strips

Pedestal subtraction

In order to acquire the charge collected by the strips, it is necessary to calculate and subtract the pedestal of every strip. The pedestal corresponds to the mean value of the charge (in the same ADC units) measured by the strips when there are no real triggers. A special file was taken regularly (usually once a day) out of which the level of the pedestals was calculated with an iteration method, in order to exclude real signals that might have occurred during the reading. This level is afterwards subtracted from each strip. Figures 5.3 and 5.4 show the level of the pedestal for every strip with the corresponding sigmas. The sigma of the pedestals is subsequently used to determine a trigger. Only strips with a signal above 5 pedestal sigmas are considered to have fired and will be processed for the next step, the clustering.

Clustering

After the subtraction of the pedestals, the strips that have fired are identified and grouped: neighbouring strips (at least 3 in number[1]) that have a gap of less than 3 strips between them, form a cluster. Another group of at least 3 consecutive strips that lie farther than 3 strips away from the other cluster, form a second cluster in the event.

By this point several characteristics taken from the strip information regarding each event found are recorded:

Event ID The identification number given to the event by the DAQ.

Event time The time stamp of the event in ms.

Number of Clusters The number of clusters found in the X strips as well as in the Y strips is stored separately.

Center The position of the barycenter (in strip number × strip width) of each cluster.

Sigma The FWHM of the distribution of the cluster.

Multiplicity The number of strips forming the cluster. (The minimum multiplicity for a cluster is 3)

Charge The sum of charges of each strip of the cluster.

Total Charge The total charge gathered in each of the electronic cards (corresponding to 96 strips).

---

[1] The charge distribution of a localized energy deposition (which approximately is the case of X-rays) exceeds three strips, after the diffusion in the gas volume.

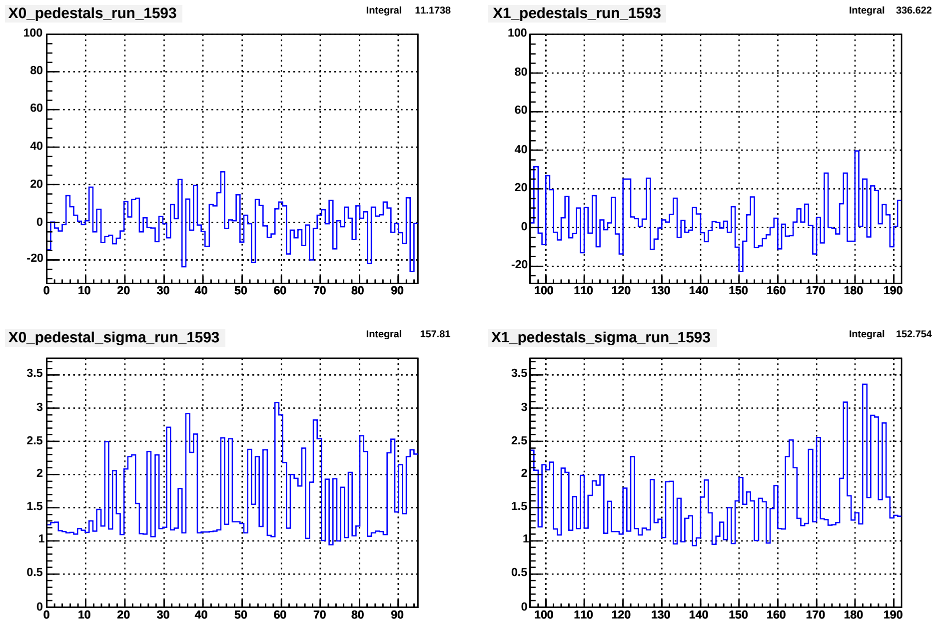

Figure 5.3: The pedestal level for the two electronic cards reading the X strips (upper part). The corresponding sigmas are plotted below. It should be noted that both the level and the sigmas were quite stable all through the year.

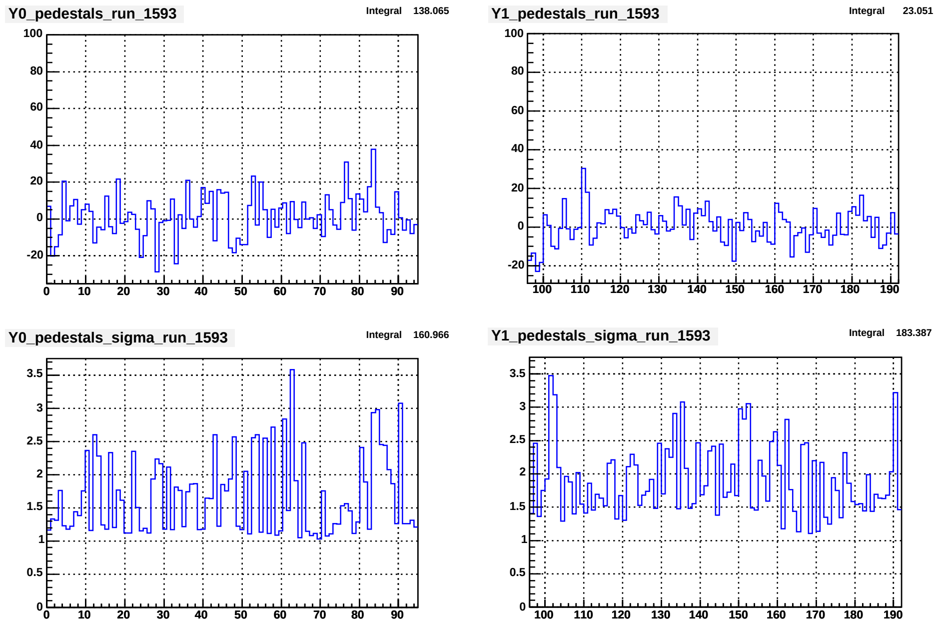

Figure 5.4: The pedestal level for the two electronic cards reading the Y strips (upper part). The corresponding sigmas are plotted below.

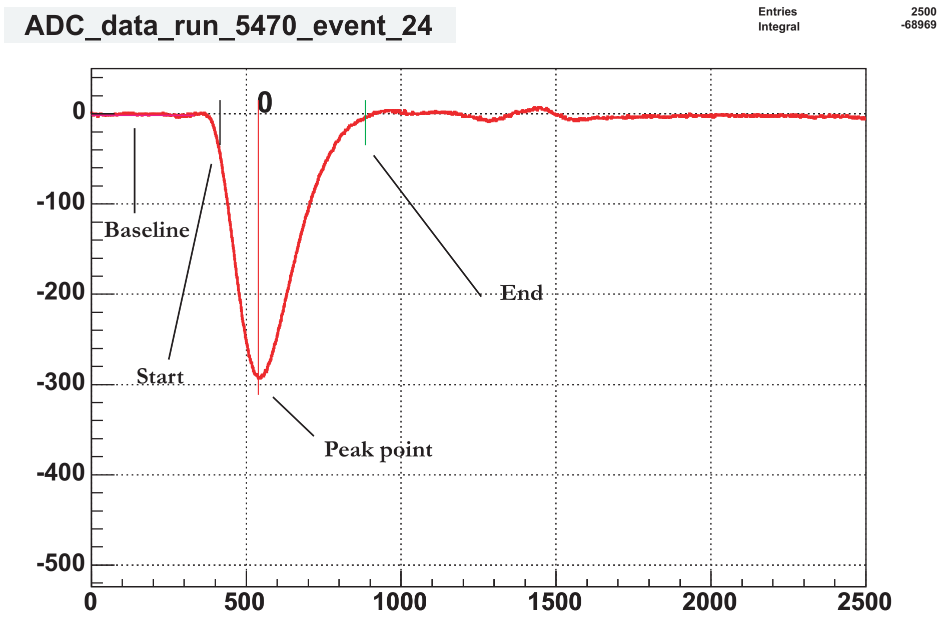

Figure 5.5: A drawing of a pulse from the mesh, reproduced with the help of the data stored. On the figure, some of the parameters of the pulse as defined in the text can be seen.

5.2.2 The signal from the mesh

After the treatment of the strips' data, the data coming from the MATACQ card is read. A simple pulse shape analysis on this data is performed to extract the information of the pulse. Figure 5.5 shows an example of a pulse, taken from a calibration.

Baseline The baseline is calculated as the mean value of a given sample of points between the start of the pulse and the start of the peak using the pre-sample range (where there is no signal).

Baseline Fluctuation It is the calculated standard deviation of the baseline.

Peak time The time at which the Pulse has reached its maximum height.

Amplitude It is the height of the pulse at the peak time, baseline corrected.

Start time The start time of the peak is considered as the time when the pulse reaches the 15% of its height, corrected for the baseline.

Risetime The rise time of the pulse is defined as the time interval from the start time, until it reaches the 85% of its height.

End time As the end time is taken the point where the pulse reaches the baseline level within its fluctuation.

Integral It is the area of the pulse, integrated from the start time till the end time.

Default Integral The area of the pulse that extends from the Start time for 500 ns, defines the Default Integral.

Rise Integral It is the integral of the pulse during the risetime.

PileUp flag The evolution of the derivative of the cumulative distribution of the peak should follow a well characterized pattern for the case of a single X-ray signal. The flag indicates if the pattern of the pulse is accepted (value equal to 0) or more composite and therefore rejected (values above 0).

5.2.3 Calibration

Apart from the data file and the pedestal file taken everyday, as mentioned before, there were Calibration files taken; these are data files taken with the detector exposed to an X-ray source. Because of the experiment's set up, the source could not be placed in front of the detector, therefore it was placed at the back. For this reason, four holes were opened on the back of the detector's support, to allow the passage of the X-rays. The source was held in position with the help of a cylindrical tube with a shutter. Whenever a calibration was needed, the shutter would be removed and the source would directly be pointing at the four holes. The distance between the detector and the source was approximately 12 cm, enough to cover the four holes at the same time and give a rate of about 10 Hz.

The calibration data was giving valuable information in two aspects: first of all the actual energy calibration of the instrument, and secondly – but equally important – it was providing the information to create the profile of the X-rays in the detector. This profile would be later used to discriminate background events from X-rays. The source used mostly was a ^{55}Fe of the intensity of 15.8 MBq, although a ^{109}Cd source was used occasionally. In figures 5.6 and 5.7 the energy spectra of a ^{55}Fe source are shown, using strip and pulse information, where the energy resolution can be seen.

The strips' energy resolution is expected to be poorer than the one of the mesh signal, when taking into account that one sums over many channels (and their errors), the way the integration is performed and the fact that there might be dead strips. And yet, the resolution was quite lower than expected. This was attributed to the fact that there seemed to be some "cross-talk" between the X and Y strips (figure 5.8), making the information collected by the strips not very accurate[2]. For this reason, in the 2003 data

---

[2] The pillars that hold the micromesh above the strips' plane, end to a very thin layer of copper. Their diameter being approximately 75 μm, just around the distance between a strip and a pad, it is possible that they touch the two, connecting them electrically. Because of this electrical connection, it might happen that some of the signal in one X strip can be transferred to neighbouring ones, or even appear as if it were read by the Y plane.

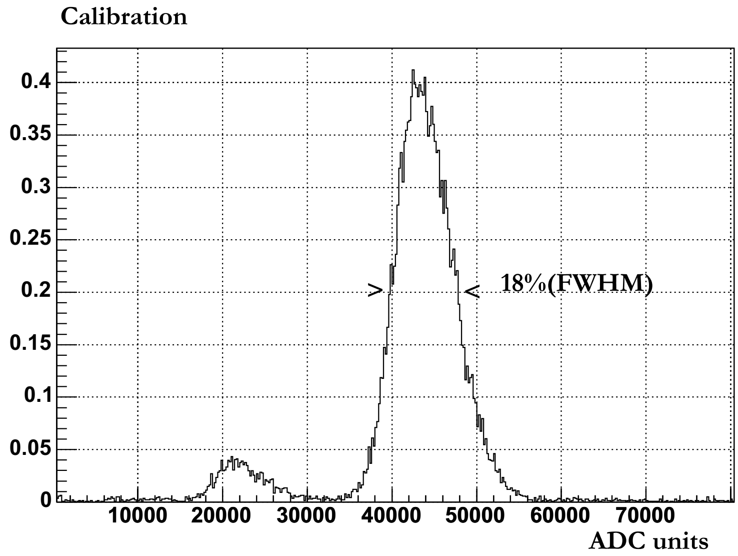

Figure 5.6: The energy spectrum from a ^{55}Fe source as seen at the mesh. The energy resolution at the main peak, 5.9 keV is 18% (FWHM). The Argon escape pea at 3 keV is also visible.

analysis more weight was given to the information gathered by the mesh. The detector's gain was rather stable during the operation, as figure 5.9 shows.

5.2.4 Building the X-ray profile

The pulses generated by an X-ray source are used as the guide for making a list of requirements an event should fulfill in order to be accepted. The calibration files are used for this purpose. After exploiting the information given by these events, the following conditions were formed:

Table 5.2: Details on the Rise Time condition for the FADC pulses: the mean value of the gaussian distribution and the sigma. The condition excludes events outside a region denoted by 3σ around the mean value. (The limits on the condition are optimized to maximize the ratio efficiency/background rejection.)

	Mean value at 3 keV	σ	**Mean value at** 5.9 keV	σ
SetA	105.6 ns	2.5 ns	105.2 ns	1.5 ns
SetB	56.5 ns	2.9 ns	56.8 ns	1.45 ns
SetC	56.2 ns	2.1 ns	57.0 ns	1.4 ns

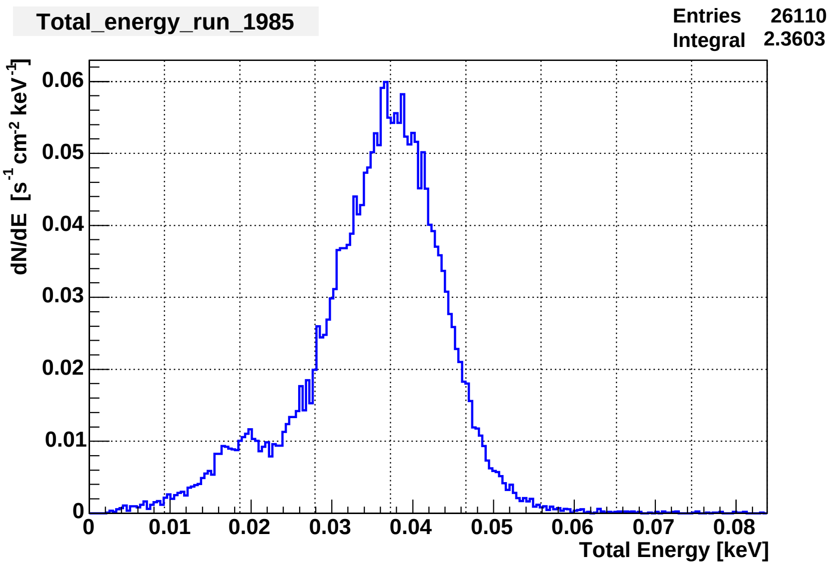

Figure 5.7: The energy spectrum from a ^{55}Fe source formed with the charge collected at the strips. The energy resolution at 5.9 keV is 32% and very low at 3 keV (the Ar escape peak). It is straightforward there is a problem on the strips' information.

Table 5.3: The expressions of Conditions 2 and 3

	Equation expression
Condition 2	$\text{Amplitude} > a_1 \times \text{StripsCharge} + b_1$
	$\text{Amplitude} < c_1 \times \text{StripsCharge} + d_1$
Condition 3	$\text{Multiplicity}_y > a_2 \times \text{Multiplicity}_x + b_2$
	$\text{Multiplicity}_y < a_2 \times \text{Multiplicity}_x + b_2$

1. The X-rays interacting in the detector are expected to have the same risetime, regardless of their energy. The condition on this quantity excludes events outside a region denoted by 3σ around a mean value (Table 5.2). The effect of the condition on a calibration and a background file is evident in figure 5.11. In fact the good precision of the estimation of the risetime is evident in figure 5.10; the mean value of the risetime at 3 keV differs from the ones of 5.9 keV by 0.5 ns to 1 ns. This small difference could be explained by the fact that the mean free path of the electrons differs for the two energies, it is true that the lower energy photons could have a slightly smaller risetime.

2. Basic information on the profile is provided by the multiplicity of the event. In particular the plot of the multiplicity in one direction versus the multiplicity in the other is rather revealing. The plot shows that good events lie in a diagonal zone

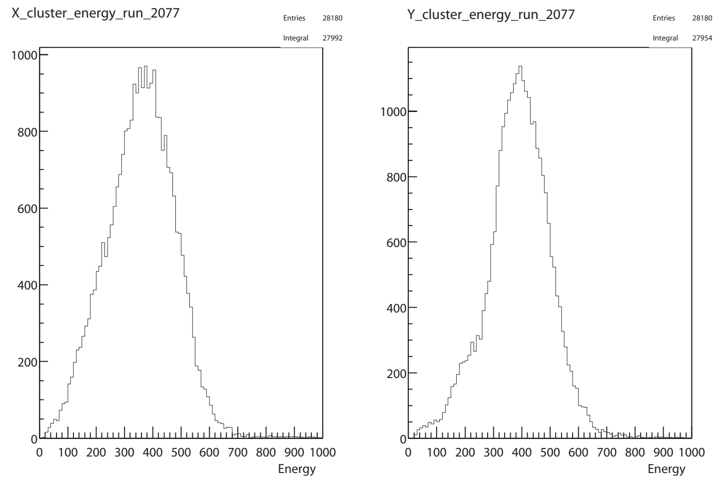

Figure 5.8: The bad energy resolution on the strips can be explained by “cross-talk”, introduced by electrical connection between neighbouring strips or strips of the other direction. An optimization of the read-out plane would decrease the possibility of such occurrences.

delimited by two lines (Tables 5.3 and 5.4 provide the information on the condition). After applying this condition, the plots in figure 5.12 were produced.

3. The usefulness of the two different readouts of the detector (mesh pulse and strips) as well as that of the two-dimensional plots, is proved in the following condition: plotting the amplitude of the mesh pulse versus the energy deposited on the strips, the X-ray events have left almost the same energy on the strips as the one collected by the mesh; two lines (Tables 5.3 and 5.4) restrict the accepted events to be those sitting in between them (figure 5.13).

4. Going back to figure 5.12 can be seen that, essentially, without a loss in the efficiency, one can restrict the maximum allowed multiplicity of an event to be 18 strips.

Efficiency of the selection criteria

The calculation of the efficiency of these conditions was not an easy task. In order to keep the ratio of “pure” X-ray events over background as high as possible, the area of the 4 holes used was small (a radius of 2 mm). The principle of the calculation was to study the effect of the conditions on the two peaks (3 keV and 5.9 keV, taken from the mesh pulse) of the calibration spectra, counting the number of events before and after the application. However, several correction factors had to be taken into account, to this obvious definition.

- The contamination of background events (mainly cosmic rays) in the area of these small holes is taken into account. After having calculated a mean background rate

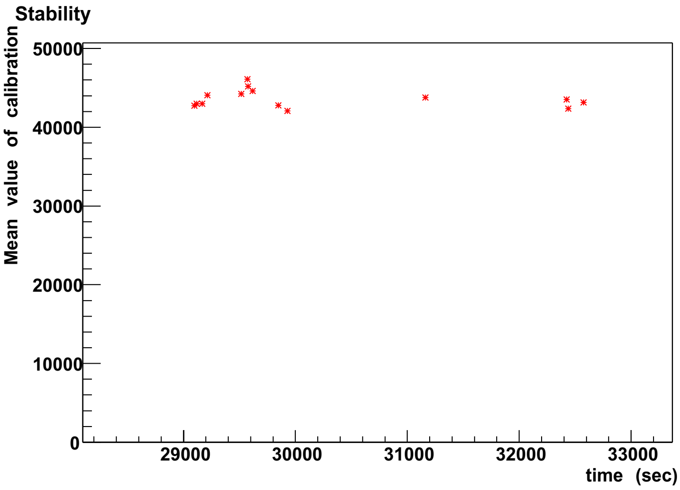

Figure 5.9: The mean value (in ADC units) of the 5.9 keV ^{55}Fe peak in function with time (information taken from the mesh pulse). The stability is remarkable, since the highest deviation of the mean value is of the order of 6% .

for every set, a number of expected background events for the duration of the calibration run was estimated.

- The second factor were events that have a 'double' cluster; the mesh pulse does not always include them, but the strips collect them. The pulse analysis classifies these events as 3 keV, while the strips classify them at 6 keV. The result is a population of events (figure 5.14) that when excluded, the loss would be attributed to the 6 keV peak and not to the 3 keV.

Taking these factors into account, Table 5.5 was filled, when the conditions were applied in the same sequence as described.

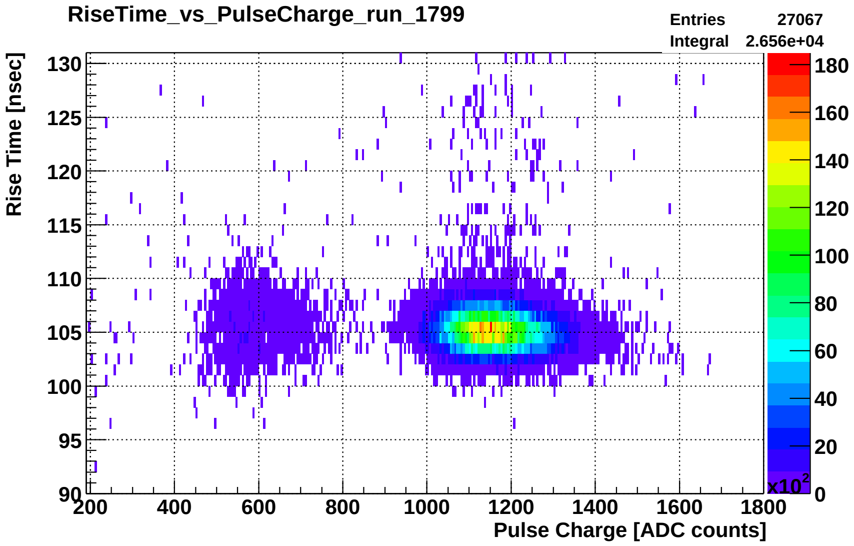

Figure 5.10: The plot of the risetime versus energy. in the lower energy part some events with a smaller risetime can be seen, indicating that the lower energy events could have a lower risetime because of the longer drift time they could have.

Table 5.4: The values of the parameters of the expressions in Table 5.3

Condition 2				
	a_1	b_1	c_1	d_1
SetA	0.34	25	4/6	100
SetB	500/150	0	150/500	250
SetC	500/1800	0	250/800	100

Condition 3				
	a_2	b_2	c_2	d_2
SetA	5/6	-25/6	4/5	8
SetB	17/19	-5.4	14/130	6
SetC	17/19	-5.4	14/130	6

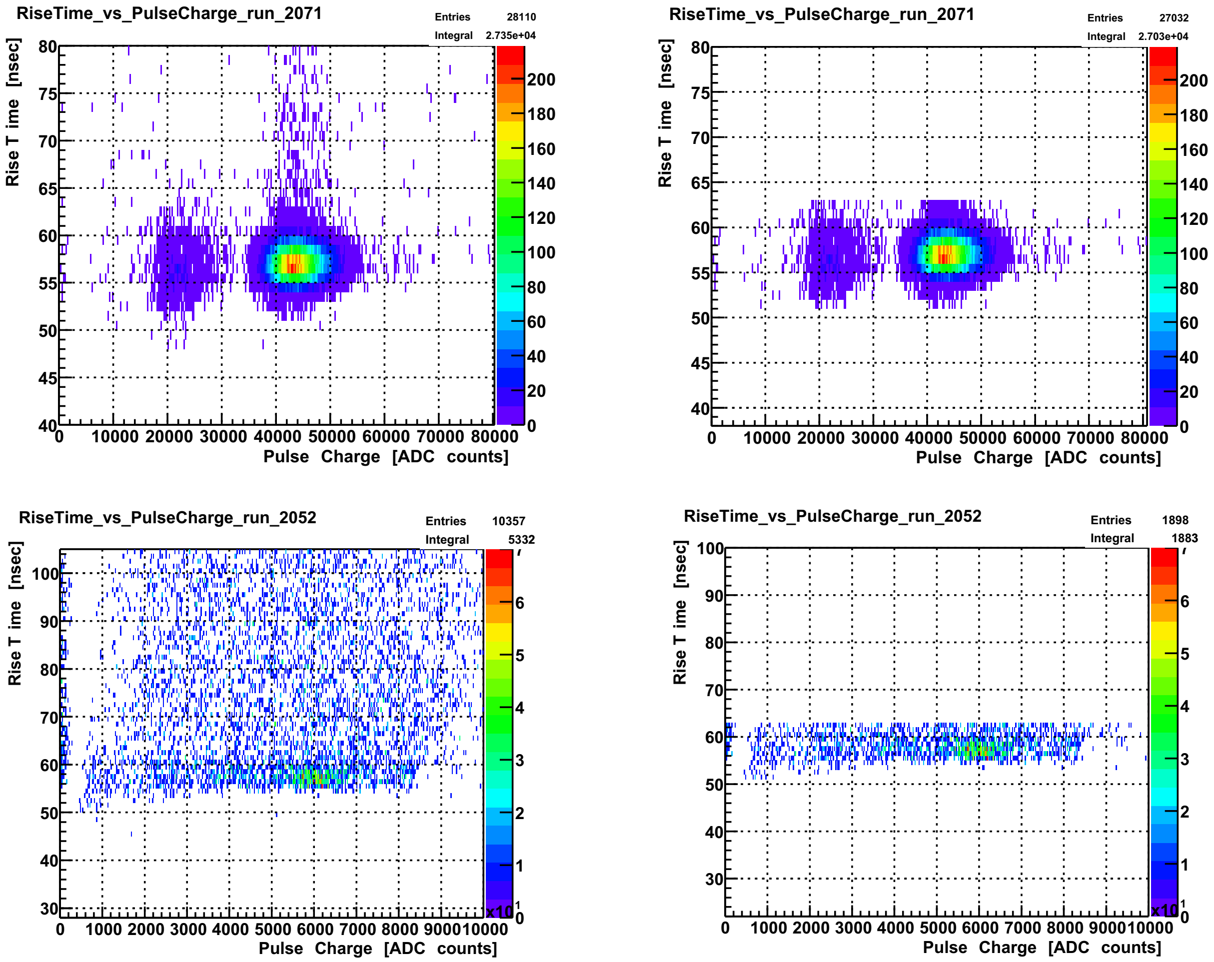

Figure 5.11: The risetime plotted with respect to the energy. The top row comes from a calibration run, showing the distribution before and after the condition, while the lower part shows the same in a background file.

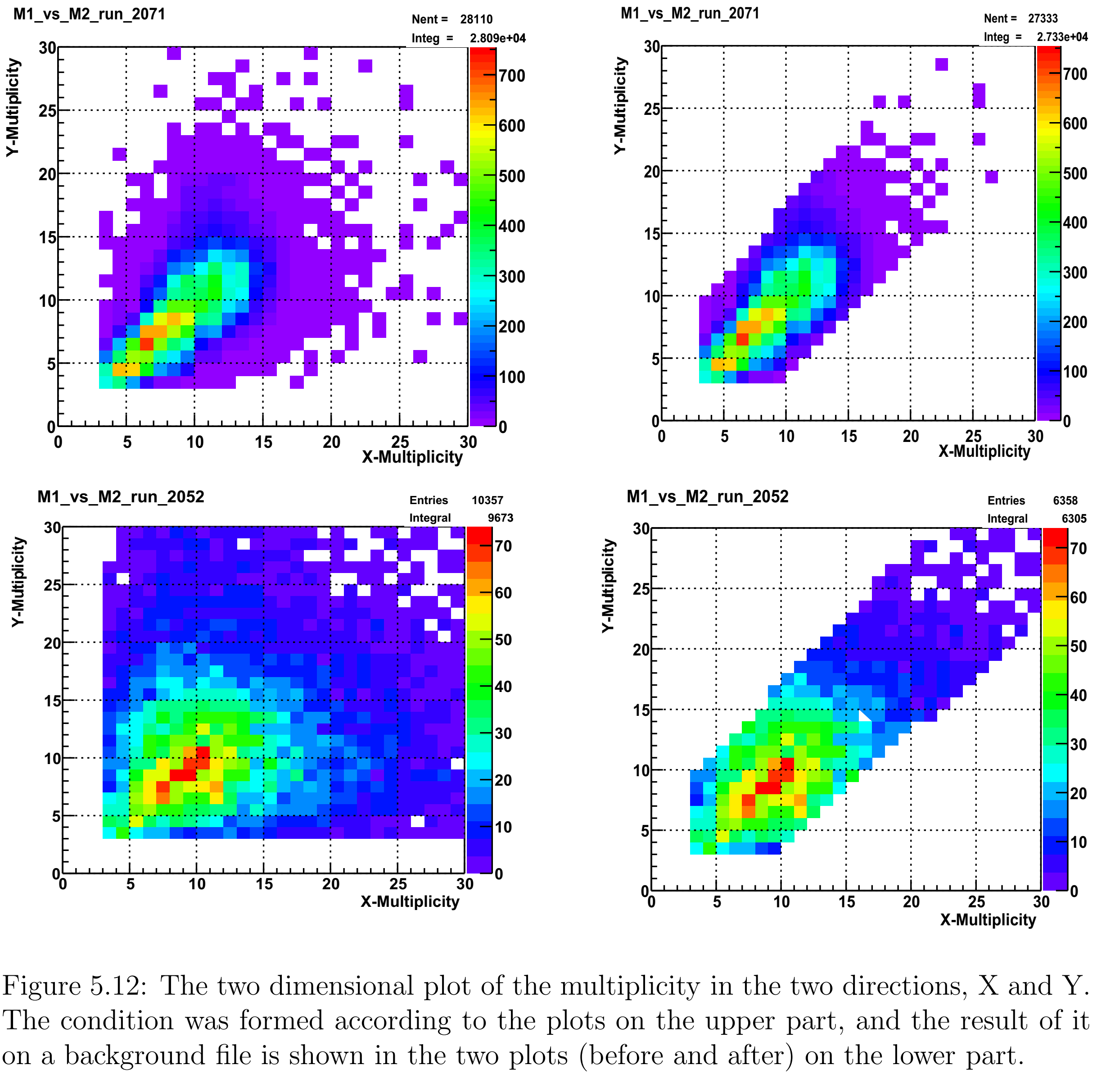

Figure 5.12: The two dimensional plot of the multiplicity in the two directions, X and Y. The condition was formed according to the plots on the upper part, and the result of it on a background file is shown in the two plots (before and after) on the lower part.

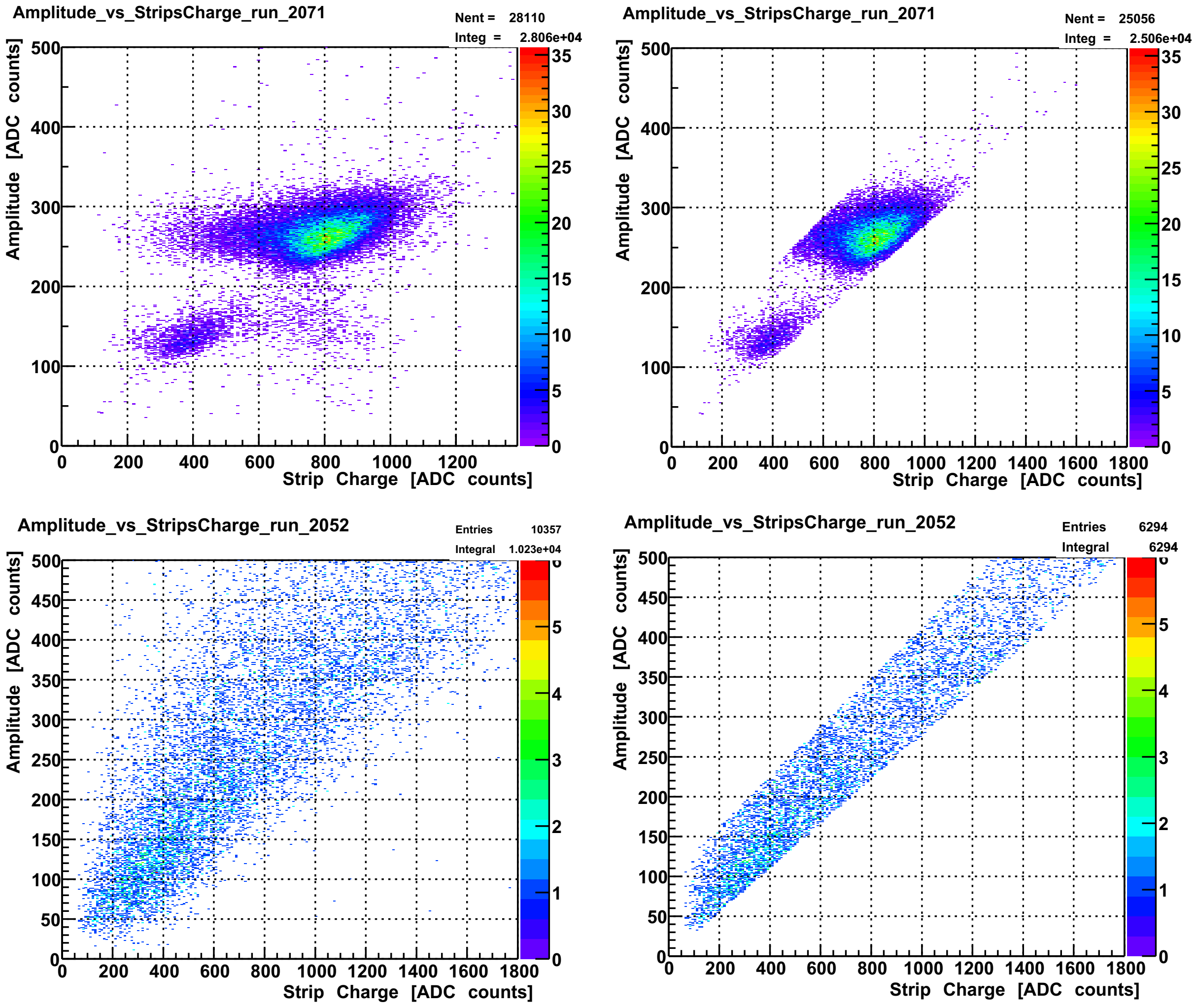

Figure 5.13: Similarly for the amplitude plotted versus the strip charge the calibration files (upper part) show the events' preference for a diagonal region, which forms the condition later applied on the background events (lower right).

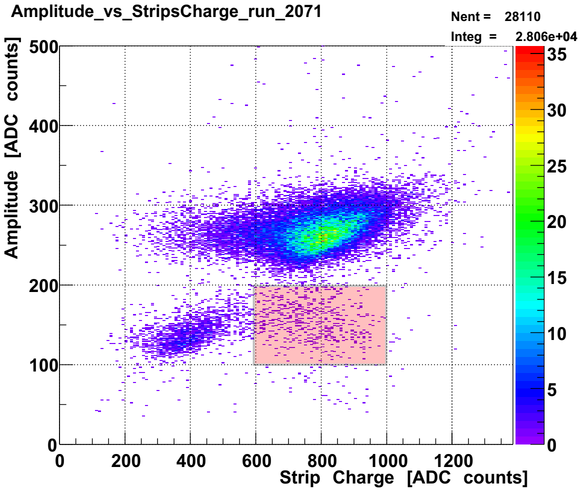

Figure 5.14: The plot shows events that have left an energy of 3 keV on the mesh but 6 keV on the strips (shaded area). for a correct estimation of the efficiency of the conditions, a correction was applied for this population of events.

Table 5.5: The efficiency of every condition, when applied sequentially to the data. The statistical error is less than 1%.

Set A	3 keV	6 keV
Condition 1	97.1%	97.1%
Condition 2	96.3%	96.3%
Condition 3	94.6%	93.7%
Condition 4	94.5 %	92.4%

Set B	3 keV	6 keV
Condition 1	98.7%	97.6%
Condition 2	97.7%	95.9%
Condition 3	96.3%	94.8%
Condition 4	96.3%	94.8%

Set C	3 keV	6 keV
Condition 1	94.4%	98.3%
Condition 2	93.4%	97.4%
Condition 3	86.1%	85.6%
Condition 4	86.1%	85.5%

Hardware efficiency

The detectors used for data taking were different versions of the detectors tested in PANTER. In order to be conservative, the efficiency curve was not used directly [95]. However, it was used in an indirect way, to verify the outcome of the simulated efficiency.

A simulation was performed, using the GEANT4 package [97]. The code was fed with a simple geometry fitting the characteristics of the detectors used in PANTER (conversion gap, diameter, etc.), the dimensions and chemical composition of the window, as well as running conditions like the composition of the gas flushed in the detector. The photon beam shot towards the detector was such to simulate the narrow beam provided by the PANTER facility. The result of the simulation is the line in figure 5.15. The good agreement between the line and the points measured in PANTER (the accuracy of the intensity given is 10%), allows to use the simulation to estimate the hardware efficiency of the detectors used in CAST that were not tested in PANTER.

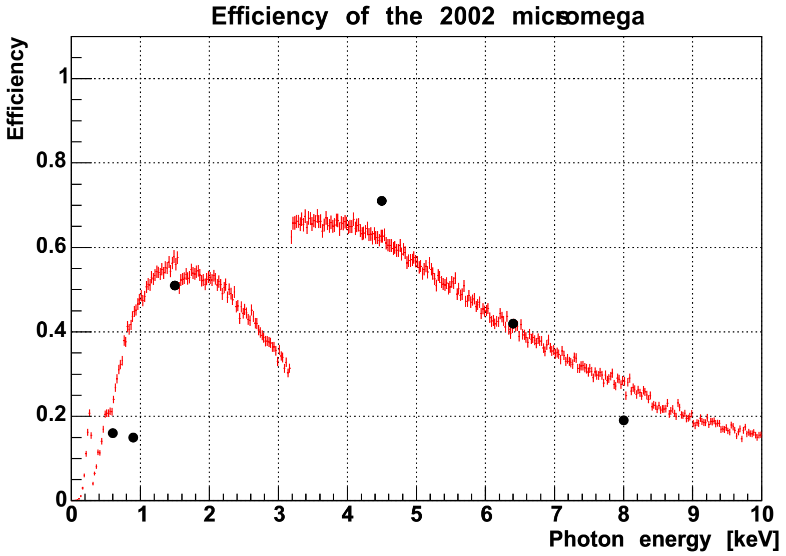

Figure 5.15: The hardware efficiency of the Micromegas in PANTER: the points are the efficiency calculated for the beams received [95]. The solid line represents the simulated hardware efficiency for the same detector. The Argon absorption line at around 3 keV is clearly visible. The efficiency of the 0.9 keV point was most probably underestimated.

In order to do that, the new parameters of the detector of interest are inserted in the code. This time the used photon beam is such that resembles the axions coming through the bore of the magnet. The efficiency curve obtained for the detector used in the first year of Phase I of CAST (V3) is shown in figure 5.16. The overall hardware efficiency of the detector in the range $1-10\,\mathrm{keV}$ is 59%.

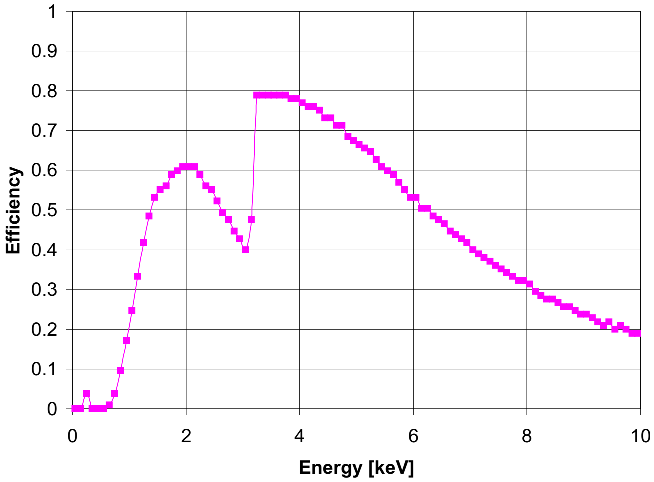

Figure 5.16: The curve of the hardware efficiency of the detector V3 used in the first year of data taking in CAST .

5.2.5 Spectra

As mentioned before, one file contained the tracking data for each day, and another one (or more) the background one.

While tracking the Sun, a signal is expected to appear only within the area of the detector that is equal to the one of the magnet bore (that is 43 mm) and only when the magnetic field is on, and –of course– only if the detector is not blind to it, meaning that the valve to the magnet is open[3]. The check of these requirements was done with the help of the Slow Control and the program responsible for the movement of the magnet, both of which store this information.

To avoid systematic effects, such conditions were required for the background data taking time. Although after this the statistics were lower, the background events were still one order of magnitude more than the tracking ones.

After having passed this first step, the events are subject to the conditions described, and the final spectra were produced. In figures 5.17, the tracking (red) and background (black) spectra are overlapped, for each of the three sets. The shape of the distributions is the same, with the prominent peak of copper at $\sim 8\,\mathrm{keV}$, attributed to fluorescence. The background level achieved is remarkably low (at $10^{-4}\,\mathrm{counts\,s^{-1}cm^{-2}keV^{-1}}$, for energies below $7\,\mathrm{keV}$. A summary on information regarding the level of the spectra and the exposure times, is given in Table 5.6.

---

[3] This conditions are the reasons why not all hours of background data are used.

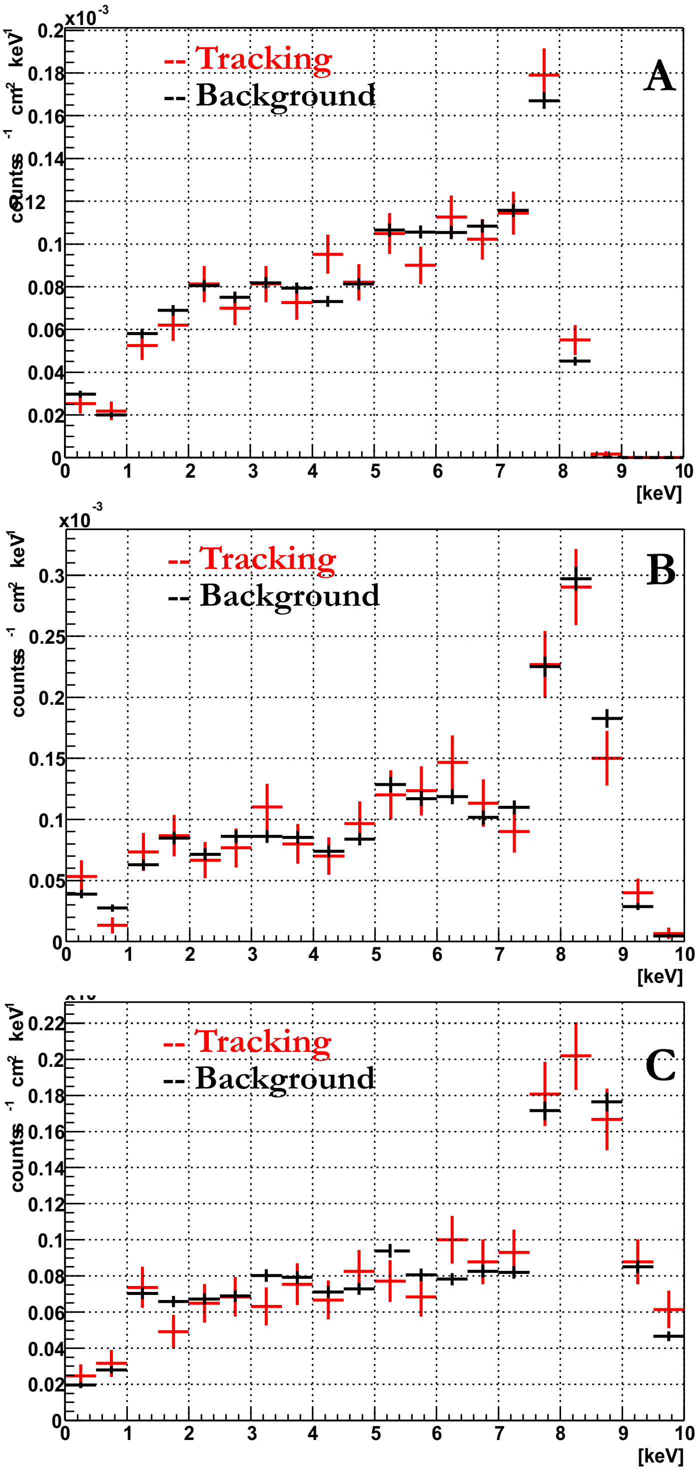

Figure 5.17: The tracking spectra (red crosses) plotted over the background spectra (black crosses) for each data set of 2003.

Table 5.6: Details on the exposure time and level ($1-7\,\mathrm{keV}$) per set of data.

	Background hours	Level (cts/cm^2/keV)	Tracking hours	Level (cts/cm^2/keV)
Set A	431.4	8.5×10^{-5}	43.8	8.4×10^{-5}
Set B	121	9.17×10^{-5}	11.5	9.7×10^{-5}
Set C	251	7.59×10^{-5}	21.8	7.31×10^{-5}

Systematics

The first step towards reducing any systematic effects on the data, was to use background data only at the same magnet conditions as the tracking data was taken: valves to the magnet open, magnetic field on.

A plot of the rate during the day, is shown in figure 5.18; no significant fluctuation from a main value can be noted, indicating that the rate was rather stable.

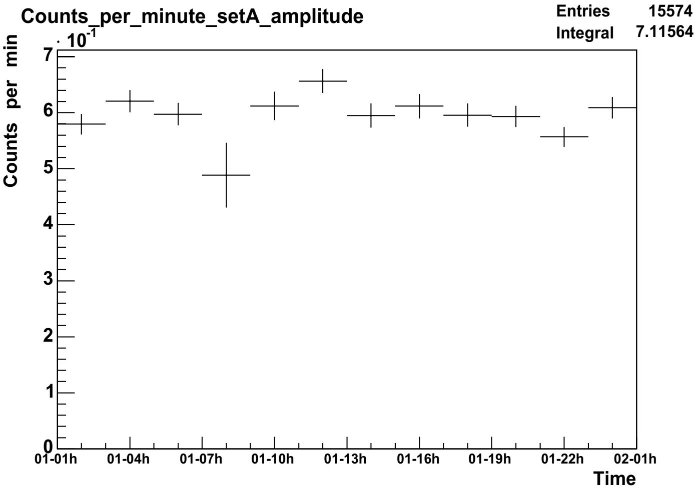

Figure 5.18: The rate (in counts per minute) as a function of time during one day. The energy interval used is between 1 and 8.5 keV as estimated from the FADC. No diversion from a mean value can be seen. The bin with the lowest value has the least exposure time, translated in bigger error bars.

Then the possibility of a position dependence was checked, by plotting in figure 5.19 the rate variation of the background in every position of the magnet, and the exposure time in each cell, for setA (the higher background times). Taking into account the time exposure in every cell, no pattern appears, the rate shows no significant change with the position. The projection of every vertical movement bin (2 degrees of vertical movement) on the azimuthal movement is plotted in the top part of figure 5.20, and similarly for every 10 degrees of azimuthal movement, the rate is projected to the vertical movement (bottom part of figure 5.20). Any possible change on the rate seems random, and within the error bars: in one of the histograms of the latter plot there is a change of the order of 10%, with an error bar of 9%.

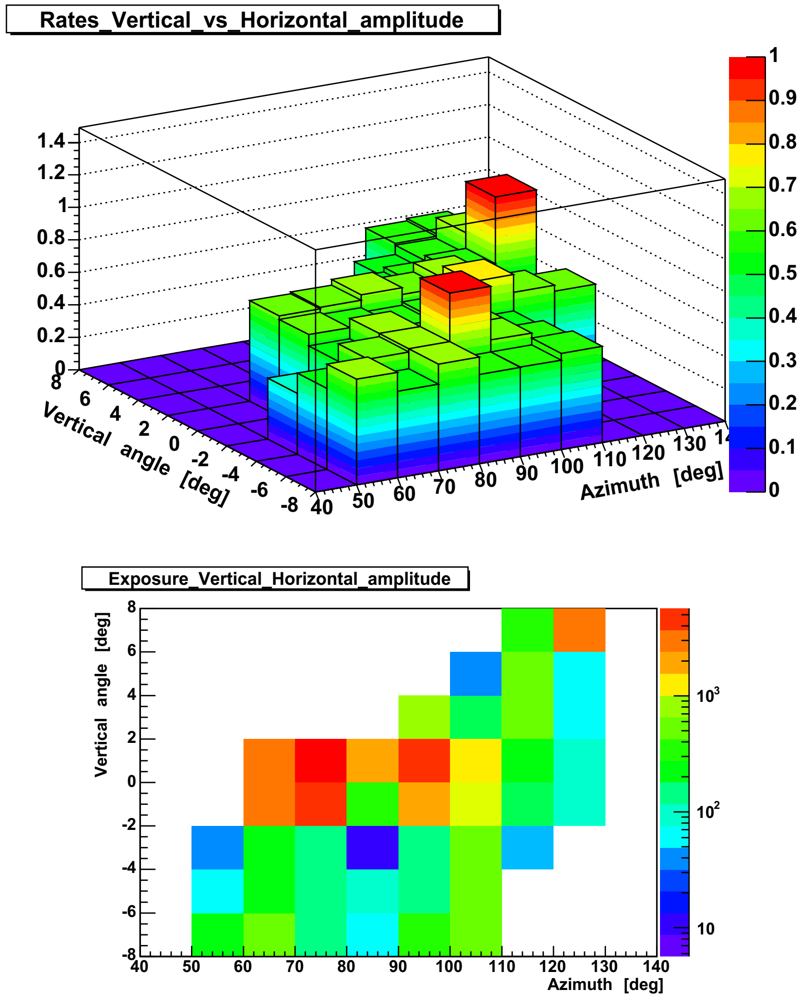

Figure 5.19: Top: the rate (in counts per minute) of the background for setA in every position cell. There seems no tendency for higher rate in some positions, taken into account the exposure time per cell. Bottom: the exposure time per position while the magnet was taking background data for setA.

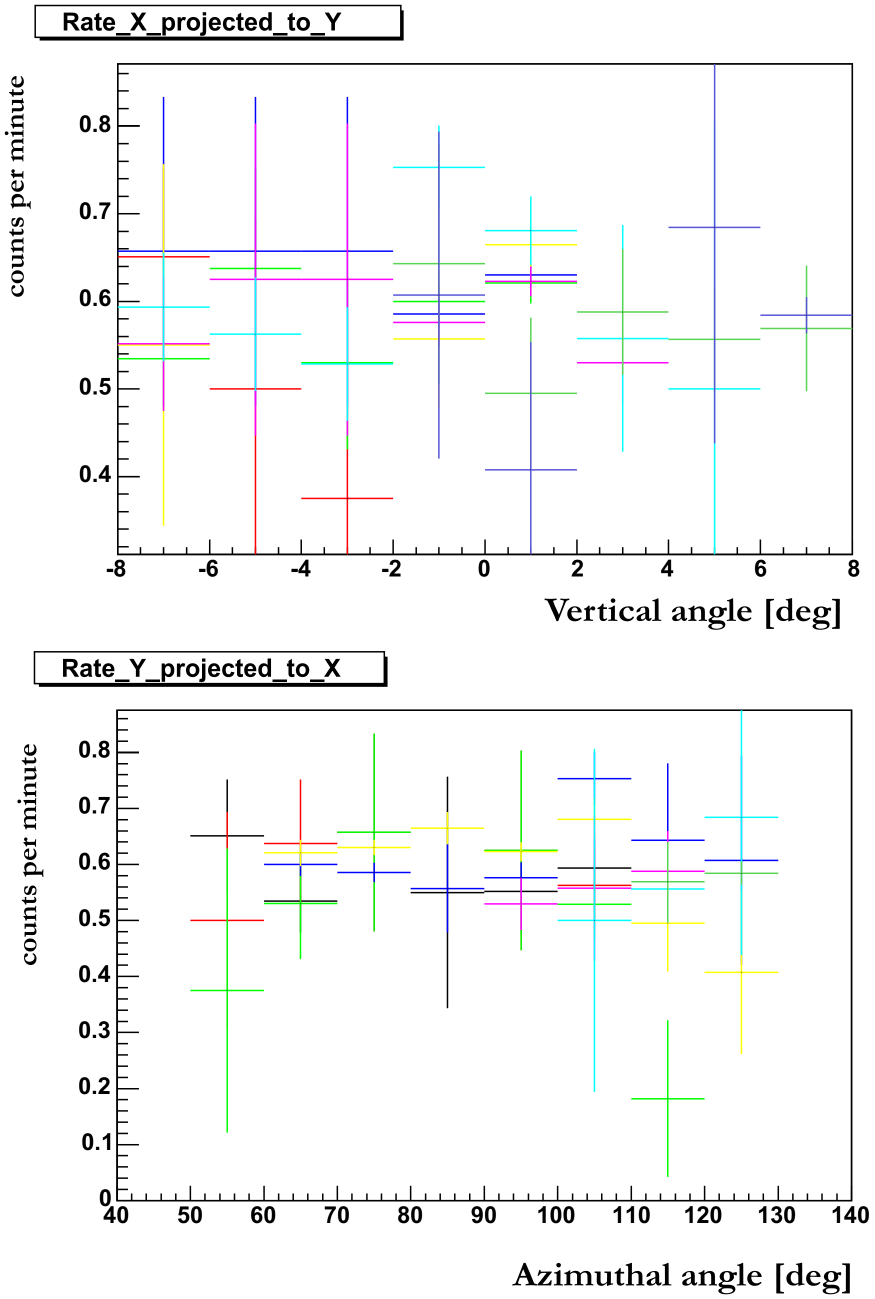

Figure 5.20: Rates versus position for setA. Top: the rates in every slice of horizontal positions projected to the vertical. Bottom: the rates in every slice of vertical positions projected to the horizontal. No dependence can be established snce any change is within the error bars.

5.3 The Results of the 2003 analysis

If axions have been detected, the data taken when the magnet is aligned with the Sun would have a distribution similar to the one shown in figure 3.2, over the background spectrum. Subtracting the background, one would be left with the axion (photon) spectrum detected. Because the efficiency of the detector is not 100% and, even more, follows a non-uniform distribution, in order to acquire the real theoretically expected spectrum for the specific detector (and software efficiency for each data set), the two spectra from figures 3.2, 5.16[4] have to be folded . The theoretically expected spectrum was calculated for a fixed m_a, using equations (3.5)[5] and (3.7), and is proportional to $g^4_{a\gamma}$ (equation (3.14)). If no signal is detected, this subtracted spectrum should be compatible with zero within its statistical fluctuations. The energy range of SetA was just at 8 keV, so the evaluation was applied to the energy range between 1 and 8 keV, for all the three sets.

It should be mentioned that throughout the data taking of the sets analyzed, the magnet was kept in a field of 9 T.

The statistical evaluation of the data follows three (plus one) steps:

i The "null-hypothesis" test

ii Best-fit

iii Confidence Interval extraction

iv Combination of the results of the 3 sets.

The "null-hypothesis" test

The spectra in figure 5.21 do not show any significant excess of the tracking over the background. To verify this, the 'null-hypothesis' test was performed: the subtracted spectra were compared to absence of signal, namely a signal expected for a coupling $g_{a\gamma} = 0$.

The weighted sum of squared deviations was calculated

$$S = \sum_{i=1}^{n} \left(\frac{y_i^{\text{exp}} - 0}{\sigma_i} \right)^2 \tag{5.1}$$

where y_i^{exp} are the experimental points, and the theoretically expected points, in this case that the coupling constant $g_{a\gamma} = 0$ are zero. Because the experimentally observed number of events y_i^{exp} in each bin are gaussian distributed, S is distributed as a χ^2.

The numbers listed in Table 5.7 confirms the hypothesis, showing compatibility of the data with absence of signal.

---

[4] Taking into account the software efficiency as given in Table 5.5.

[5] The flux equation that was actually used was the one given in [56] but changed to one suggested in [98] , with a modified normalization constant to match the total axion mass, as predicted by a more recent solar model [59].

Table 5.7: The results of the evaluation of the data for each Set.

	χ^2_{null}/d.o.f.	χ^2_{min}/d.o.f.	$\left(g_{\alpha\gamma}^{\mathrm{bestfit}^4} \pm \sigma\right)$	$g_{\alpha\gamma}(95\%)$
Set A	12.5/14	12.4/13	$-(1.5 \pm 4.5) \times 10^{-40}\,\mathrm{GeV}^{-4}$	$1.67 \times 10^{-10}\,\mathrm{GeV}^{-1}$
Set B	6.2/14	6.1/13	$(2.59 \pm 8.8) \times 10^{-40}\,\mathrm{GeV}^{-4}$	$2.09 \times 10^{-10}\,\mathrm{GeV}^{-1}$
Set C	12.8/14	10.7/13	$-(9.4 \pm 6.5) \times 10^{-40}\,\mathrm{GeV}^{-4}$	$1.67 \times 10^{-10}\,\mathrm{GeV}^{-1}$

Best fit and errors

At this step, S is calculated for every value of the parameter $g_{a\gamma}$:

$$S = \sum_{i=1}^{n} \left(\frac{y_i^{\mathrm{exp}} - y_i^{\mathrm{th}}(g_{a\gamma})}{\sigma_i} \right)^2 \tag{5.2}$$

where y_i^{exp} the experimental points, $y_i^{\mathrm{th}}(g_{a\gamma})$ the theoretically expected points. The minimum of this distribution gives the best estimate of the parameter $g_{a\gamma}$, and the error of the estimation. In figure 5.21 the best fit is shown with the dotted lines, and its value is shown in Table 5.7. Within its errors, the best fit does agree with the null-hypothesis.

Confidence Interval Extraction

The compatibility of the data sets with the absence of any signal allows the derivation of an upper limit for $g^4_{a\gamma}$. The distribution of χ^2 is plotted versus $g^4_{a\gamma}$, and the Bayesian probability distribution (assuming a flat prior in $g^4_{a\gamma}$) given by

$$P(g^4_{a\gamma})d(g^4_{a\gamma}) = \frac{1}{\sigma\sqrt{2\pi}} e^{-\chi^2(g_{a\gamma})/2} d(g^4_{a\gamma}) \tag{5.3}$$

is plotted versus χ^2. A search is performed for the minimum value of χ^2, and the ratio over the degrees of freedom (d.o.f.) are given in Table 5.7. For this data, the minimum of S lies in the region of negative values of $g^4_{a\gamma}$, which are unphysical. The 95% confidence level upper limit can be determined at the value of $g^4_{a\gamma}$ for which

$$A_1/A_0 = 0.95 \ \ ,$$

where A_1 is the area under the probability distribution within the physical region up to the upper limit, and A_0 the corresponding area within the whole physical region.

The excluded values for each set are given in Table 5.7 [99].

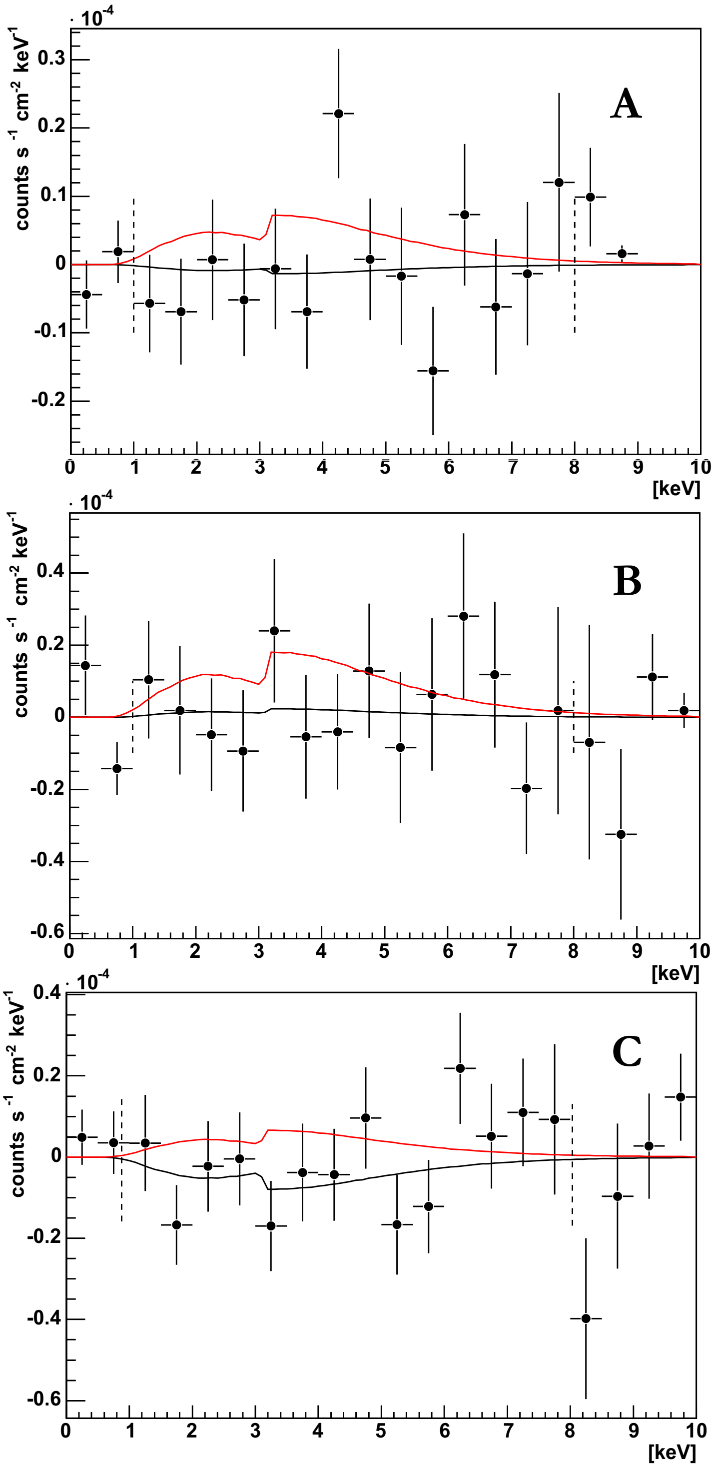

Figure 5.21: The subtracted spectra of the Micromegas data sets. The two dashed lines indicate the energy region used for the estimation, as explained in the text. The lower (black) line gives the best fit $g_{a\gamma}$, while the upper line (red) shows the $g_{a\gamma}$ upper limit with a 95% C.L.

Combination for the three sets

The distributions being gaussian, one can combine the three results for $g_{a\gamma}^4$ by multiplying the Bayesian probability functions. The next step is to repeat the previously described step and derive a combined limit for the Micromegas detector,

$$g_{a\gamma} < 1.50 \times 10^{-10}\,\mathrm{GeV}^{-1}\ 95\%\mathrm{C.L.}$$

(figure 5.22).

CAST 2003

The combined result for the three sets of the Micromegas detector is further combined with the contribution of the other two detectors in CAST. By doing so, the CAST experiment has given an upper limit of the coupling constant of axions with a mass up to 0.02 eV to photons of

$$g_{a\gamma} < 1.16 \times 10^{-10}\,\mathrm{GeV}^{-1} \quad .$$

The improvement this result has brought, compared with previous results, is shown in figure 5.22.

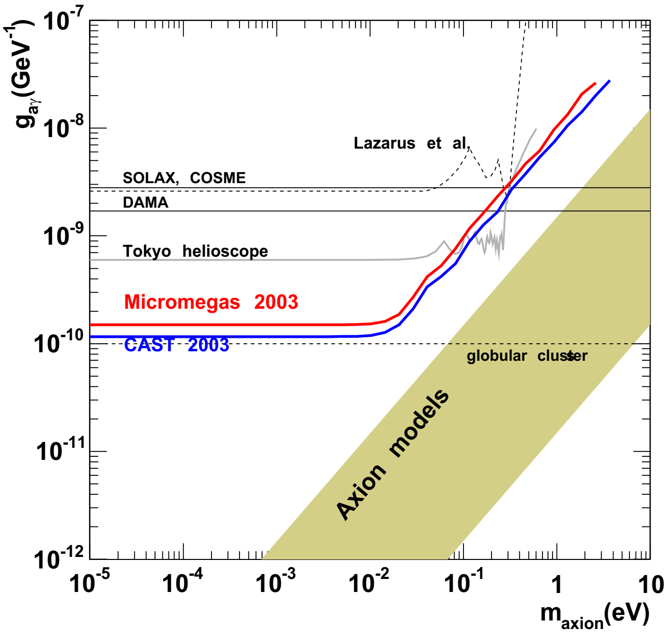

Figure 5.22: Exclusion limit at 95% C.L. from the Micromegas data of 2003, and the combined result of all the detectors of CAST for 2003, compared with other contributions. This limit is comparable to the limit from stellar energy-loss arguments and considerably more restrictive than any previous experiment. The shaded area represents typical theoretical models.

Chapter 6

The 2004 Data

The study of the 2004 data and a preliminary result is presented in this chapter. The improvement on all aspects of the experiment and Micromegas more specifically resulted in gathering three times the statistics of the first year and in an improvement of the background rejection. The detector was more sensitive to environmental changes, as the study of systematic effects showed.

6.1 The 2004 Data Taking

The end of data taking for 2003 was followed by a period of maintenance, during which several things were improved in the whole setup of the experiment. For the Micromegas detector, the change was radical; the detector V3, operating during 2003, was substituted by a new one, V4. The reasons justifying this change were mainly the forementioned "cross-talk" of the strips and the fact that the detector V4 had negligible amount of dead strips, without any signs of the "cross-talk" problem.

V4 was slightly different from V3 in terms of construction characteristics as well; Table 6.1 shows a comparison of the two.

Table 6.1: Comparison between the Micromegas detectors V3 (used in 2003) and V4 (used in 2004).

Characteristics	V3	V4
Conversion Gap	25 mm	30 mm
Amplification Gap	50 μm	100 μm
Pillars on:	mesh	readout plane

At that time, the copper case acting as a Faraday cage was changed to a new one, constructed in Freiburg. Other changes included the calibration performance and the data-taking protocol:

- The movement of the calibration source to the corresponding window from the shielded parking position was performed by a stepping motor, fully controllable via ECL signals. These signals are provided by an input/output register VME module, which is controlled by the acquisition software.
- It was decided to no longer store tracking data in a separate from the background file. The decision was taken with a view of a more automated system, that would demand less interference with the shifters. The Slow Control data as well as the tracking program's logfiles were used to select the tracking events from the background.
- A veto counter (with dimensions 22 cm × 30 cm × 2 cm) was implemented on the top part of the detector.

Table 6.2: The hours of data taken by the Micromegas detector in 2004.

	Dates	Background hours	tracking hours
Commissioning data	01.05 - 31.05		
Set A	01.06 - 15.11	2404.2	178

Approximately 3400 h of background data and around 200 h of tracking data was the harvest of 2004. Out of these, for the evaluation were used 2404 h of the background and 178 h of tracking the Sun. This reduction comes mainly from keeping the same conditions of tracking and background (magnetic field on, valve to the magnet open) and that the data after May were of higher quality than the ones takes in May.

Table 6.3: The expressions of the new Conditions for the 2004 data.

	Equation expression
Condition 1	mean value : 84.5 ns
and	σ : 2 ns
Condition 2	$\mathrm{Multiplicity_y} > \mathrm{Multiplicity_x} - 4$
and	$\mathrm{Multiplicity_y} < \mathrm{Multiplicity_x} + 5$
Condition 3	$\mathrm{Energy} > 3/3.2 \times \mathrm{Scharge} - 2.4/3.2$
and	$\mathrm{Energy} < 8.8/8 \times \mathrm{Scharge} + 1.2$
Condition 4	$\mathrm{Multiplicity_y} + \mathrm{Multiplicity_x} < 10/6 \times \mathrm{Energy} + 25$
Condition 5	$\mathrm{Energy_x}/\mathrm{Energy_y} > 0.4$
and	$\mathrm{Energy_x}/\mathrm{Energy_y} < 1.5$

6.2 The Analysis of the 2004 data

6.2.1 Conditions and Efficiency

The new detector showed no "cross-talk" of the strips, therefore the strips' information could be exploited much better than the year 2003. Therefore the optimization of the conditions was redone, resulting in the following set (Table 6.3):

1. As for 2003, the risetime is used to define a rejection criterium: events outside a region denoted by 3σ around a mean value are excluded.

2. Another condition used the same way as in 2003, is the two-dimensional plot of the multiplicity in X versus the multiplicity in Y.

3. The third condition used in 2003 was slightly changed: the amplitude of the mesh pulse (in keV) versus the energy deposited on the strips (in keV) gave the new condition.

4. The sum of the multiplicities of the two directions, X and Y, is plotted versus the energy of the pulse. Figure 6.1 shows that the X-ray events can be constrained by a slope that will allow higher multiplicities for higher energies.

5. The ratio of the energies deposited per plane of strips, is not expected to be very different than unity. The bulk of the population is sitting in a zone around one, as can be seen in figure 6.2.

6. The implementation of the veto counter, although not placed in the optimum position, can help reject the events that come in coincidence with the detector. When taking a look at the time interval of the events recorded in the detector, there is

a small window between 0 and 10 μs that can be excluded (figure 6.3) as events in coincidence with the veto.

The calculation of the efficiency was done following the same way as for the 2003 data, only now keeping in mind that the reference of energy is given by the strips. Hence, the efficiency of these cuts reached 90% for both the 3 keV and the 5.9 keV peaks (with a statistical error of less than 1%).

The detector used in 2004, V4, has a bigger conversion gap, which increases the efficiency of the detector another 4% approximately, as figure 6.4 shows.

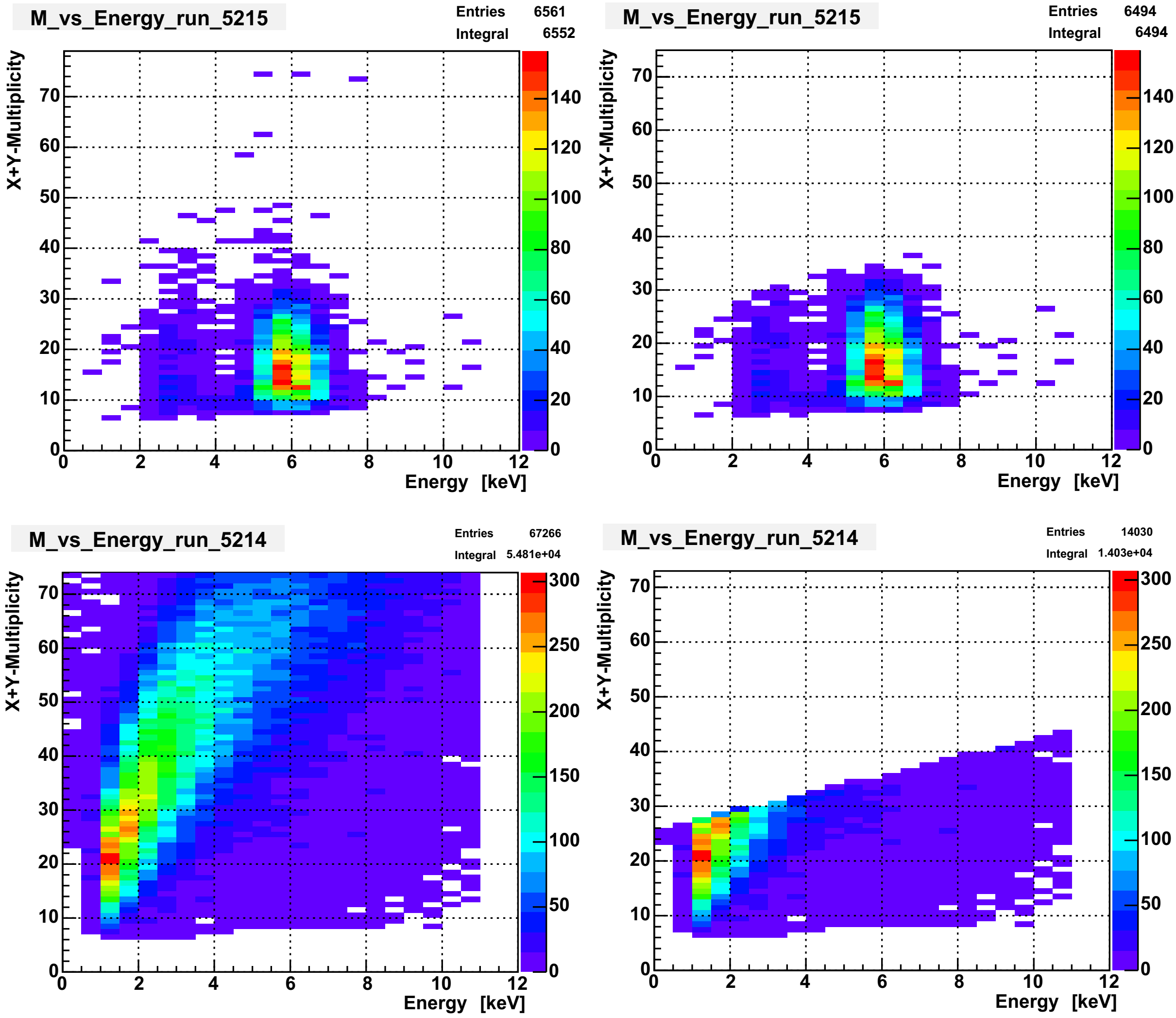

Figure 6.1: The sum of the total multiplicity in the X and Y directions is plotted versus energy extracted from the FADC. At the top part the image of a calibration run with an ^{55}Fe source before (left) and after (right) the condition. The lower shows the equivalent plots for a background file.

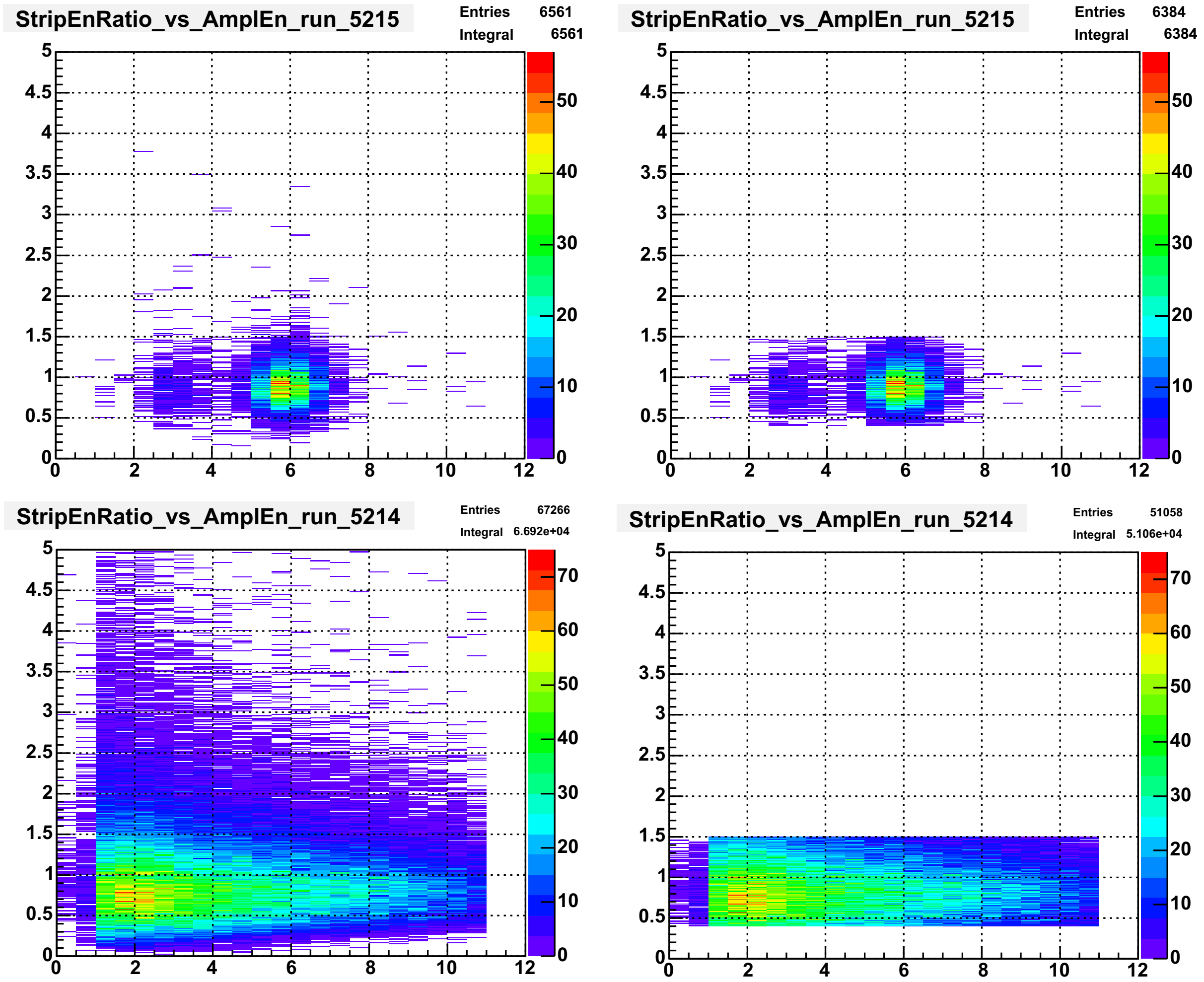

Figure 6.2: The plot of the ratio energy deposited in X over energy deposited in Y strips, versus energy extracted from the FADC. The top part shows that the X-ray events of the ^{55}Fe source are gathered in a zone around 1 (on the left before and on the right after the application of the condition). The effect of the condition on a background file is shown below.

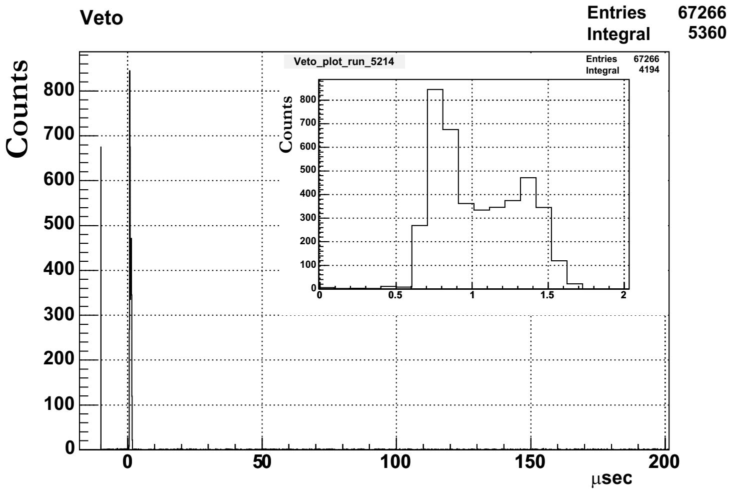

Figure 6.3: The events plotted versus the time since the last veto trigger. The peak at zero represents events in coincidence with the veto (the zoomed plot on the top right corner) and therefore should be rejected. This plot gives a nice visualization of the drift time in the detector.

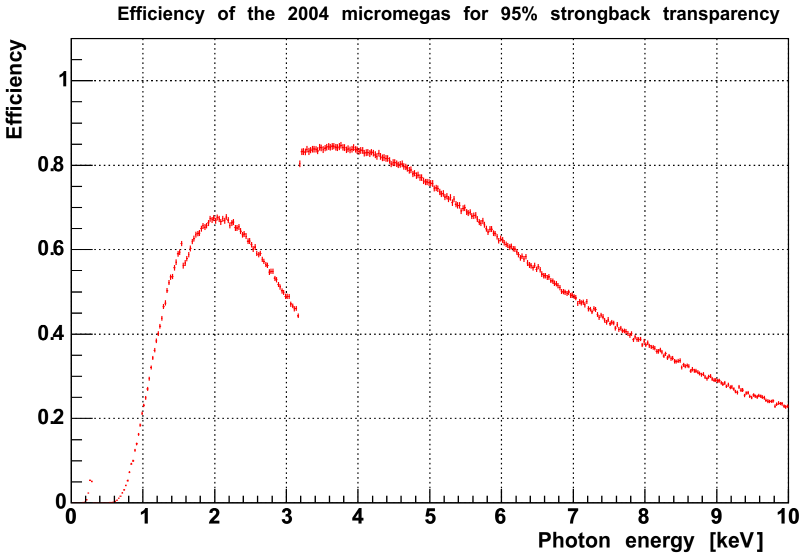

Figure 6.4: The curve of the hardware efficiency of the detector V4 used in CAST during 2004 data taking.

6.2.2 Spectra

The energy spectrum after the selection of the criteria described in the previous section is shown in figures 6.5 and 6.6 for the energy extracted from the FADC and from the strips respectively, for tracking and background data. The shape of the spectra resembles very much the 2003 one, as expected. The level, though, for the region until 7 keV is reduced approximately by a factor 2 with respect to the 2003 data, which is explained by the elimination of the cross-talk. Another observation is that the copper peak, around 8 keV is less prominent, explained by the fact that there is less copper in the detector. One can also note that there are some bins for energies higher than 4 keV where the tracking shows an excess over the background of the order of 2 sigma, more evident in the spectrum obtained from the mesh pulse. In order to try to understand this effect, a close study of the systematics was performed.

6.3 Study of the Systematics

It was already mentioned that the very first attempt to analyze the data, revealed a clear excess of the tracking over the background in certain bins, more clear in the mesh signal than in the strips (figures 6.5, 6.6). Several dependencies were looked at, in order to understand this effect, starting with the dependence on day time.

Time dependence

Plotting the rate (in counts per minute) during the whole day, showed a big daily variation up to $\sim 15\%$, figure 6.7, which peaks exactly at the time bins when the tracking data is accumulated. It should be stressed that the strips and the mesh pulse show the same tendency. This link between the time variation and the level of the energy spectra was verified when dividing the background spectrum in two time periods, one between midnight until noon (00-12) and the second the rest (12-24), as figure 6.8, or even more eloquently in 6-hour intervals (figure 6.9). The effect is very similar when plotting the equivalent spectra for the strips. The study of several systematics followed as it will be described.

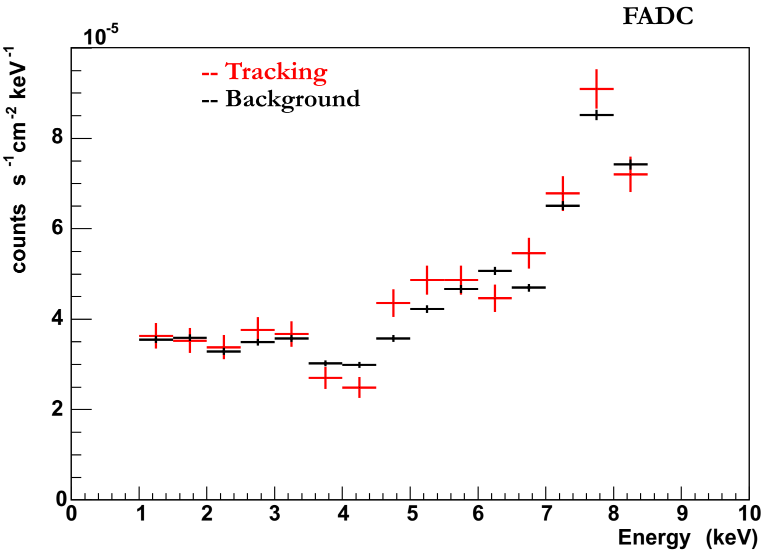

Figure 6.5: The energy spectrum of the background data (black line) overlaid with the tracking data (red line), using the amplitude of the mesh pulse translated into energy. There are some bins where the excess of the tracking data exceeds the 2σ.

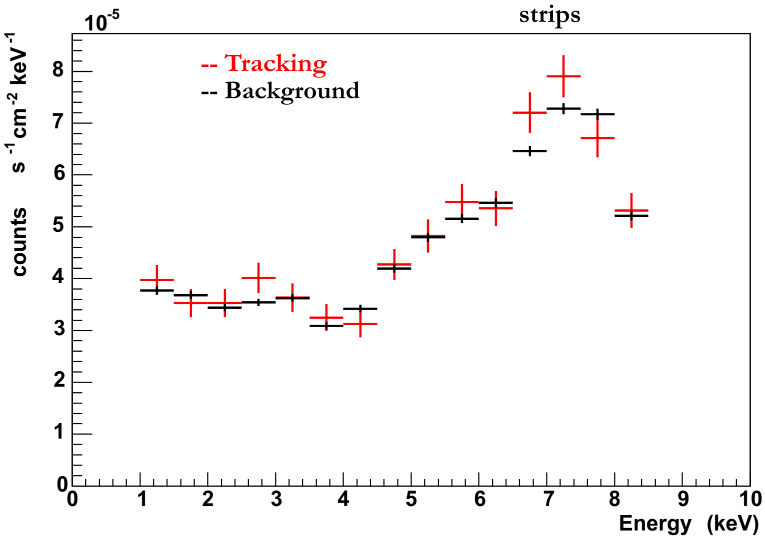

Figure 6.6: The energy spectrum of the background data (black line) overlaid with the tracking data (red line), using the energy of the strips. Although the excess is still apparent, the worse energy resolution of the strips in comparison to the mesh signal smoothes away the difference. .

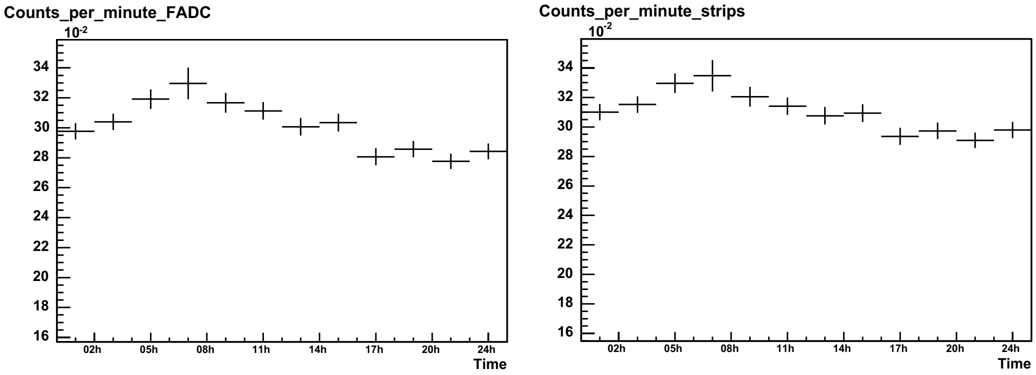

Figure 6.7: The rate (in counts per minute) as a function of time during one day. The energy interval used is between 1 and 8.5 keV as estimated from the pulse (left) and the strips (right). The rate changed with time, up to 15% (maximum to minimum) for both.

Gain studies

During the data taking, it was observed that the gain of the mesh was showing rather big variations from day to day (figure 6.10), which were not followed by the strips, where the variation with time was much smaller. Checking the gain per periods of two months, both for the strips and the mesh pulse, interesting observations can be made; the gain of the mesh pulse was changing randomly, not following a clear pattern for the months of June until September. The quantity of interest is the ratio of pressure P and temperature T which is proportional to the density ρ of the gas inside the detector. The last two months, there is a clear slope indicating that a change of approximately 3% in the P/T quantity, is followed by a 10% change in gain (figure 6.11, left). This is in agreement with calculations on the expected dependence of the gain on pressure and temperature. The same relation can very clearly be established for the strips through all the months (figure 6.11, right). Of course, by taking the appropriate calibration for the data of every day any such effect is corrected for, since there existed a calibration file per day. However, the calibrations were taken the same time of the day, immediately after the tracking time was over, and there was no information of any potential gain variations within the day.

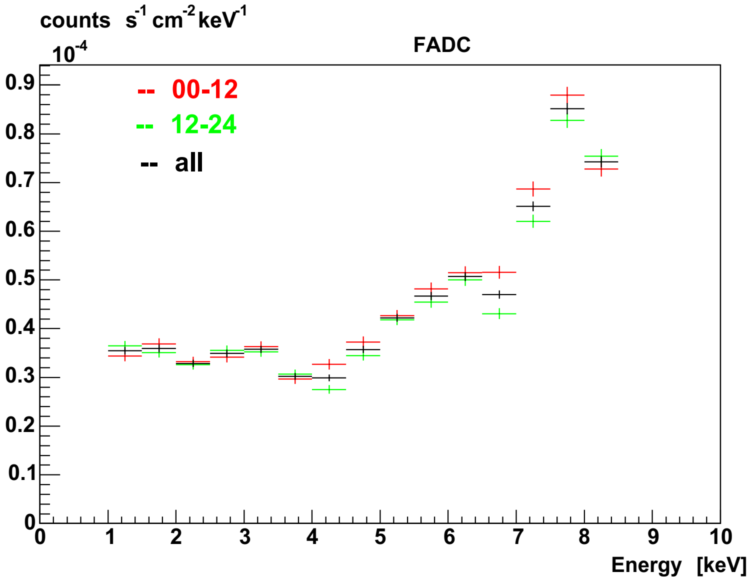

Figure 6.8: Dividing the background data in two time intervals, one between midnight and noon (red line), and the other between noon and midnight (green line). They are both compared here to the spectrum when all the background is taken into account (black line).

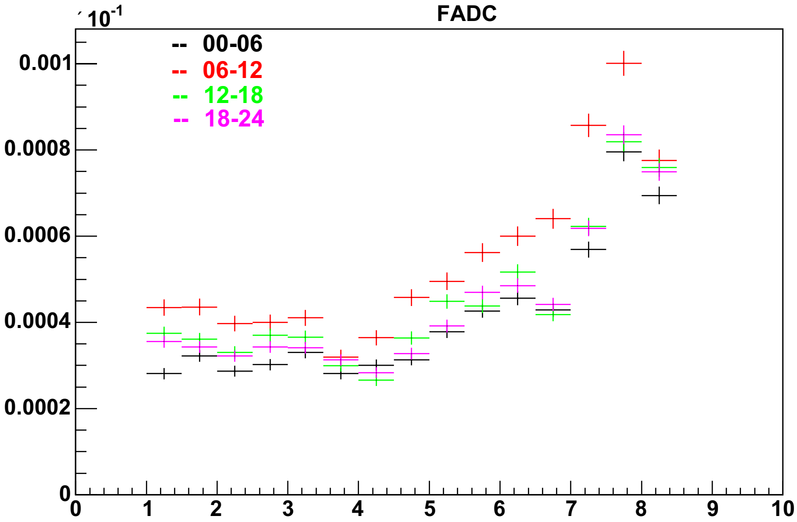

Figure 6.9: A further division of the data in 4 periods: 00-06 (black line), 06-12 (red line), 12-18 (green line) and 18-24 (purple line). The spectrum of the second interval has an excess overall the points.

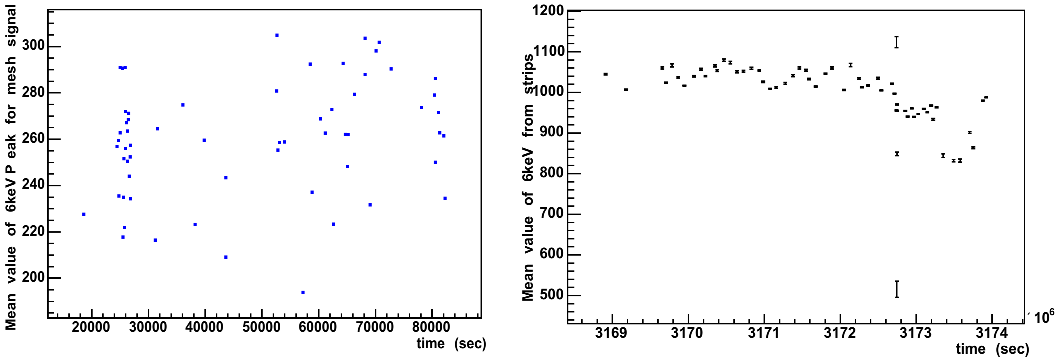

Figure 6.10: The mean value of the 6 keV peak of the calibration as taken from the pulse (left) and the strips (right) for June and July, versus time. For the FADC the change was ±16%, while for the strips is very small, of the order of ±4%.

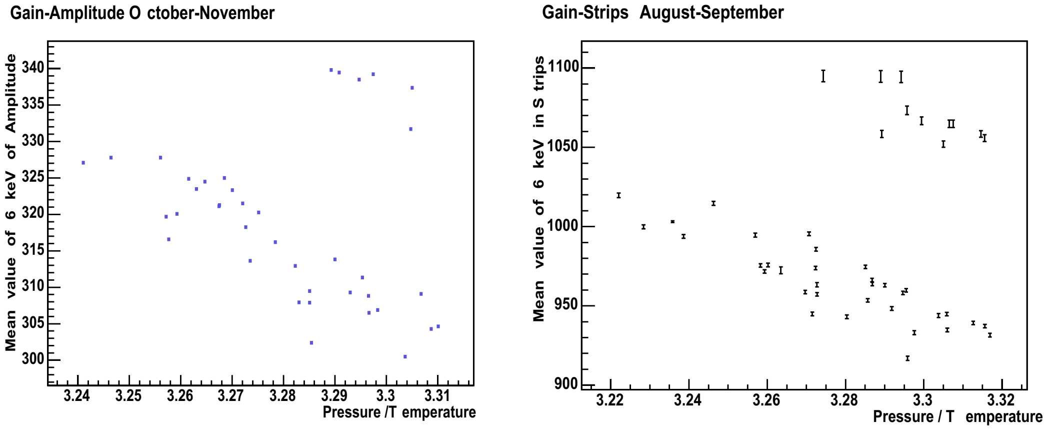

Figure 6.11: The mean value of the 6 keV peak of the calibration as taken from the pulse (left) and the strips (right), versus P/T. The plot on the left is from October-November and in the right from August-September. Both show the same dependence of the gain on P/T: a 3% change in P/T influences the gain by 10%. The small population of events that appears in the upper right corner of each plot seems to follow the same dependence. This jump on the gain is believed to be due to changes in the flux of gas through the detector.

At the end of the data taking (November), special long calibrations were taken with the purpose to study this effect. The data of the six consecutive days (7-hour long calibration files) did not show any clear correlation with the environmental conditions, which themselves did not show more than 1% of variation during those days (figures 6.12, 6.13).

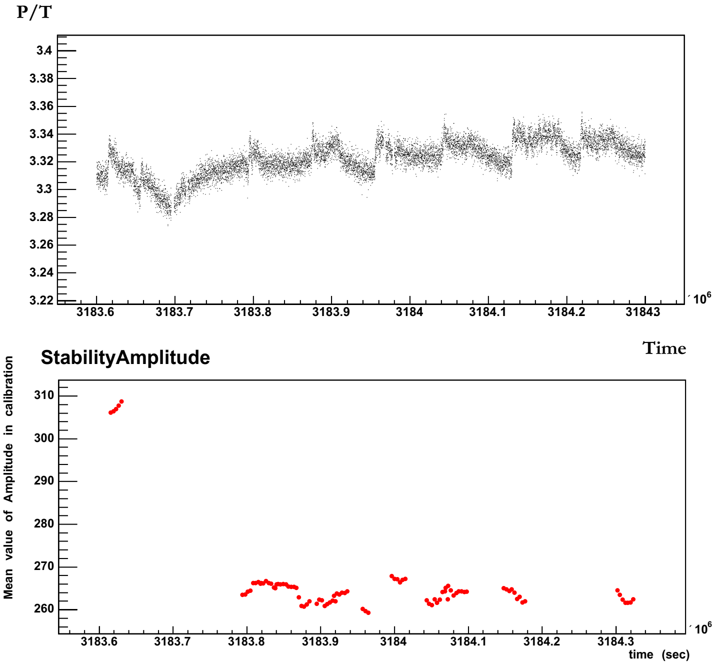

Figure 6.12: Top: the variation of P/T in November, when the long calibrations were taken. Bottom: the mean value of the 6 keV peak of the calibration every hour, taken from the mesh signal.

Figure 6.14 shows the change in rate (for the strips) and in P/T during one day, averaging for all the months. Judging from the previously mentioned curves, the change of $\sim$ 1% in P/T observed in this plot would be translated in approximately 3% in gain, which is compatible with the dependence observed in figure 6.11. This effect probably does not account for the variation of the rate, in which case an excess over all the energy range would be expected.

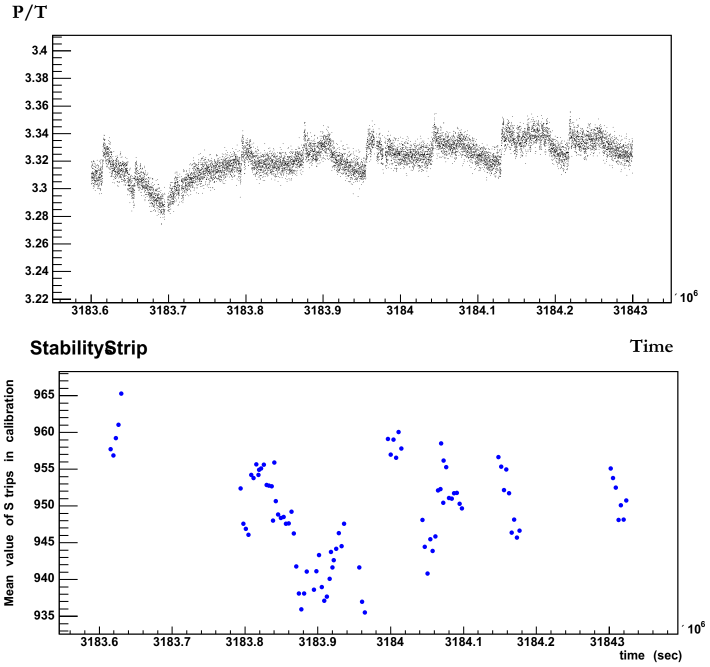

Figure 6.13: Top: the variation of P/T in November, when the long calibrations were taken. Bottom: the mean value of the 6 keV peak of the calibration every hour, taken from the strips.

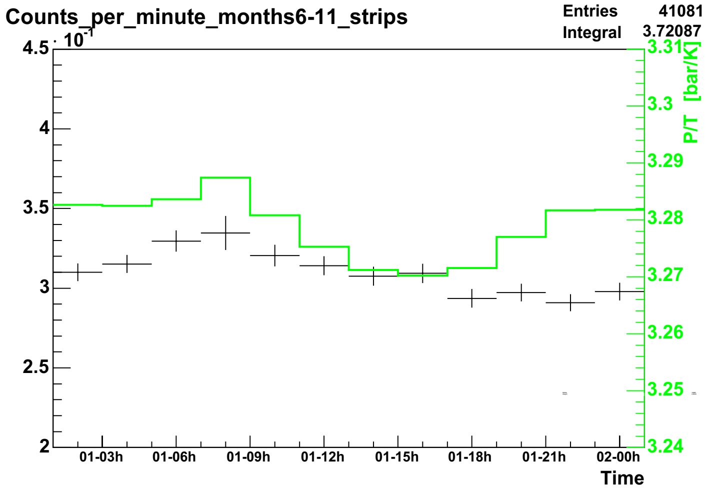

Figure 6.14: The P/T variations of all the months (green line), plotted at the same figure as the rate (crosses). A change of 0.6% in the green curve means a 2.5% change in the gain.

Position Dependence

The second step was to study any position dependence on the rate; the positions of the sunrise and sunset trackings are for more than 80% of the time very different, and although there was an attempt to take background data in the same positions as the tracking, this time was divided between the two places. Therefore there is a lot of background data taken in positions very different than the position the magnet passes by when tracking the Sun. The exposure tracking time with regard to position is shown in figure 6.15, and the same plot for the background data in figure 6.16.

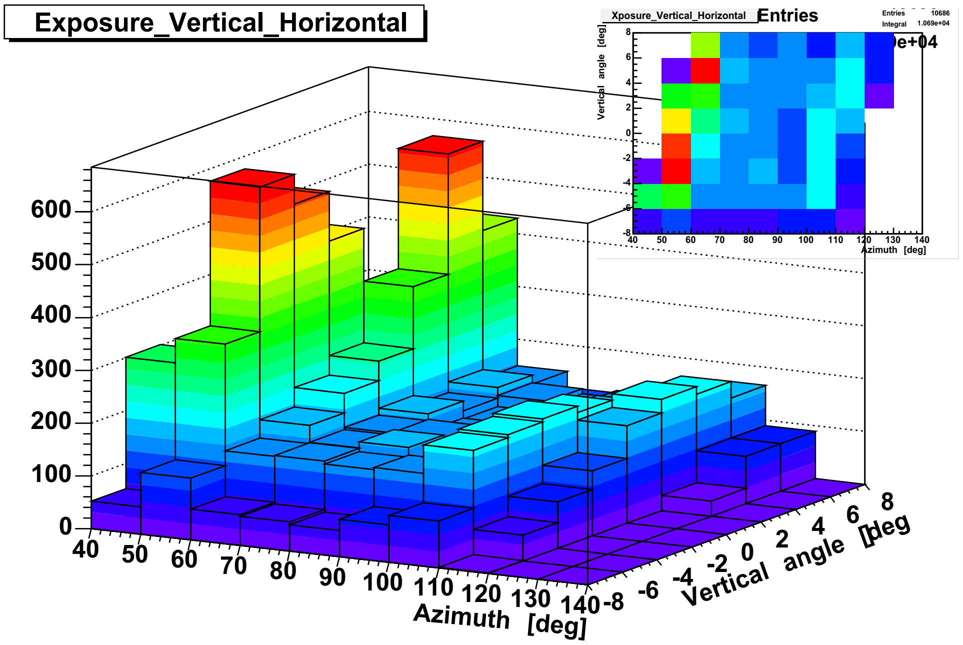

Figure 6.15: The exposure time per position while the magnet was tracking the Sun (the z axis is in min). The top right corner shows the flat version of the 2-dimensional plot.

Figure 6.17 shows the rate variation of the background in every position of the magnet, where higher rates are observed in azimuthal angles of less than 90 degrees. To see the uncertainties in each cell, the projection of every vertical movement bin (2 degrees of vertical movement) on the azimuthal movement is plotted in figure 6.18. This figure shows a decrease of the order of ±15% on the rate when the magnet is in positions of azimuth higher than 90°. The equivalent projection of the azimuthal movement bins (10 degrees of movement) on the vertical movement axis cannot provide with a clear image of any dependence.

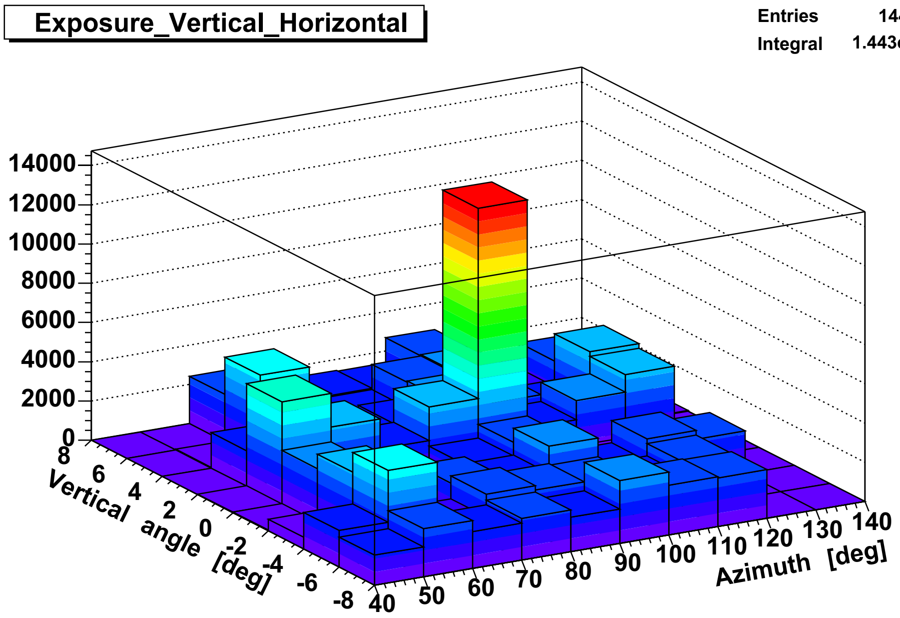

Figure 6.16: The exposure time per position while the magnet was taking background data (the z axis is in min).

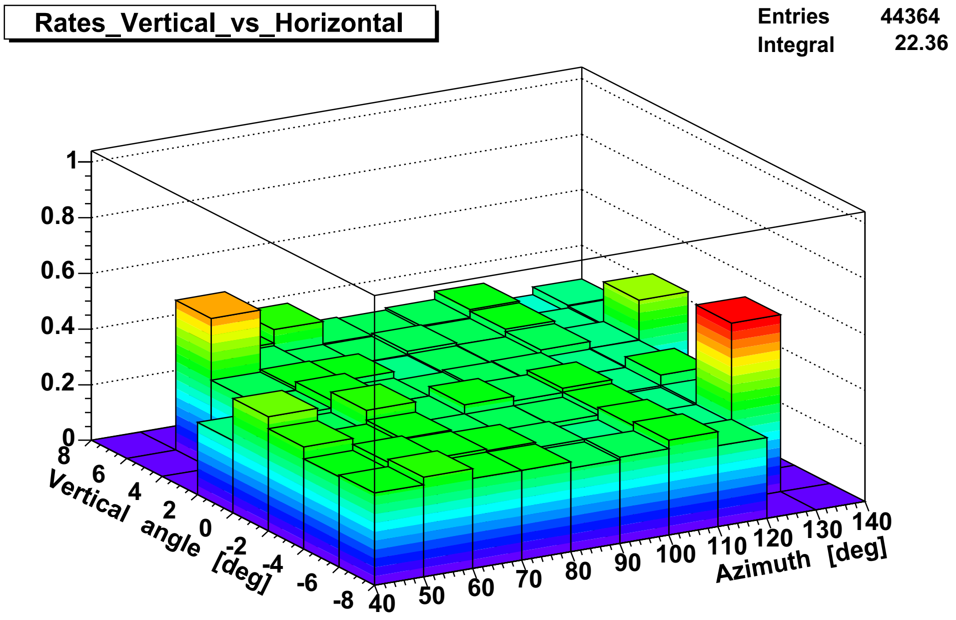

Figure 6.17: The rate (in counts per minute) of the background data in every position cell. There is a tendency for higher rates when the magnet is in positions with azimuth less than 90°.

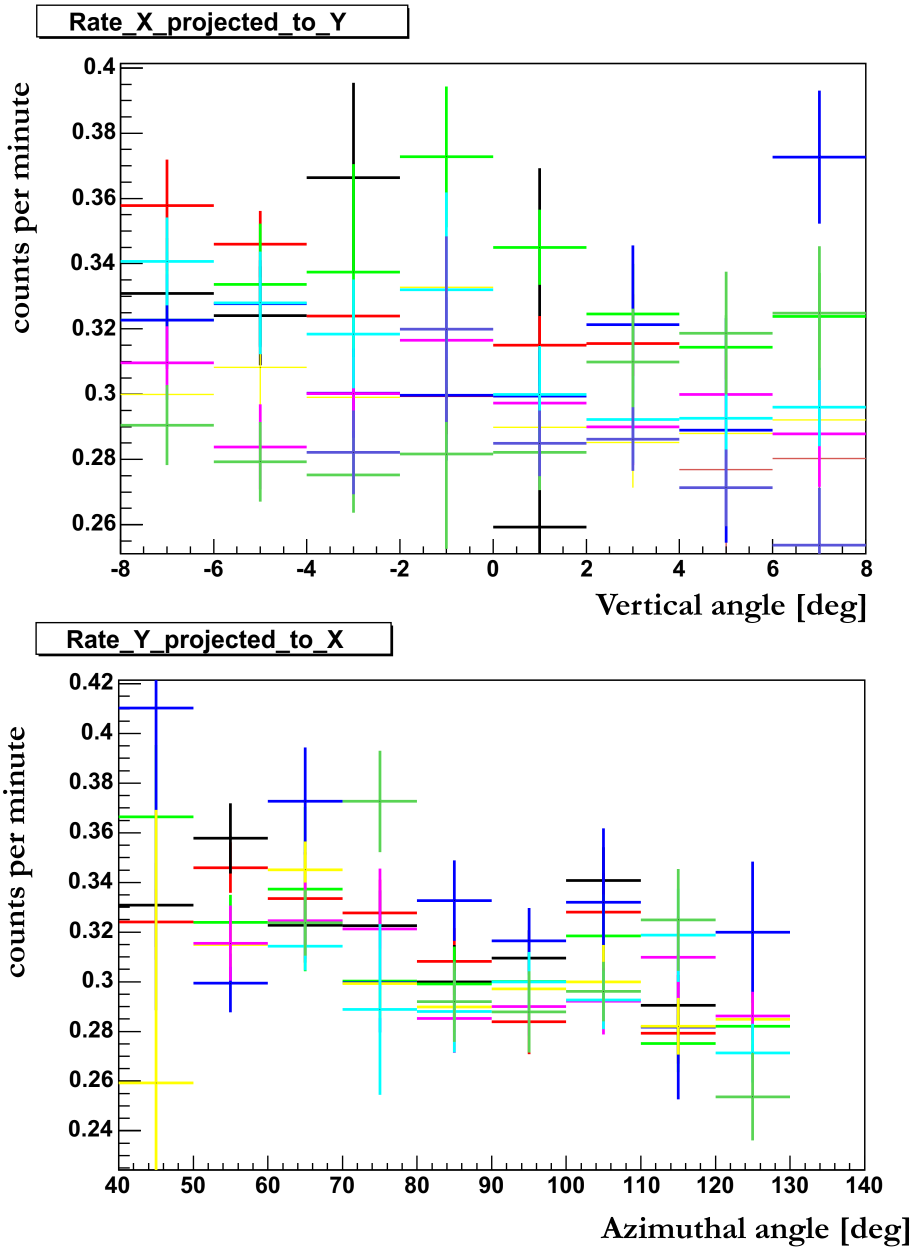

Figure 6.18: Top: the rates in every slice of horizontal positions projected to the vertical. Bottom: the rates in every slice of vertical positions projected to the horizontal, where the tendency for higher rates in positions with less than 90° azimuth is of the order of ±15% .

Position Dependence Correction

As a dependence on the position has been observed, one can try to correct for it and observe if the excess in the spectra disappears. In order to study this, the position of the magnet in the experimental hall is mapped in cells of 2 degrees of vertical movement and 10 degrees of horizontal movement[1]. The strategy is simple: the relative tracking exposure time for each position is calculated, and these numbers are used to weigh the background events.

The effect of this correction is shown in figure 6.19, where this *"effective"* background is shown in comparison with using the background data without the correction. The background points have moved upwards, towards the tracking points, and have acquired bigger error bars. These spectra will be used for the evaluation of the data.

---

[1] This technique was used for the TPC, for the 2003 data, when they were seeing a rather big variation of the rate with position.

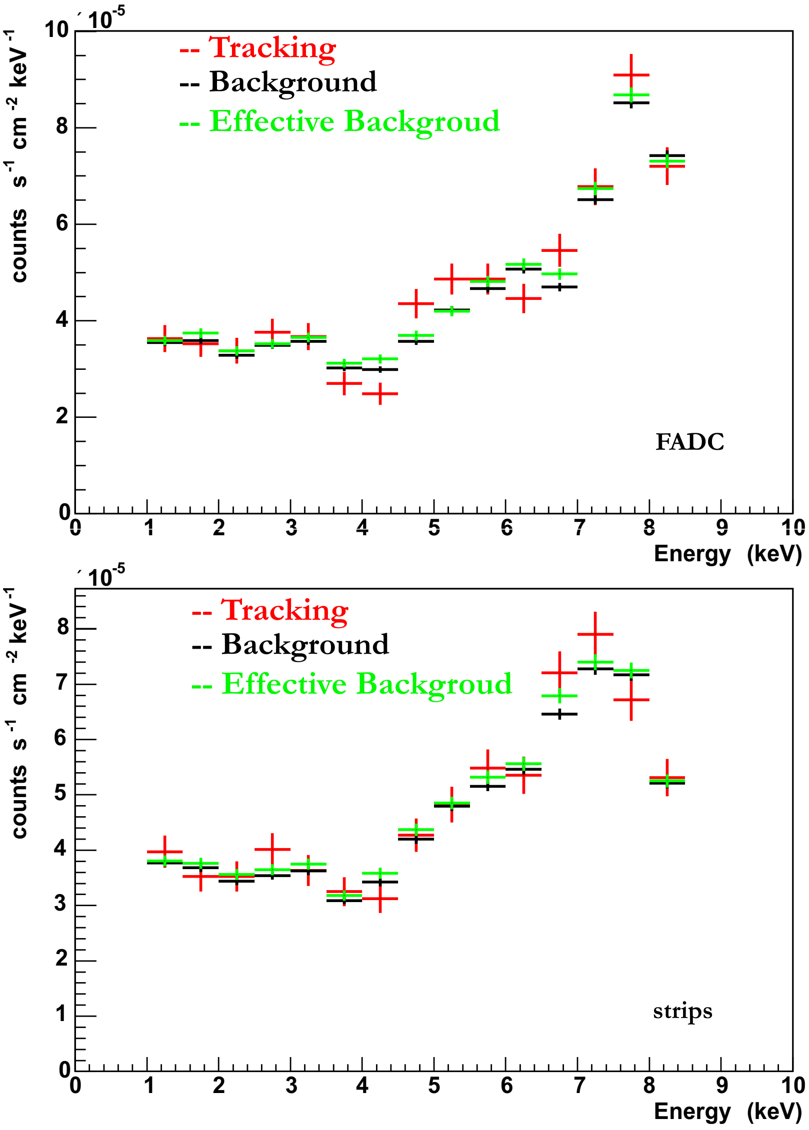

Figure 6.19: The energy spectra of the tracking (red) and background data (black) for the pulse (top) and the strips (bottom). In green is drawn the effective background, which is the background after correcting for the position.

6.3.1 Results

After this look to the data, a preliminary result can be derived. The same steps as for the evaluation of the 2003 data were used. Some parameters were changed referring to the efficiency (both hardware and software), but to the value of the magnetic field as well. For approximately 20% of the data taking time the magnetic field was at the maximum (that is 13300 A, corresponding to 9 T) and the rest at the usual value of 13000 A (8.79 T). This means an "effective" magnetic field of 8.83 T.

In Table 6.4 the results are shown: the null-hypothesis test, the best fit to the data, as well as the upper limit for the coupling constant of axions to photons (for masses up to 0.02 eV, derived from the first look at the 2004 data

$$g_{a\gamma} < 1.21 \times 10^{-10}\,\mathrm{GeV}^{-1}$$

with a 95% C.L. Figure 6.20 in turn gives he subtracted spectrum with the best fit and the upper limit curves.

This upper bound is more restrictive than the one derived from the 2003 data (figure 6.21). This can be explained by the fact that in this year there were gathered three times more statistics than in 2003 and by the two times lower background level. In figure 6.21 an attempt was made to combine the two curves (although the new result is preliminary), which gives a limit of the coupling constant $g_{a\gamma} < 1.15 \times 10^{-10}\,\mathrm{GeV}^{-1}$ with a 95%C.L.

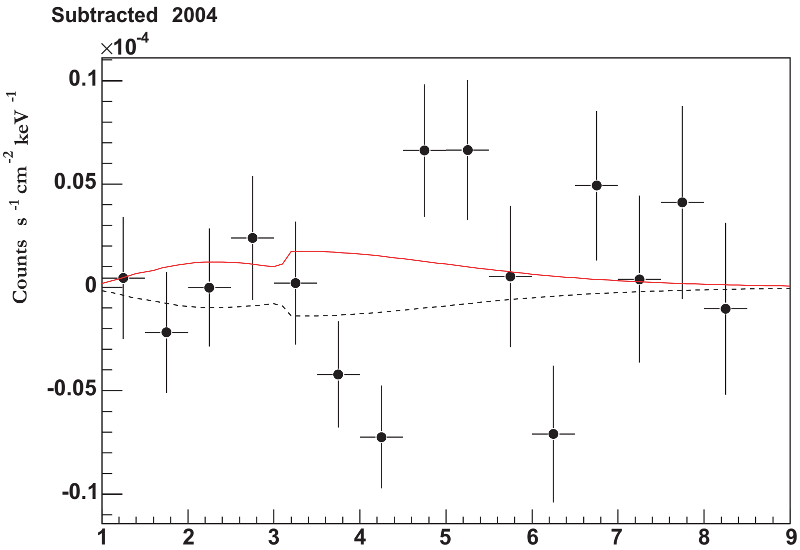

Figure 6.20: The experimental subtracted spectrum of the 2004 data for Micromegas, together with the expectation for the best fit $g_{a\gamma}$ (dashed line) and for the 95% C.L. limit on $g_{a\gamma}$ (solid red line).

Table 6.4: The value for the coupling constant for the 2004 data.

	$\chi^2_{\rm null}$/d.o.f.	$\chi^2_{\rm min}$/d.o.f.	$\left(g_{\alpha\gamma}^{\rm bestfit^4} \pm \sigma\right)$	$g_{\alpha\gamma}(95\%)$
2004 data	27.8 / 15	21.6/14	$-(1.53 \pm 1.4) \times 10^{-40} GeV^{-4}$	$1.21 \times 10^{-10} GeV^{-1}$

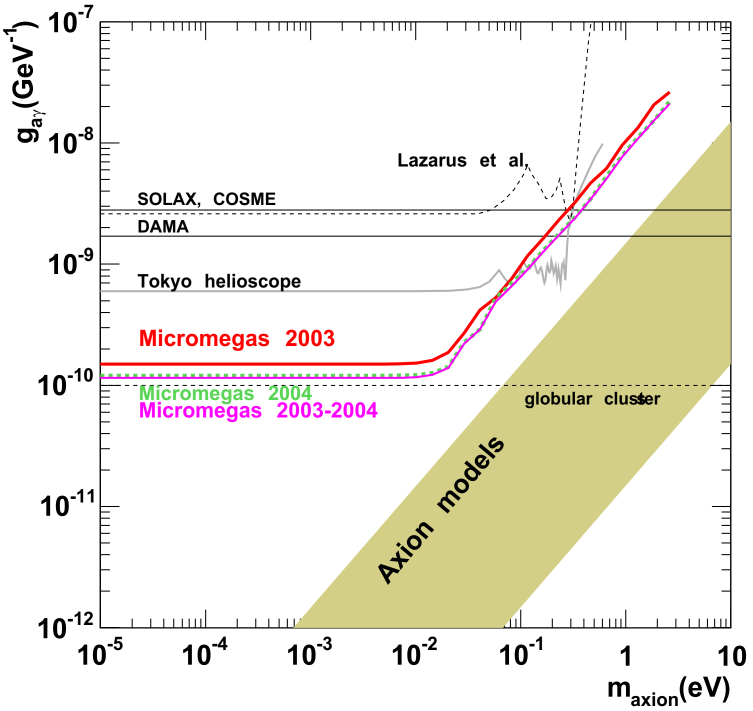

Figure 6.21: The upper limit of 2004 in the exclusion plot (dashed line), compared with the one of 2003. The bound is more strict, as expected due to lower background level and higher exposure time. An attempt to combine the data is shown as well.

Chapter 7

Conclusions and Outlook

In the present thesis a description of the CERN Axion Solar Telescope has been given, along with a detailed presentation on the commissioning, the operation and the analysis of the data taken with the Micromegas detector within the two years of data taking for the first phase of the experiment.

A dedicated Micromegas detector was built in low radioactive materials in order to fulfill the requirements for a low background detector. For the first time a two readout plane was implemented, resulting in an excellent spatial resolution. The spatial resolution together with the very good energy resolution allows to distinguish events issued from X-rays from background events taken into account their energy, topology and time structure, reaching a very low level of background.

The CERN Axion Solar Telescope operated for about 6 months, from May to November, in 2003. Because of the various interventions in order to improve the system, the data were grouped in three sets, summing up to approximately 750 h of background data and 75 h of data while the magnet was tracking the Sun.

No signal above background was observed. The absence of signal was verified for each set with the null hypothesis test, and with the obtained values of the coupling constant $g_{a\gamma}$ that fit best the data. This absence of signal allows the extraction of an upper limit for the coupling of axions to photons. The limit was calculated for every set, and the results were combined into

$$g_{a\gamma} < 1.50 \times 10^{-10}\,\mathrm{GeV}^{-1}$$

for axion masses up to 0.02 eV.

The combination of the Micromegas result with the results of the other two detectors of the experiment, has given the exclusion limit for CAST 2003

$$g_{a\gamma} < 1.16 \times 10^{-10}\,\mathrm{GeV}^{-1}$$

for $m_a \leq 0.02\,\mathrm{eV}$. This limit is five times more restrictive than previous experiments.

CAST concluded the first phase of data taking in November 2004. A description of the data taking of this second year has been reported as well. A first, preliminary, result from the 2004 data has been given,

$$g_{a\gamma} < 1.21 \times 10^{-10}\,\mathrm{GeV}^{-1}$$

showing an improvement in the sensitivity for the same range of masses.

The upper limit on the axion mass of the sensitivity, 0.02 eV, is imposed because of the so-called 'coherence' issue: for a given path length, approximately 10 m in the case of the CAST experiment, the axion-photon oscillation is constructive, meaning that the transition rate of axions to photons is maximum, only up to this mass. That is why CAST has planned a second phase for the experiment.

During this phase gas will be inserted in the magnet pipes, making the experiment extend its sensitivity to higher masses (figure 7.1, looking for the first time in the "axion window", masses up to 1 eV. Similarly to the microwave cavity searches, the gas density will be varied in order to tune the magnet to different axion masses. CAST Phase II has been approved by CERN for running late 2005 until 2007, and the required mechanical interventions, cold window tests and the construction of a helium gas system are underway.

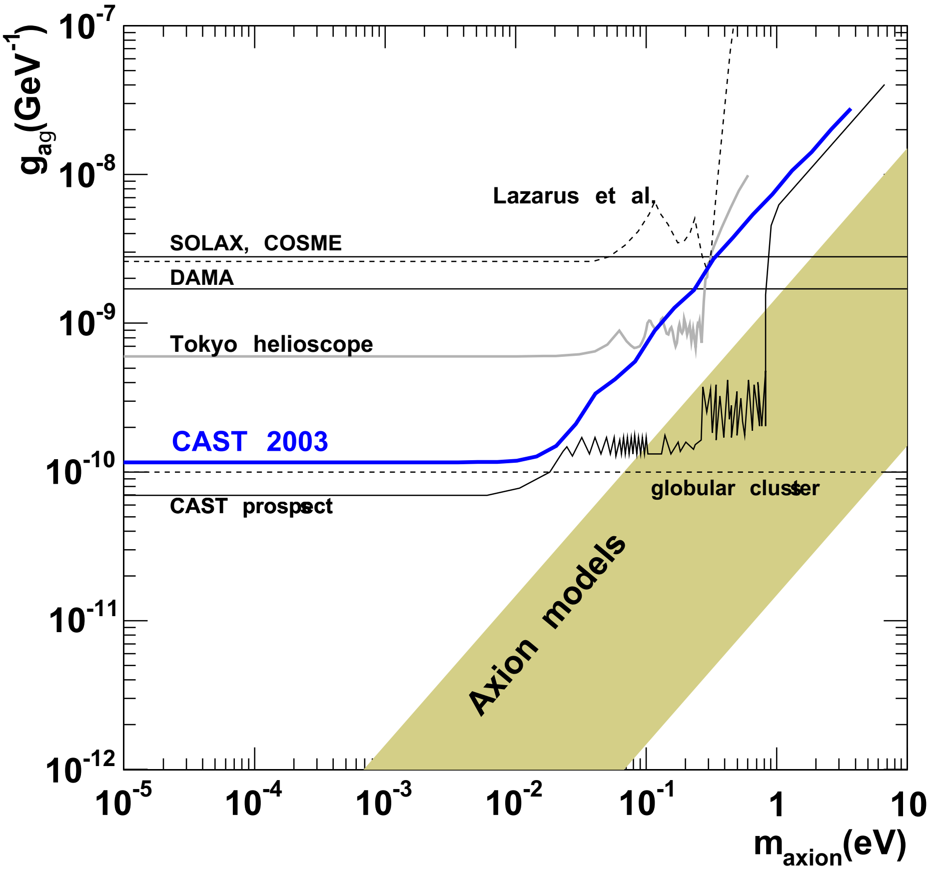

Figure 7.1: The exclusion plot of the coupling constant of axions to photons versus axion mass. The exclusion limit (at 95% C.L.) of CAST from the 2003 data is stronger than other constraints. The shaded band represents the theoretical models. The future CAST sensitivity as foreseen after the conclusion of Phase II, which will go into that band, is also shown.

A further improvement is sought for the experiment through the implementation of more X-ray focusing devices. Such an addition, for example for the Micromegas detector, will improve dramatically the signal-to-noise ratio. The "discovery potential", the strength of the potential signal in the case an axion is detected, thus, is increased.

This end is already being followed and a study of the desired characteristics of such an optic is performed. A schedule of constructing and commissioning such a device in combination with a new design of Micromegas is underway. The new design envisions a very small Micromegas, which will be surrounded by passive shielding, similar to the one used by TPC in the other end of the magnet.

CAST can also be used to test the presence of large extra dimensions, for the Phase II setup [100]. It is argued that the detection of additional X-rays at least at two pressure settings could be the signature of large extra dimensions. From this requirement, CAST may test two large extra dimensions with a common compactification radius R down to 250 nm in the scenario where $m_a < 1/2R$, and to 370 nm if $1/2R < m_a$.

Although CAST may not have seen any axions yet, it has already managed, with only the data of one year, to set a restriction on the coupling constant five times stronger than any experiment before. Putting the exclusion line on the plot (figure 7.1), a large part of the parameter space is excluded all compatible with solar physics. The limit is also comparable with the limit imposed by astrophysical considerations, although there is large uncertainty involved in those estimations. With the second phase, which is underway, it will have the exciting opportunity to take a look into the axion models zone, for the first time for a laboratory experiment.

Bibliography

[1] R. D. Peccei, “QCD, strong CP and axions”, J. Korean Phys. Soc. **29** (1996) S199.

[2] R. D. Peccei, “The Strong-CP Problem”, in **CP Violation**, ed. C. Jarlskog (World Scientific, Singapore, 1989).

[3] G. ’t Hooft, “Symmetry Breaking Through Bell-Jackiw Anomalies”, Phys. Rev. Lett. **37** (1976) 8.

[4] G. ’t Hooft, “Computation Of The Quantum Effects Due To A Four-Dimensional Pseudoparticle”, Phys. Rev. D **14** (1976) 3432 [Erratum-ibid. D **18** (1978) 2199].

[5] R. D. Peccei and H. R. Quinn, “CP Conservation In The Presence Of Instantons”, Phys. Rev. Lett. **38** (1977) 1440.

[6] R. D. Peccei and H. R. Quinn, “Constraints Imposed By CP Conservation In The Presence Of Instantons”, Phys. Rev. D **16** (1977) 1791.

[7] F. Wilczek, “Problem Of Strong P And T Invariance In The Presence Of Instantons”, Phys. Rev. Lett. **40** (1978) 279.

[8] S. Weinberg, “A New Light Boson?”, Phys. Rev. Lett. **40** (1978) 223.

[9] F. Wilczek, “Asymptotic freedom: From paradox to paradigm”, arXiv:hep-ph/0502113.

[10] K. Bócker, “Impact of Hadronic Axions on Black Hole Accretion Discs and Neutron Stars”, Diplomarbeit, (1999).

[11] H. Leutwyler, “The ratios of the light quark masses”, Phys. Lett. B **378** (1996) 313.

[12] S. Eidelman *et al.* [Particle Data Group], “Review of particle physics”, Phys. Lett. B **592** (2004) 1.

[13] M. Srednicki, “Axion Couplings To Matter. 1. CP Conserving Parts”, Nucl. Phys. B **260** (1985) 689.

[14] G. Raffelt, “ Stars as Laboratories for Fundamental Physics”, Univesity of Chicago Press, 1996.

[15] Y. Asano *et al.*, “Search For A Rare Decay Mode $K^+ \to \pi^+$ Neutrino Anti-Neutrino And Axion”, Phys. Lett. B **107** (1981) 159.

[16] J. E. Kim, “Weak Interaction Singlet and CP Invariance”, Phys. Rev. Lett. **43** (1979) 103;
M. A. Shifman, A. I. Vainshtein, V. I. Zakharov, “Can Confinement Ensure Natural CP Invariance of Strong Interactions?”, Nucl. Phys. **B166** (1980) 493.

[17] D. B. Kaplan, “Opening The Axion Window”, Nucl. Phys. B **260** (1985) 215.

[18] M. Dine, W. Fischler, M. Srednicki, “ A Simple Solution to the Strong CP Problem with a Harmless Axion”, Phys. Lett. **B104** (1981) 199;
A. R. Zhitnitskiĭ, “ On Possible Suppression of the Axion Hadron Interaction”, Yad. Fiz. **31** (1980) 497 [Sov. J. Nucl. Phys. **31** (1980) 260].

[19] J. E. Kim, “Light Pseudoscalars, Particle Physics And Cosmology”, Phys. Rept. **150** (1987) 1.

[20] M. S. Turner, “Windows On The Axion”, Phys. Rept. **197** (1990) 67.

[21] G. G. Raffelt, “Astrophysical Methods To Constrain Axions And Other Novel Particle Phenomena”, Phys. Rept. **198** (1990) 1.

[22] M. S. Turner, “On The Cosmic And Local Mass Density Of ’Invisible’ Axions”, Phys. Rev. D **33** (1986) 889.

[23] D. N. Spergel *et al.* [WMAP Collaboration], “First Year Wilkinson Microwave Anisotropy Probe (WMAP) Observations: Determination of Cosmological Parameters”, Astrophys. J. Suppl. **148** (2003) 175.

[24] R. A. Battye and E. P. S. Shellard, “Axion string constraints”, Phys. Rev. Lett. **73** (1994) 2954 [Erratum-ibid. **76** (1996) 2203].

[25] D. Harari and P. Sikivie, “On The Evolution Of Global Strings In The Early Universe”, Phys. Lett. B **195** (1987) 361.

[26] C. Hagmann and P. Sikivie, “Computer Simulations Of The Motion And Decay Of Global Strings”, Nucl. Phys. B **363** (1991) 247.

[27] H. T. Janka, W. Keil, G. Raffelt and D. Seckel, “Nucleon spin fluctuations and the supernova emission of neutrinos and axions”, Phys. Rev. Lett. **76** (1996) 2621.

[28] P. Sikivie, “Experimental Tests Of The *Invisible* Axion”, Phys. Rev. Lett. **51** (1983) 1415 [Erratum-ibid. **52** (1984) 695].

[29] R. Bradley *et al.*, “Microwave cavity searches for dark-matter axions”, Rev. Mod. Phys. **75** (2003) 777.

[30] S. De Panfilis *et al.*, "Limits On The Abundance And Coupling Of Cosmic Axions At $4.5\,\mu\text{eV} < m_a < 5.0\,\mu\text{eV}$", Phys. Rev. Lett. **59** (1987) 839.

[31] W. U. Wuensch *et al.*, "Results Of A Laboratory Search For Cosmic Axions And Other Weakly Coupled Light Particles", Phys. Rev. D **40** (1989) 3153.

[32] C. Hagmann, P. Sikivie, N. S. Sullivan and D. B. Tanner, "Results From A Search For Cosmic Axions", Phys. Rev. D **42** (1990) 1297.

[33] C. Hagmann *et al.*, "Results from a high-sensitivity search for cosmic axions", Phys. Rev. Lett. **80** (1998) 2043.

[34] S. J. Asztalos *et al.*, "An improved RF cavity search for halo axions", Phys. Rev. D **69** (2004) 011101.

[35] M. Mück, J. B. Kycia and J. Clarke, "Superconducting Quantum Interference Device as a Near-Quantum-Limited Amplifier at 0.5 GHz", Appl. Phys. Lett. **78** (2001) 967.

[36] M. Tada *et al.*, "CARRACK II: A new large-scale experiment to search for axions with Rydberg-atom cavity detector", Nucl. Phys. Proc. Suppl. **72** (1999) 164.

[37] M. Tada *et al.*, "A coupled microwave-cavity system in the Rydberg-atom cavity detector for dark matter axions", arXiv:physics/0101028.

[38] S. Matsuki and K. Yamamoto, "Direct Detection Of Galactic Axions With Rydberg Atoms In An Inhibited Cavity Regime", Phys. Lett. B **263** (1991) 523.

[39] M. T. Ressell, "Limits to the radiative decay of the axion", Phys. Rev. D **44** (1991) 3001.

[40] M. A. Bershady, M. T. Ressell and M. S. Turner, "Telescope Search For Multi-Ev Axions", Phys. Rev. Lett. **66** (1991) 1398.

[41] B. D. Blout, E. J. Daw, M. P. Decowski, P. T. P. Ho, L. J. Rosenberg and D. B. Yu, "A radio telescope search for axions", Astrophys. J. **546** (2001) 825.

[42] K. Van Bibber, N. R. Dagdeviren, S. E. Koonin, A. Kerman and H. N. Nelson, "An Experiment To Produce And Detect Light Pseudoscalars", Phys. Rev. Lett. **59** (1987) 759.

[43] G. Ruoso *et al.*, "Limits on light scalar and pseudoscalar particles from a photon regeneration experiment", Z. Phys. C **56** (1992) 505.

[44] R. Cameron *et al.*, "Search for nearly massless, weakly coupled particles by optical techniques", Phys. Rev. D **47** (1993) 3707.

[45] L. Maiani, R. Petronzio and E. Zavattini, "Effects Of Nearly Massless, Spin Zero Particles On Light Propagation In A Magnetic Field", Phys. Lett. B **175** (1986) 359.

[46] Y. Semertzidis *et al.*, "Limits On The Production Of Light Scalar And Pseudoscalar Particles", Phys. Rev. Lett. **64** (1990) 2988.

[47] G. Cantatore *et al.*, in Proceedings of the 5th International Workshop on the Identification of Dark Matter, Edinburgh, UK, 2004 (to be published).

[48] E. A. Paschos and K. Zioutas, "A Proposal for solar axion detection via Bragg scattering", Phys. Lett. B **323** (1994) 367.

[49] F. T. . Avignone *et al.* [SOLAX Collaboration], "Experimental search for solar axions via coherent Primakoff conversion in a germanium spectrometer", Phys. Rev. Lett. **81** (1998) 5068.

[50] A. Morales *et al.* [COSME Collaboration], "Particle dark matter and solar axion searches with a small germanium detector at the Canfranc underground laboratory", Astropart. Phys. **16** (2002) 325.

[51] R. Bernabei *et al.*, "Search for solar axions by Primakoff effect in NaI crystals", Phys. Lett. B **515** (2001) 6.

[52] D. M. Lazarus, G. C. Smith, R. Cameron, A. C. Melissinos, G. Ruoso, Y. K. Semertzidis and F. A. Nezrick, "A Search for solar axions", Phys. Rev. Lett. **69** (1992) 2333.

[53] S. Moriyama, M. Minowa, T. Namba, Y. Inoue, Y. Takasu and A. Yamamoto, "Direct search for solar axions by using strong magnetic field and X-ray detectors", Phys. Lett. B **434** (1998) 147.

[54] K. Zioutas *et al.*, "A decommissioned LHC model magnet as an axion telescope", Nucl. Instrum. Meth. A **425** (1999) 482.

[55] G. G. Raffelt, "Plasmon Decay Into Low Mass Bosons In Stars", Phys. Rev. D **37** (1988) 1356.

[56] K. van Bibber, P. M. McIntyre, D. E. Morris and G. G. Raffelt, "A Practical Laboratory Detector For Solar Axions", Phys. Rev. D **39**, (1989) 2089.

[57] L. Di Lella, A. Pilaftsis, G. Raffelt and K. Zioutas, "Search for solar Kaluza-Klein axions in theories of low-scale quantum gravity", Phys. Rev. D **62** (2000) 125011.

[58] J. N. Bahcall, W. F. Huebner, S. H. Lubow, P. D. Parker and R. K. Ulrich, "Standard Solar Models And The Uncertainties In Predicted Capture Rates Of Solar Neutrinos", Rev. Mod. Phys. **54** (1982) 767.

[59] J. N. Bahcall and M. H. Pinsonneault, "What do we (not) know theoretically about solar neutrino fluxes?", Phys. Rev. Lett. **92** (2004) 121301.

[60] P. Serpico and G. Raffelt, “New Calculation of Solar Axion Flux”, CAST Internal Report (2004)

[61] G. Raffelt and L. Stodolsky, “Mixing Of The Photon With Low Mass Particles”, Phys. Rev. D **37** (1988) 1237.

[62] M. Bona *et al.*, “Performance of the first CERN - INFN 10 m long superconducting dipole prototype for the LHC”, CERN-AT-94-26-MA *4th European Particle Accelerator Conference (EPAC 94), London, England, 27 Jun - 1 Jul 1994*

[63] K. Barth *et al.*, “Commissioning and first operation of the cryogenics for the CERN Axion Solar Telescope (CAST)”, AIP Conf. Proc. **710** (2004) 168.

[64] NOVAS (Naval Obervatory Vector Astrometry Subroutines), http://aa.usno.navy.mil/software/ovas/novas_info.html

[65] Altmann, J. and Egle, W. J. and Bingel, U. and Hafner, W. and Gaenswein, B. and Schwarz, H. and Neugschwender, A., “Mirror system for the German X-Ray satellite ABRIXAS: I. Flight mirror fabrication, integration, and testing”, in *X-Ray Optics, Instruments and Missions II*, R. B. Hoover and A. B. Walker eds”, SPIE Conf. Proc. (1998) 350.

[66] Egle, W. J. and Altmann, J. and Kaufmann, P. and Muenker, H. and Derst, G. and Schwarz, H. and Neugschwender, A., ”Mirror system for the German X-ray satellite ABRIXAS: II. Design and mirror development”, in *X-Ray Optics, Instruments and Missions*, R. B. Hoover and A. B. Walker eds”, SPIE Conf. Proc. **3444** (1998) 359.

[67] Egle, W. J. and Altmann, J. and Schwarz, H., ”ABRIXAS mirror system: mirror module testing and integration in the ABRIXAS satellite”, in *X-Ray Optics, Instruments and Missions II*, R. B. Hoover and A. B. Walker eds”, SPIE Conf. Proc. **3766** (1999) 2.

[68] G. Lutz *et al.*, “An application of space technology to the terrestrial search for axions: The X-ray mirror telescope at CAST”, Nucl. Instrum. Meth. A **518** (2004) 201.

[69] G. Raffelt and L. Stodolsky, “New Particles From Nuclear Reactions In The Sun”, Phys. Lett. B **119** (1982) 323.

[70] M. Krčmar, Z. Krečak, A. Ljubičić, M. Stipčević and D. A. Bradley, “A novel approach to the search for solar axions using Li-7”, Phys. Rev. D **64** (2001) 115016.

[71] C. Hearty *et al.*, “Search For The Anomalous Production Of Single Photons In E+ E- Annihilation At S**(1/2) = 29-Gev”, Phys. Rev. D **39** (1989) 3207.

[72] F. Sauli, ’Principles of Operation of Multiwire, Proportional and Drift Chambers”, CERN Report 77-09 (1977).

[73] G. Charpak, R. Bouclier, T. Bresani, J. Favier and Č. Zupaničič, “The Use Of a Multiwire Proportional Counters To Select And Localize Charged Particles”, Nucl. Instrum. Meth. **62** (1968) 262.

[74] E. Gatti, A. Longoni, P. Semenza and H. Okuno, “Optimum Geometry For Strip Cathodes Or Grids In Mwpc For Avalanche Localization Along The Anode Wires”, Nucl. Instrum. Meth. **163** (1979) 83.

[75] A. Breskin, G. Charpak and F. Sauli, “High Accuracy Bidimensional Drift Chambers”, Nucl. Instrum. Meth. **125**, (1975) 321.

[76] D. R. Nygren, “A Time Projection Chamber - 1975”, PEP-0198 *Presented at 1975 PEP Summer Study. Included in Proceedings.*

[77] A. Oed, “Position Sensitive Detector With Microstrip Anode For Electron Multiplication With Gases”, Nucl. Instrum. Meth. A **263** (1988) 351.

[78] A. Sharma, “Gaseous Micropattern Detectors: High Energy Physics and Beyond”, ICFA Instrum. Bull. **22** (2001) 01.

[79] F. Angelini, R. Bellazzini, A. Brez, M. M. Massai, R. Raffo, G. Spandre and M. A. Spezziga, “The Microgap chamber”, Nucl. Instrum. Meth. A **335**, (1993) 69.

[80] R. Bellazzini *et al.*, “The WELL detector”, Nucl. Instrum. Meth. A **423** (1999) 125.

[81] F. Bartol *et al.*, “ The C.A.T. Pixel Proportional Gas Counter Detector”, J. Phys. III France **6** (1996) 337.

[82] G. Chaplier, C. Bouillot, M. Lemonnier, S. Megtert and J. P. Boeuf, “Preliminary results of the experimental and simulated intrinsic properties of the Compteur A Trou (CAT) detector: Behavior with synchrotron radiation”, Nucl. Instrum. Meth. A **426** (1999) 339.

[83] A. Sarvestani, H. J. Besch, N. Pavel, N. Sauer, C. Strietzel, A. H. Walenta and R. H. Menk, “Study of the high rate performance of the MicroCAT detector”, Nucl. Phys. Proc. Suppl. **78** (1999) 431.

[84] Y. Giomataris, P. Rebourgeard, J. P. Robert and G. Charpak, “MICROMEGAS: A high-granularity position-sensitive gaseous detector for high particle-flux environments”, Nucl. Instrum. Meth. A **376** (1996) 29.

[85] P. Rehak, G. C. Smith, J. B. Warren and B. Yu, “MIPA : A New micro-pattern detector”, SLAC-J-ICFA-20-3

[86] F. Sauli, “GEM: A new concept for electron amplification in gas detectors”, Nucl. Instrum. Meth. A **386** (1997) 531.

[87] R. Bouclier *et al.*, “New observations with the gas electron multiplier (GEM)”, Nucl. Instrum. Meth. A **396** (1997) 50.

[88] A. Delbart, R. de Oliveira, J. Derre, Y. Giomataris, F. Jeanneau, Y. Papadopoulos and P. Rebourgeard, “New developments of Micromegas detector”, Nucl. Instrum. Meth. A **461** (2001) 84.

[89] J. Derre, Y. Giomataris, H. Zaccone, A. Bay, J. P. Perroud and F. Ronga, “Spatial resolution in Micromegas detectors”, Nucl. Instrum. Meth. A **459** (2001) 523.

[90] J. Derre, Y. Giomataris, P. Rebourgeard, H. Zaccone, J. P. Perroud and G. Charpak, “Fast signals and single electron detection with a MICROMEGAS photodetector”, Nucl. Instrum. Meth. A **449** (2000) 314.

[91] Y. Giomataris, “Development and prospects of the new gaseous detector 'Micromegas”', Nucl. Instrum. Meth. A **419** (1998) 239.

[92] G. Barouch *et al.*, “Development of a fast gaseous detector *Micromegas*”, Nucl. Instrum. Meth. A **423** (1999) 32.

[93] D. Breton, E. Delagnes, M. Houry, “Very High Dynamic Range and High-Sampling Rate VME Digitizing Boards for Physics Experiments”, *to appear in Proceed. IEEE 2004 Med. Imag. Conf., Rome , Oct 2004*

[94] http://www.mpe.mpg.de/panter/panter-neu/about_en.html

[95] S. Andriamonje *et al.*, ”Micromegas X-ray Detectors for CAST: Status Report”, CAST Internal Report (2002).

[96] http://root.cern.ch/

[97] http://www.cern.ch/GEANT4

[98] R. J. Creswick, F. T. . Avignone, H. A. Farach, J. I. Collar, A. O. Gattone, S. Nussinov and K. Zioutas, “Theory for the direct detection of solar axions by coherent Primakoff conversion in germanium detectors”, Phys. Lett. B **427** (1998) 235.

[99] K. Zioutas *et al.*, “First Results From the CERN Axion Solar Telescope”, Phys. Rev. Lett. **94** (2005) 121301.

[100] R. Horvat, M. Krcmar and B. Lakic, “CERN axion solar telescope as a probe of large extra dimensions”, Phys. Rev. D **69** (2004) 125011.

Acknowledgement

For three years, I have had the luck and –most importantly– the pleasure to work in this experiment, following its course from the commissioning (in fact the very first training quench of the magnet) until the conclusion of its first phase. So many things I have seen, so much information gathered, so many people I would like to mention...

I have to start this part expressing my gratefulness to my supervisor, Prof. D. H. H. Hoffmann; for giving me the opportunity to work in this subject; for the trust he has shown to my person and for his (very successful) tries to supply me with the best conditions to work.

I am indeed indebted to Prof. Konstantin Zioutas who acted as my supervisor at CERN, where all this work was done; for introducing me to this field, for trusting me since my undergraduate studies; for having drawn my path to this work; for posing an example of a hard worker.

Yannis Giomataris and the group in Saclay (Esther Ferrer Ribas, Stephan Aune) I would like to thank for getting probably the most direct information and 'feeling' of the Micromegas detector that one can; for all the discussions that have proven crucial during the course of my work.

Thank you Igor G. Irastorza, Biljana Lakić and Thomas Papaevangelou for having answered any silly question and request, and for having read this first. Without your friendship and help, this work would be half of what it is. I want to thank Esther for the very useful last-minute comments, and special thanks go to Laura and Christos for the last minute problem-solving.

My thanks should go to all the people in the collaboration that I have met, for everything I have learned from them and for the fun we have had during the shifts (ok, outside shifts as well!).

My utmost respect, love and gratitude to my parents, sister, friends and Igor, for it is them I owe who I am.

Curriculum Vitae

Name: Theopisti Dafni
Birth date/Place: May 8, 1978 / Thessaloniki, Greece
Citizenship: Greek (Hellenic)

Educational Profile:

since Aug. 2002	PhD student at the Technical Univeristy, Darmstadt
1997-2002	Bachelor (Ptychio) of Physics at the Aristotle University of Thessaloniki, Greece Specialization : Nuclear and Elementary Particle Physics Diploma thesis: “Search for Novel Elementary Particles in Astroparticle Physics”
1990-1996	17th Junior and Senior High School of Thessaloniki

Publications:

1. K. Zioutas *et al.*, “First Results From the CERN Axion Solar Telescope”, Phys. Rev. Lett. **94** (2005) 121301.

Proceedings in Conferences:

- * Th. Dafni *et al.*, “First Results From the CERN Axion Solar Telescope (CAST)”, Proceedings of “Les Rencontres de Physique de la Valée d’Aoste: Results and Perspectives in Particle Physics”, ed. M. Greco, Vol. XXXIV (2004) 19.
- I. G. Irastorza *et al.*, [CAST collaboration], “First Results from the CERN axion solar telescope (CAST),” to be published by World Scientific, Proceedings of the Fifth International Workshop on the Identification of Dark Matter.
- S. Andriamonje *et al.*, [CAST Collaboration], “The CERN Axion Solar Telescope (CAST): An update,” Nucl. Phys. Proc. Suppl. **138** (2005) 41.
- S. Andriamonje, S. Aune, T. Dafni, E. Delagnes, G. K. Fanourakis, E. Ferrer Ribas, T. Geralis, Y. Giomataris, K. Kousouris, T. Papaevangelou, “A low background Micromegas detector for axion searches,” Nucl. Instrum. Meth. A **535** (2004) 309.
- S. Andriamonje, S. Aune, T. Dafni, G. K. Fanourakis, E. Ferrer Ribas, H. Fischer, J. Franz, T. Geralis, A. Giganon, Y. Giomataris *et al.* “A Micromegas detector for the CAST experiment,” Nucl. Instrum. Meth. A **518** (2004) 252.
- C. Eleftheriadis *et al.*, “Axion searches at CERN with the CAST telescope,” Proceedings of NEB-X Conference on ”New Developments in Gravity”, Chalkidiki, Greece, 2002 (astro-ph/0305534).
- J. I. Collar *et al.*, [CAST Collaboration], “CAST: A search for solar axions at CERN,” Proceedings SPIE, 2003 (hep-ex/0304024).
- I. G. Irastorza *et al.*, [CAST collaboration], “The CERN axion solar telescope (CAST): Status and prospects,” Proceedings of the Fourth International Workshop on the Identification of Dark Matter, (eds. N. J. C. Spooner and V. Kudryavtsev), World Scientific ISBN 981-238-237-2, Singapore, 402, 2003 (astro-ph/0211606).

Hiermit erkläre ich, dass ich die Arbeit selbständig
und nur mit den angegebenen Hilfsmitteln angefertigt und
nicht schon früre eine Promotion versucht habe.